Thermal Energy Storage for Building-Integrated Photovoltaic Components

Alaa Liaq Hashem Al-Mosawi B.Sc., M.Sc.

A thesis submitted for the

Degree of Doctor of Philosophy

Energy Systems Research Unit

Department of Mechanical Engineering

University of Strathclyde

Glasgow, Scotland

September 2011

In memory of my Mother

Copyright Declaration

The copyright of this thesis belongs to the author under the terms of the United Kingdom Copyright Act as qualified by the University of Strathclyde Regulation 3.50. Due acknowledgement must always be made of the use of any material contained in, or derived from, this thesis.

Acknowledgments

Table of Contents

List of Figures

Chapter 6

List of Tables

Nomenclature

Symbols

A Area, Constant $\{J/kg.K^2\}$.

AC Air conditioning.

B Constant $\{J/kg.K\}$

Bi Biot Number $\{-\}$.

C, c_p Specific heat at constant pressure $\{J/kg.K\}$, self-coupling and cross-coupling coefficients, constant.

d, D Thickness, diameter, hydraulic duct thickness, discharge process.

$dblf$ Double skin façade.

e Electronic charge $\{1.6*10^{-19}C\}$.

Fo Fourier Number $\{-\}$.

f Liquid fraction factor $\{-\}$.

g, gr Acceleration due to gravity $\{m/s^2\}$, ground level.

H, h Enthalpy $\{J/kg, kJ/kg\}$, height of a vertical surface.

$h_c, \bar{h}$ Convection coefficient $\{W/m^2K\}$.

i, j Grid indices of nodes in x and y directions.

k, K Stefan-Boltzmann constant $\{J/K\}$, thermal conductivity $\{W/m.K\}$, K-type thermocouple.

L, l Duct length, layer thickness, heat of fusion $\{kJ/kg, kJ/m^3\}$, liquid phase

M, m Mass $\{kg, g\}$, melting phase.

n, N Number of nodes per layer, number of..., constant.

NE Number of elements.

P Shape coefficient, power $\{W, MW, kWhr\}$.

Q, q Heat flux $\{W/m^2, kW/m^2\}$, heat source term $\{kJ/kg, kJ/m^3\}$.

r, R Radius, shape coefficient, thermal resistance $\{m^2K/W\}$.

Ra Rayleigh Number $\{-\}$.

S Maximum liquid thickness, surface position.

t Time $\{second\}$.

T Temperature $\{°C, K\}$, T-type thermocouple.

U	Overall heat transfer coefficient $\{W/m^2K\}$.
V	Volume $\{m^3\}$, voltage $\{volt\}$.
w	Width.
X	Phase change front location.
x, y, z	Cartesian coordinates.
Z	Height $\{m\}$.

Subscripts

ach	Volumetric flow rate measured in room air changes per hour.
amb	Ambient.
app	Apparent method.
$conv$	Convection.
ch	Charge process.
cr	Critical condition value.
$cell$	Photocell.
c,i	Cross coupling coefficient for node (i).
$extwall$	External wall.
eff	Efficiency.
$effc$	Effective.
$flagPCM$	Flag to indicate PCM existing.
$final$	Final state/condition.
f	Fluid.
in	Inside condition.
i-1	Previous node.
i+1	Next node.
$init$	Initial state/condition.
liq ,$liquid$	Liquid phase.
$melt$	Melting phase.
mp	Maximum power point.
max	Maximum value.
out	Outside condition.
opq	Opaque surface.

oc	Open circuit.
PCM	Phase change materials.
ph ,phase	Phase.
part	Particle properties.
rad	Radiation.
ref	Reference condition.
sol, s,solid	Solid phase.
stru	Materials structure properties.
sc	Short circuit.
s,i	Self coupling coefficient for node *i*.
Subde	Subcooling degree *{˚C}*.
t+Δt	Next time step.
tr	Transparent surface.

Greek symbols

α	Current temperature coefficient *{A/˚C}*, thermal diffusivity *{m²/s}*.
β	Voltage temperature coefficient *{V/˚C}*, thermal expansion coefficient *{K^{-1}}*.
ω	Shape factor.
ρ	Density *{kg/m^3}*.
Δ	Differences values.
∇	Differential operator.
∂	Partial differential
μ	Dynamic viscosity *{N·s/m^2}*.
υ	Kinematics viscosity *{m^2/s}*.
δ	Thickness.

Abstract

The combination of building structure, renewable components, and management systems provides new opportunities for exploiting natural energy and minimising impact on the environment. Using hybrid solutions that integrate different sources of renewable energy and demand reduction components constitutes an effective way to improve overall energy efficiency and create appropriate load profiles for the local deployment of alternate energy sources.

In the present work, phase change material (PCM) is employed to lower the temperature of a photovoltaic (PV) panel to ensure maximum cell efficiency and protect cells from excessive heat. This hybrid system, termed PV/PCM, allows the stored heat to be recovered using air or water flow. The behaviour of the PCM will be altered by the fact that the thermal properties of specific heat, density and conductivity are continually changing, with new values depending on the context temperature and the phase change temperature range.

The PCM behaviour is represented by a new algorithm, which was constructed, validated, and incorporated within a state-of-the-art building energy simulation program, ESP-r, with interactions taking place between PV and PCM physical models. Building control strategies were then developed to take advantage of the PCM's latent heat capacity, especially under peak load operation or when high PV temperature is observed. The integration of building control systems with the charging-discharging of the PCM layer enables the program user to control the quality and efficiency of these processes, and allows for the optimal use of the thermal energy stored.

The thesis describes the form of the developed PV/PCM model and presents the results from its empirical validation. Finally, the thesis applies the new model to investigate the impact on building energy efficiency of deploying PV/PCM in practice.

Chapter 1 : Thesis Context

1.1 Introduction

The major purpose of the building envelope is to provide passive climate modification and indoor conditions that best match the occupant's activities. This goal is rarely attained in practice, and it becomes necessary to deploy heating, ventilating and air conditioning systems in order to provide a comfortable environment for occupants. With population and economic growth, global energy consumption is expected to increase significantly. The energy consumed in buildings accounts for around 30%-40% of the world's energy consumption, making buildings the largest energy consumer (UNEP 2009). The majority of energy used in buildings derives from fossil fuel and there is growing concern about the issues of sustainability and environmental impact (Porez-Lombard *et al* 2008). Because of this, governments are turning towards the use of cleaner and more sustainable resources in the form of decarbonised fossil fuel, nuclear and renewable energy. To accommodate these new resources, the need to operate buildings more efficiently becomes an urgent objective. New design concepts have emerged, such as 'low energy' and 'zero carbon' buildings, which ease fossil fuel consumption by adding new functionality to the building envelope. These new functions aim to reduce the total energy consumed by integrating passive and/or active technologies within the building envelope (Pitts 2008). Typical approaches reduce thermal conductivity, increase thermal capacity, modify radiation transmission, or generate power, with the intention of minimising heating and cooling loads over time, or matching these loads from local energy sources.

1.2 Buildings and Energy Consumption

Globally, building energy consumption has been steadily increasing and is exceeding other major consumption sectors such as industry and transportation. In the Middle East 33.6% of total electricity generation is consumed in the residential sector according to the International Energy Agency (IEA 2009). Future growth in population will increase demand, as typified in figure 1-1. The expansion in HVAC systems energy use is particularly significant. In 2007, the electricity, heat generation, and transport sectors produced nearly 64% of global CO_2 emissions.

Overall world increase 6088 million tons of oil equivalent
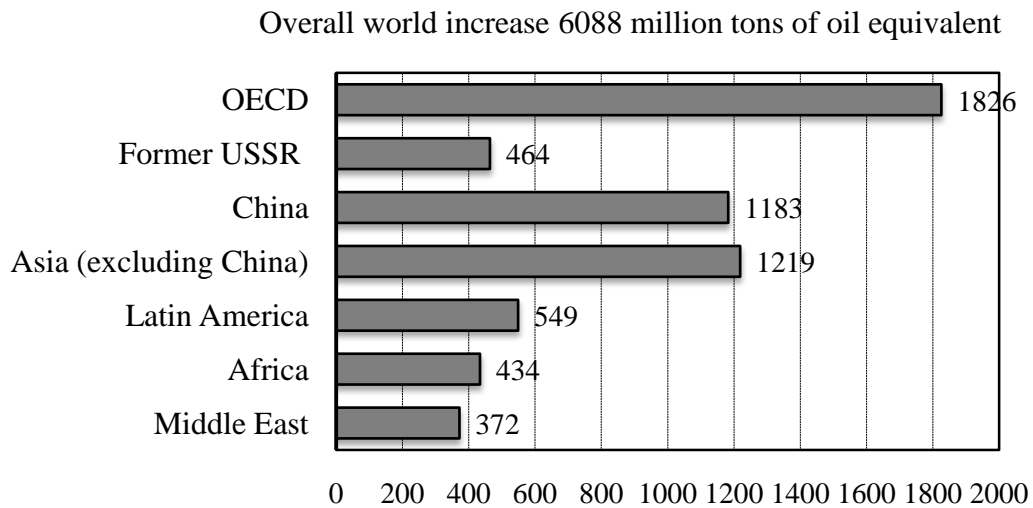
Figure 1-1: Growth in the demand for primary energy among regions of the world (2000-2030) (IEA 2009).

In 2007, the generation of electricity and heat was responsible for 41% of the world's total CO_2 emission, as compared to 27% in 1971, as shown in figure 1-2. By 2030, the World Energy Outlook Project anticipates that demand for electricity will be almost twice as high as in 2007, driven principally by population growth and rising wealth, resulting in more electrical devices in the domestic, commercial, and industrial sectors (Porez-Lombard *et al* 2008). Referring to figure 1-2, electricity

3

and heat generation contributed most significantly to CO_2 emissions in 2007. This implies that as more fossil fuels are used to meet growing energy demands, greenhouse gas emissions will rise further. Without proper mitigation strategies and technological improvements in buildings, this pattern is unlikely to change in the near future. The residential sector accounts for a significant portion of the energy consumed in buildings; in developing countries, this can be over 70% (Al-Ajmi *et al* 2006). Furthermore, the energy consumed in non-residential buildings, such as offices, public buildings and hospitals, is also significant. These sectors must therefore be targeted, with developments being pursued according to aggressive energy sustainability criteria.

1971 Total emission: 14.1 Gt CO_2
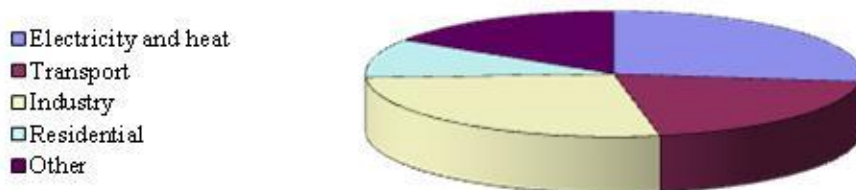
2007 Total emission: 29 Gt CO_2
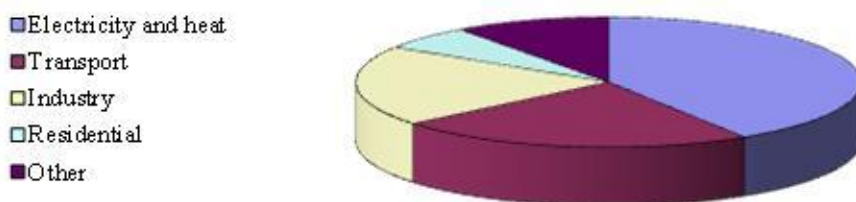
Figure 1-2: World CO_2 emissions classified by sector (UNEP 2007).

4

1.3 Approaches to Reducing Energy Consumption in Buildings

The actual performance of a renewable energy component when integrated in a building depends on the specific building design and the environmental context within which it operates. The combination between building components, renewable (passive or active) components, and the building's management systems provides new opportunities for exploiting natural energy. A reduction in energy consumption and impact can be achieved in many ways, including the use of low carbon building materials, enhanced insulation, low energy lighting, embedding renewable technologies, intelligent control and the use of low carbon fuels (CIBSE 2006). Typically, several approaches may be employed as follows:

1. Load reducing strategies − via load control, advanced glazing, daylight capture, lighting and air conditioning modulation, adaptive materials, smart shading systems and intelligent energy management.

2. Load shifting strategies − via building energy management, thermal storage for pre-cooling or pre-heating and waste heat recovery. Many countries, the electrical demands, and time-of-use utility rates have been designed to encourage shifting of electrical loads from peak periods to off-peak periods. For example, electrical demands vary significantly during the day and night due to changes in weather conditions and energy demands. Buildings with distributed thermal storage materials can shift much of the load on residential air conditioners from peak to off-peak time periods. As a result, capital investment in peak power generation may be significantly reduced for power utilities and this can result in cost savings to customers. In general, where power utilities are

offering time of day rates, building-integrated thermal storage can enable customers to take advantage of lower utility rates during off-peak hours.

3. Local heat and electricity generation using photovoltaic panels, fuel cells, micro gas turbines, solar water heating, solar pool heating, passive or active solar space heating/cooling and geothermal heat pumps; on-site electricity generation using wind turbines and photovoltaic modules is becoming more common.

In any strategy used to reduce building energy consumption all types of renewable energy components can, in principle, be utilised. Improvements in component efficiency and construction integration are important targets of research. Hybrid solutions that integrate different renewable energy and demand reduction components represent an effective way to improve the overall energy efficiency.

1.4 Research Objectives

Ensuring the overall effectiveness of the approach that is selected for a particular building is the key objective in low energy building design. The incorporation of renewable energy components in a building must be done in a way that ensures reliable performance and cost-effective energy saving. The former goal can be attained through the integration of different renewable energy components to produce a hybrid passive/active solution. The latter goal can be attained by ensuring that the component operates in near optimum conditions. For example, phase change material (PCM) may be employed to lower the temperature of a photovoltaic (PV) panel to ensure maximum cell efficiency and protect cells from excessive heat. This hybrid system, hereinafter called PV/PCM allows stored heat to be additionally recovered using air or water flow. The behaviour of the PCM will be altered by the fact that the thermal properties-specific heat, density and conductivity - are

continually changing, with new values depending on the context temperature, ambient temperature and the phase change temperature range. The PCM's apparent specific heat is termed the effective heat capacity, with an increase acting to absorb a large fraction of the local heat flux. Within the present work, the PCM's new behaviour is represented by a mechanism in which a 'hand-shaking' algorithm was constructed, validated, and built into a state-of-the-art building energy simulation tool, ESP-r, with interaction taking place between separate PV and PCM model nodes, as shown in figure 1-3.
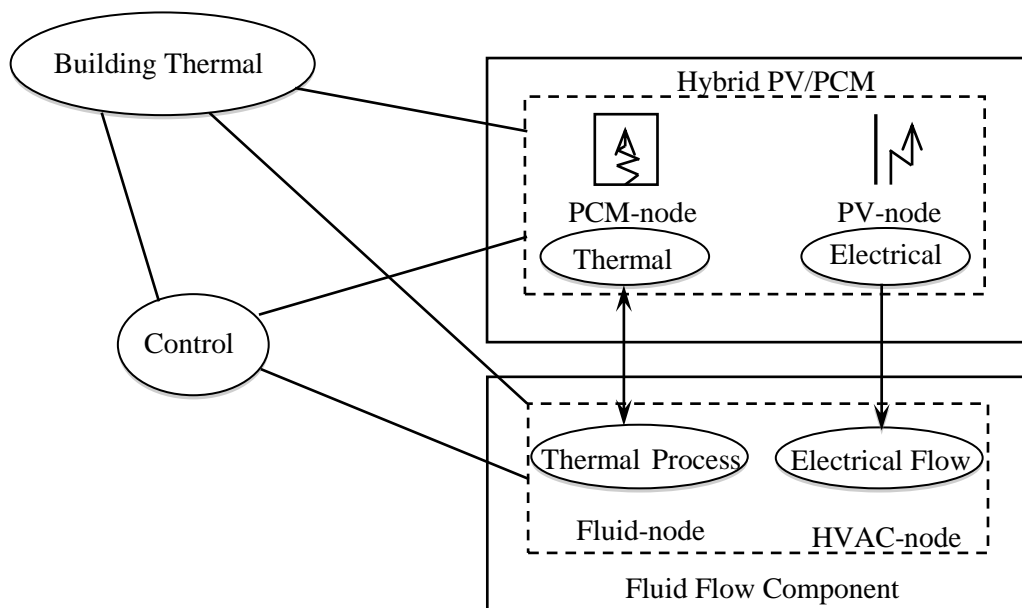
Figure 1-3: The coupled domain for PV/PCM and air flow within the building façade.

This algorithm has been enhanced by a coupling function which determines appropriate natural or forced convection for heat transfer, and which governs whether the phase change process is delayed or continued. This process allows the maximum latent heat potential to be utilised. The objectives of this research are to assess the possibility of:

1- Employing the PCM's latent heat characteristic to ensure that the photovoltaic panel temperature is maintained at a level that around to ambient temperature. This will enhance PV cell efficiency, maximises power output and protects the cell's integrity.

2- Introducing building control strategies that utilise the latent heat advantage, especially under peak load operation or when high photovoltaic temperature observe.

3- Developing PCM-based building envelopes that integrate with the building's heating, cooling and ventilation systems, with the overall aim of exploiting energy from the environment to modulate the indoor climate at low energy expense.

As can be seen in figure 1-3, hybrid PV/PCM components simultaneously affect the thermal and electrical domains within the integrated building model. PV components convert a portion of the solar radiation falling on the building façade to electrical power, which supplies the power flow network associated with plant components (e.g. the fan to transport heat from the PCM heat exchanger to the airflow within the air conditioning system as well as lighting and small power loads). In ESP-r, the facility exists to simultaneously solve the electrical and thermal flows (Clarke 2001 and Kelly 1998). Because building zones, HVAC components, and renewable energy components are represented by a system of nodes, controllers may sense state properties with appropriate actions applied to model parameters as required.

1.5 Thesis Outline

Specifically, this research examines how PCM can be deployed to maintain PV panel power output at a maximum. This is done by utilising the PCM as a heat sink on the rear surface of the PV panel. The thesis contains seven chapters. Chapter One introduces the context of the research topic and elaborates the advantages that may be obtained from the integration of renewable energy in the building envelope. It also reviews strategies that may be applied to reduce energy demand and integrate new energy supply streams. Further, an outline of the research objectives is given, and the chapter ends with a description of the research procedure followed in the research. Chapter Two provides a technology review of PCM and fields of applications. It also reviews the effect of temperature on the efficiency of PV cells. Chapter Three describes the development and verification of a mathematical model for PCM and its integration with models representing PV components within the ESP-r system. Chapter Four outlines the enhancement of the ESP-r subroutine involving the PCM's variable thermo-physical properties, and how the convection effects are introduced and sub-cooling problems quantified. Moreover, the optical properties are adjusted to facilitate the semi-transparent PV components examined later in the work. Chapter Five presents a description of the experimental work to verify and calibrate the new PV/PCM model and presents the test results and validation outcomes. Chapter Six describes the strategies devised to achieve the integration of PCM within building constructions, and examines the potential of the building energy management system to facilitate this integration. Chapter Seven presents the main conclusions drawn from the research and makes recommendations for future work.

Chapter 2 : Technology Review

2.1 Thermal Energy Storage

Thermal energy can be stored as a change in the internal energy of a material either as sensible heat, latent heat or as a combination of both. With sensible heat storage, a material's temperature changes during the process of charging and discharging without a change in phase. The heat storage size then depends on the mass of the heat storage medium (m), its average specific heat (C_p) and temperature change (Sharma *et al* 2009):

$$Q = m \cdot C_p \cdot (T_{final} - T_{init})$$

2.1

Water and oil are two substances that are normally used as sensible heat storage liquid types, while the main solid types are rock, brick, concrete, iron and earth. Two disadvantages of sensible heat storage are the large system size and the high temperature difference required (Fath 1995). Latent heat storage is based on the capture or release of heat when a material experience a phase change from solid to liquid or liquid to gas; such materials are termed phase change materials (PCM). PCM has a significantly higher energy density than non-PCM.

2.2 Phase Change Energy Storage Materials

Unlike sensible energy storage materials, PCM absorbs and releases heat at a constant temperature, a process that is completely reversible. Such materials store 5–14 times more heat per unit volume than sensible storage materials, as shown in figure 2-1 (Sharma *et al* 2009). Once the melting or solidification process is complete, any further heat stored will manifest as a temperature rise. The latent heat stored during the phase change is equal to the enthalpy differences between the solid

and liquid phases, and is termed the solid-liquid phase enthalpy change, melting enthalpy or heat of fusion (Mehling and Cabeza 2008):

$$\Delta Q = \Delta H = m \cdot \Delta h$$

2.2
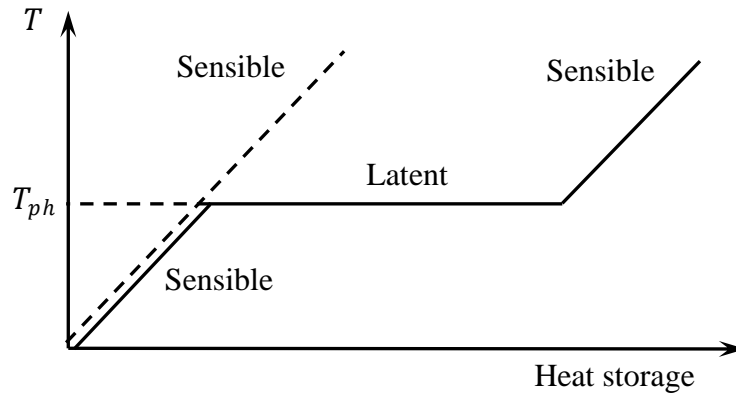
Figure 2-1: Heat storage as latent (———) and sensible (-----).
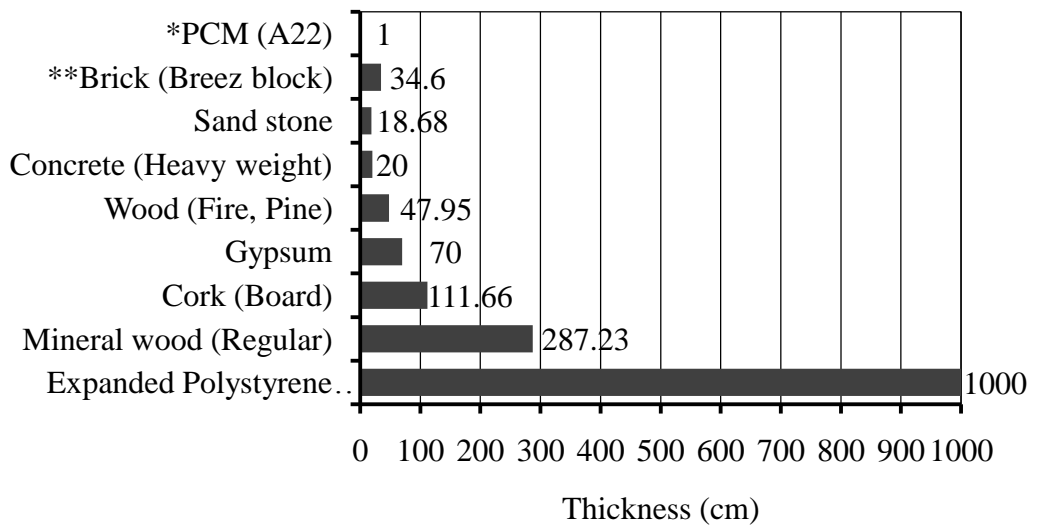
Thickness (cm)

Figure 2-2: Thickness of different building construction layers to store as much heat as a 1 cm thick layer of PCM undergoing phase change.

*The PCM has a capacity of 130 MJ/m^3 and a phase change temperature range of 4˚C (Appendix A).

** Except bricks that have a high thermal capacity such as Feolite. Data for other materials are available in Appendix C.

In building applications, the use of PCM adds little mass, resulting in few additional structural requirements compared to a sensible heat storage system as shown in figure 2-2, which gives a general comparison of heat storage capacities of different materials compared to PCM.

2.2.1 PCM Classifications

There are many organic and inorganic materials that may be classified as PCM and these are organised according to their melting temperature and latent heat of fusion. In general, inorganic materials have almost doubled the volumetric latent heat storage capacity (250–400 kJ/m^3) of organic materials (128–200 kJ/m^3) (Sharma *et al* 2009). Based on their distinct thermal and chemical behaviour, they are divided into subgroups; the behaviour of each subgroup then dictates the design approach of an energy storage system using a PCM of a particular subgroup (Garg *et al* 1985; Pasupathy *et al* 2008). Salt hydrates (general formula $AB.nH_2O$ where A is the acid, B is the base and n the number of water molecules) are a crucial PCM group, which exhibit attractive cost and behaviour characteristics; the following represent some important facts about salt hydrates.

1. Massive latent heat of fusion per unit volume (~350 MJ/m^3).

2. Relatively high thermal conductivity (almost double that of paraffin at ~0.5 W/m˚C).

3. Lower volume change on melting.

4. Low corrosive action and slight toxicity.

5. Moderate costs compared to paraffin.

13

The sub-cooling is a major disadvantage of this PCM group. Organic materials (mixture of mostly straight chain n-alkanes with general formula $CH_3-(CH_2)n-CH_3$) are defined as paraffin and non-paraffin and some exhibit congruent melting, meaning that the melting/freezing cycle can occur indefinitely without phase segregation and consequent degradation of performance (Sharma *et al* 2009). Self-nucleation means that they crystallize with little or no super-cooling and are usually non-corrosive. Some of the features of organic materials are as follows:

1. high heat of fusion;

2. inflammable;

3. low thermal conductivity;

4. low flash point;

5. varying level of toxicity; and

6. instability at high temperatures.

Paraffin-based PCMs are available for use over a large temperature range. Due to cost considerations, however, only technical grade paraffin may be used in latent heat storage systems. Paraffin PCMs are safe, reliable, predictable, inexpensive, and non-corrosive (Farid *et al* 2004). They are stable below 500˚C, show little volume change on melting, have low vapour pressure in the melted form, provide a wide range of melting temperatures, have minimal sub-cooling, and are chemically inert with no phase segregation. On the other hand, their low conductivity (0.2 W/m˚C) limits their application. Metallic fillers, metal matrix structures, and

14

fins have been used to improve conductivity. Due to their compatibility with metal, they can be used in electronic devices to provide temperature control. Organic non-paraffin's are the most numerous of the PCMs and possess highly varied properties. Each such material has its own unique set of properties, unlike the paraffin's, which have similar properties (Abhat 1983). Fatty acids, alcohols and glycols are appropriate for energy storage because they have high heat of fusion values compared to those of paraffin. They also exhibit reproducible melting and freezing behaviour and freeze with no super-cooling (Zalba *et al* 2003). Because organic non-paraffin PCMs has different thermal and chemical behaviour, they are divided into subgroups; the thermal properties of each subgroup will again dictate the design of any latent heat storage system. When using such PCMs, they must be encapsulated so that they do not adversely affect the function of the construction.

2.2.2 Application of PCM

Three approaches to PCM deployment are possible: direct incorporation, immersion and encapsulation (Hawes *et al* 1993). The first two approaches affect the function of the related construction due to direct contact with the construction material; the third approach requires the containment of the PCM within a capsule that is introduced into the material during manufacture. With encapsulation, it is possible to employ large volume containment (macro-encapsulation), where the PCM is located within tubes, pouches, spheres, panels or similar receptacles (Sharma *et al* 2009). Such containers serve directly as heat exchangers. Macro-encapsulation may fail due to poor PCM conductivity, resulting in the PCM solidifying around the edges and preventing effective heat transfer. Further, the PCM capsules may be destroyed when building materials are cut (Mehling and Cabeza 2008).

With micro-encapsulation, the dimensions are small, allowing the PCM to be incorporated simply and economically into conventional construction materials. In this approach, spherical or rod-shaped particles are enclosed by thin, high molecular weight polymer film. The coated particles can then be incorporated in any matrix that is compatible with the encapsulating film. It follows that the film must be compatible with both the PCM and the matrix (Sharma *et al* 2009). Both micro- and macro-encapsulation, when applied to concrete, require plastic and metal encapsulation, which, although expensive is safe as the PCM is not in contact with the concrete. While micro-encapsulation of PCM in concrete is thermally effective, it can adversely affect the mechanical strength of the concrete. Composite PCM solutions improve the conductivity, heat storage and handling versatility. Composites are made by embedding PCM in the matrix of another material or, conversely, by embedding another material into the PCM.

2.3 PCM for Energy Saving in Buildings

In buildings, increased thermal mass decreases temperature swings, which can improve occupant comfort and reduce peak cooling/heating loads, and accordingly reduce energy consumption (Zhang *et al* 2008). The thermal energy storage of walls and ceilings can be improved by incorporating PCM: the latent heat capacity of wallboard with 30% PCM by weight is about five times greater than the heat uptake of conventional wallboard for a 5.5˚C rise in temperature. The PCM effectively increases the thermal mass of the building material during the transition temperature process of the PCM. Sharma *et al* (2005) provide data for key performance attributes of commercially available PCMs. Different types were studied for integration in building materials, including organic materials such as

16

paraffin, and inorganic materials such as salt hydrates. Effort was focused on integration within different building components, e.g. wallboard, floor/ceiling tiles, particle board, foam insulation board, plaster, radiant barriers, cellulose insulation, solar blinds, and concrete. Within the human comfort temperature range spanning approximately 16˚C-25˚C, latent heat storage materials have been found to be effective because PCM is able to absorb or release large amounts of heat or cold with comparatively small temperature change. This advantage may be realised in applications such as passive heating/cooling systems and domestic hot water heating. In wallboard impregnated with PCM to the level of around 3 kg/m^3 (approximately 26% by weight) the storage capacity is comparable to a 9 cm thick concrete wall or a 12 cm thick brick wall. Investigations have shown that with such a component, the daily storage capacity is around 300-400 kJ/m^2; where more PCM is included it will not melt and solidify under a typical daily temperature cycle (Neeper 2000).

Experiments have shown that the PCM wallboard concept is workable on a large scale and that the product can be integrated within a building to provide a significant thermal storage benefit; the approach provides an effective load management device in passive solar designs with a reasonable payback period (Peippo *et al* 1991). The thermal performance of PCMs in different types of concrete blocks has been reported: with high quality PCM incorporation techniques, thermal storage was increased by up to 300% (Hawes *et al* 1990). A floor heating system, with and without the presence of a PCM layer, has been developed and studied (Farid and Chen 1999). The results for a concrete floor without PCM showed undesirably large variations in the floor surface temperature, and a loss of most of the stored heat within a short period after the heating system was switched off. Conversely, the

results for the modified floor incorporating PCM showed a low surface temperature fluctuation and the ability of the floor to retain stored heat and so provide warming during the remaining period of the day. A PCM-integrated, south-oriented façade shows about 30% less heat loss, while solar heat gains are reduced by about 50%. Façade PCM panels considerably enhance thermal comfort in winter, especially during evenings. In summer, such systems show low heat gain, which reduces peak cooling loads during the day; additional heat gains in the evening can be drawn off by nighttime ventilation (Weinlader *et al* 2005). Ismail and Henroquez (2002) studied the effect of PCM optical properties on double glass panes; they conclude that a PCM filled glass window system is viable and thermally effective.

To improve the periodic heat storage and heat rejection of wall, ceiling, and floor PCMs, the system must be designed in a manner that leads to an enhanced heat transfer coefficient at the component surface. This essentially requires that air flow be directed along the surface of the PCM component to promote forced rather than natural convection. Another approach is to encapsulate PCM within the ventilation system itself. The ventilation unit then effectively stores cooling potential during the night and is able to cool the space during the day (Kenisarin and Mahkamov 2007).

From the above investigation, it can be concluded that, the variation of temperature with time clearly indicates the effect of the PCM, the larger the proportion of PCM, the longer the cooling process lasts. Thus, within a certain temperature range, the thermal mass of a building component can be significantly increased due to the phase change process, so that the thermal comfort associated with massive buildings can be attained with light construction materials. As with thermal energy storage, shifting an appreciable portion of electric load to off-peak

periods can realise significant primary energy savings for those hours because lower temperatures increase air conditioning efficiency; utility generators operating at night typically have higher electricity generation efficiencies. The impact of PCMs on building cooling and heating loads varies greatly between building types, having a greater impact on light construction buildings, such as timber frame houses. Climate also has a strong impact on PCM energy saving. Moderate climates, where the outdoor temperature often passes through the PCM transition temperature (particularly at night), will realise greater savings than climates where temperatures during the cooling season remain predominantly above or below the transition temperature (Zhu *et al* 2009). PCM achieves greater savings in moderate climates with large diurnal temperature swings and lower summer time humidity levels, i.e. where night-time ventilation can be used to cool and re-solidify the PCM without creating moisture issues (Roth *et al* 2007).

2.4 PCM Heat Sink for Electronic Heat Management

Traditionally, the thermal management of electronic components has been achieved using air as the cooling fluid. To attain a high rate of heat dissipation, thermal energy may be stored in the form of latent heat using PCMs. Different heat exchanger designs may be arrived at by incorporating PCMs into traditional heat sinks, such as the standard pin fin or the longitudinal plate fin, where electronic components must be cooled by passive means only, which involves the use of natural convection and radiation as the only heat transfer modes. As shown in figure 2-1, the temperature fluctuates around the phase change temperature more or less uniformly; in this case, a PCM with a melting temperature at the average process temperature generally buffers temperature fluctuations satisfactorily (Mehiling and Cabeza 2008).

PCMs have been demonstrated to be effective at maintaining electronic components within allowable ranges under operating conditions (Kandasamy *et al* 2007). The use of PCM-based heat sinks is an effective and practical way to cool electronic devices. The concept is simple, as it uses specific cavities filled with PCMs as the heat sink. The fins of the heat sink can be used as partitions within the PCM volume to improve thermal performance, while the PCMs keep the temperature of the electronic device below a critical temperature, usually the junction temperature of silicon, which is 90°C (Pal and Joshi 2001). Krishnan *et al* (2005) studied a hybrid heat sink model, configured from a plate fin heat sink with the tip immersed in a PCM. When air-cooling is limited, the heat is absorbed by the PCM. The results showed that the fin heat transfer rate increased with an increase in fin thickness and amount of PCM and a decreasing melting temperature. Tests have also shown that PCMs can maintain the temperature of the electronic chips within mobile devices and computers below an allowable upper limit of 50°C for two hours under transient operation, with the effectiveness of the heat storage unit depending on the amount of PCM used. The larger the amount of PCM, the longer it can stabilise temperature (Tan and Tso 2004). Proper sizing of a finned-composite heat sink, with base metal fins placed vertically inside the PCM path, will ensure effective operation until all latent heat storage is exhausted (Akhilesh *et al* 2005). The hybrid heat sink concept combines passive and active approaches and may be achieved by immersing the tip of a plate fin heat sink in the PCM: the improved performance of such a hybrid heat sink compared to a heat sink without PCM under identical conditions has been reported by Kenisarin (2010). Huang *et al* (2004) experimented with R25 paraffin attached to an aluminium-finned plate, with natural ventilation and an outdoor characterisation

undertaken for the UK. A 40 mm deep PCM layer was shown to provide significant PV temperature control and limit temperature rise in PV devices. They conducted further experimental and analytical investigations to study the impact of finned and high thermal conductivity materials during PCM melting and solidification. The effects of convection and crystalline segregation was studied (Huang *et al* 2006a; Huang *et al* 2006c; Huang *et al* 2008; Hasan *et al* 2010; Huang *et al* 2011) and it was shown that the Rayleigh Number varies with the metal fin spacing. They used RT27 PCM with different internal finned systems. After the PCM is fully melted, the Rayleigh Number decreased when the fin spacing was reduced while at a certain fin spacing the convection effect increased the heat transfer rate. However, the convection effect is limited when the fin spacing is less than 12 mm. Huang *et al* (2006b) showed that for systems simulated with appropriate boundary conditions, the 2D model predictions compared well with those of a 3D model. The 3D model was used to predict the temperature distributions when the heat transfer to the PCM was enhanced by high thermal conductivity pin fins. A PCM solution for the thermal management of portable electronic devices was investigated experimentally and numerically to determine the effects of various parameters such as power input (Kandasamy *et al* 2007). To achieve effective cooling it is important to ensure that the operation period of the electronic device does not exceed the time of full melting. The numerical procedure was used to optimise the geometry of a PCM heat sink when used in an extreme environment.

PCMs are also used to reduce thermal joint resistance in microelectronic systems. PCMs in such applications consist of a substrate, such as aluminium foil, supporting a PCM such as paraffin. At some melting temperatures T_{melt}, the PCM

melts then flows through the micro-gaps, expels the air, and fills the voids completely. After the temperature of the joint falls below T_{melt}, the PCM solidifies. Depending on the level of surface roughness, out-of-flatness, and thickness of the PCM, a complex joint is formed. Thermal tests reveal that the specific joint resistance is small relative to the bare joint resistance, with air occupying the micro-gaps (Jamnia 2000). The thermal performance of a ventilated panel heating unit with paraffin as latent heat storage was developed as a storage heater utilising off-peak electricity (Farid and Chen 1999). The heater comprises multiple units filled with paraffin wax and arranged in a vertical rectangular container. During the charge cycle, heat is supplied to the units via an electrical heater fixed at the centre axis of each unit; the heat is recovered by circulating air through the spaces between the units. This unit may be used to shift the electrical load from on-peak hours to off-peak hours while delivering sufficient heating to the living space during charge and discharge periods.

Because of the direct contact between the PCM's and heat exchanger components in the HVAC systems, corrosion represents a main disadvantage especially if hydrated salt PCMs are used. Farrell *et al* (2006) examined samples from commonly used materials in heat exchangers, predominately copper and aluminium, to determine the corrosion rates with two types of salted hydrate (Sodium Sulphate Decahydrate and Sodium Chloride, called PlusICE E17) and (Sodium Acetate and additives, called ClimSel C18)). Corrosion effects (mass loss) were observed in both samples (a greater rate with copper), with high pitting corrosion in the aluminium sample. The different parameters that govern the heat transfer are heat absorbed, PCM thickness, radiation coefficients, convection coefficients, and

ambient temperature. The analysis showed that cyclic charges and discharges would not be achieved unless the supplied heat exceeds a certain value, which is independent of PCM thickness. The temperature of the plate in contact with the ambient air may be readily controlled and made comfortable to the occupants (Laouadi and Lacroix 1999).

2.5 PCM Modelling

Modelling packages exist (e.g. Energy Plus, TRNSYS and ESP-r) that include phase change algorithms based on enthalpy or apparent specific heat methods, with different models for building components implementing different types of PCMs (e.g. Heim and Clarke 2004; Ibanez *et al* 2005). Researchers have focused on the effect of latent heat storage and PCM behaviour on the temperature reduction of zones and peak load shifting under different constructions and climate conditions. Their results show temperature reductions of the order of 2.8-4 K for PCMs with a phase change temperature between 23°C and 25°C and latent heat between 45 kJ/kg and 58 kJ/kg. Alawadhi (2008) and Lamberg *et al* (2004), employing FEMLAB and MATLAB respectively, have shown that the enthalpy and apparent heat capacity methods give rise to similar estimations for the temperature distribution of the PCM in both melting and solidification phases. A common finding from previous work is that the modelling of PCM behaviour during the phase transition is not adequate. It is especially important to account for the sub-cooling effect within the phase transition and the convection effect in the liquid phase, especially in PCM-based heat exchangers where the PCM is used with effective thickness.

2.6 Building-Integrated Photovoltaic Panels

It has been reported that the world PV module capacity in 2004 was 1195 MW, representing a 57% increase from 2003 (716 MW). Japan leads the way with production increasing by 65% to 602 MW in 2004. European production increased by 49% to 314 MW, whilst in the United States production increased by 35% to 139 MW. In the rest of the world, the total production increased by 67% to 140 MW (Maycock 2005). Europe is leading the way with almost 16 GW of installed capacity, representing about 70% of the global 22 GW of PV electricity generation capacity at the end of 2009, while Japan (2.6 GW) and the United States (1.6 GW) are following behind (Jager-Waldau 2010). Recently, a number of governments (e.g. Germany, Greece, Italy and the UK) introduced a Feed-in Tariff Scheme (FITS) to support investment in low carbon technologies (Krajacic *et al* 2010, Chua *et al* 2011, and Danchev *et al* 2010). FITS is seen as an effective way to encourage the residential sector and small businesses to install PV technology by paying a premium price for the generated electricity (Zahedi 2010). This encourages consumers to produce part of the electricity they need by on-site PV generators. For each kWh of electricity that these PV systems generate, the owner is paid at a rate greater than the retail price that the owner would otherwise pay to the utility. One application for solar cells is building-integrated PV usually in the form of a glass-PV-glass module in a broad variety of shapes and sizes. The mono- and poly-crystalline or amorphous silicon solar cells can be embedded into a resin or EVA foil between two glass panes. The resulting PV module is a building element like standard glass panes and can be integrated into the facade or roof structure of a building (Benemann *et al* 2001). Organic PV cells show an important potential for development in the search for low-

cost modules for the production of domestic electricity, with a nominal 10% electrical efficiency as the research target for the next few years. The long-term objective of such research is to reduce the cost of PV modules. Such cells will obviously make soft and possibly bendable or foldable PV modules. They will be adapted to the fabrication of solar roofs, but also sails, tents and all kind of plastic outdoor furniture or portable devices. Importantly, plastic solar cells will permit the orientation of future generations of photovoltaic solar cells toward a low-cost technology with a typical (based on 2002 prices) 1 €/W target (Nunzi 2002). Where solar panels are used as walls, roofs and shading devices, they provide a dual purpose because of the decrease in the amount of construction materials required as well as the production of electricity (and sometimes heat). One of the greatest advantages is that the PV component's maximum power production occurs when the building is experiencing its peak solar load, therefore potentially increasing the energy savings. For example, offices have a good PV potential because their electricity demand is significant year-round and because demand is highest between 9 a.m. and 5 p.m. in general. Thus, the match between demand and PV supply is superior (Thomas *et al* 2010). The installation of PV systems in buildings has important benefits. For example, no additional areas are necessary because the solar generator can be mounted on existing parts of a building, such as the roof or facade; flat roofs are especially suitable because the PV components can be mounted in optimal orientation and inclination. By installing components on sloped roofs or on facades, it is possible to use only the south-oriented areas of the buildings. The main disadvantage of placing panels on facades is that they are oriented in a non-optimal direction. In this case, the solar radiation incidence angle will be large during

summer months (usually above 65˚C), decreasing the amount of solar energy that can be absorbed. More than 80% of the solar radiation falling on PV cells is not converted to electricity, but is either reflected or converted to thermal energy as shown in figure 2-3. This leads to an increase in the PV cell's working temperature and, consequently, a drop in electricity conversion efficiency (Ji *et al* 2007). In the summer, with high ambient temperatures, the PV temperature can reach about 70˚C. If the PV is insulated at the rear side, it can only lose heat from the front side, which reduces its heat loss capability. If possible, an air gap should then be introduced between the PV and the building structure behind it to allow cooling of the PV laminate by natural convection (Yang *et al* 2001).
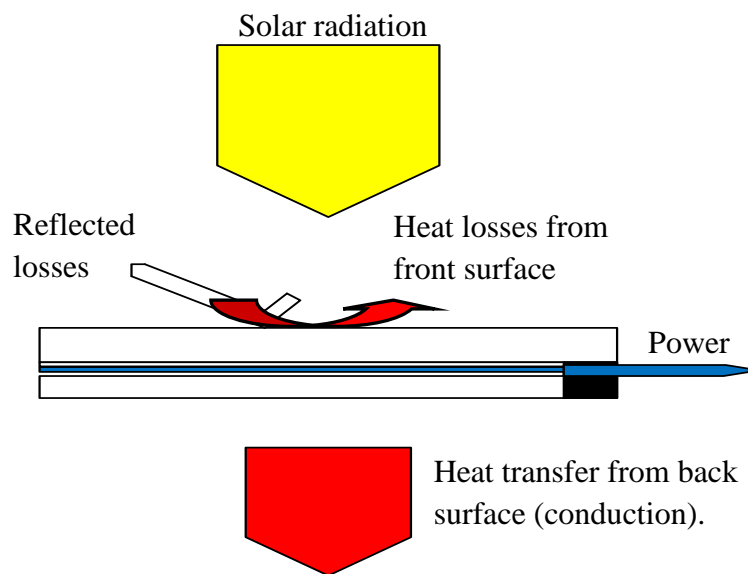
Figure 2-3: Schematic of principal energy flows of a solar cell emphasising that a significant proportion of the energy is available as heat.

2.7 Effect of High Temperature on Photovoltaic Cell Efficiency

Operating temperature plays an essential role in the PV conversion process. The electrical efficiency, and hence the power output, of a PV cell depends linearly

on the operating temperature (Skoplaki and Palyvos 2009). The power rating of a PV component is assessed under Standard Test Conditions (STC) of 1000W/m^2 irradiance corresponding to a 1.5 air mass spectral condition and a cell temperature of 25°C (Breteque 2009). Module manufacturers sometimes specify the Nominal Operating Cell Temperature (NOCT); this is determined for an irradiance of 800 W/m^2, an ambient temperature of 20°C and a wind velocity of 1m/s. The drop in performance with crystalline silicon products for each degree centigrade increase in cell temperature above 25°C is approximately 0.4–0.5%, for crystalline silicon cells. For amorphous silicon cells, the effect is roughly half of this depending on the specific production process (Roberts and Guariento 2009). As peak irradiance levels are generally attained only for a few hours around solar noon, and as the PV cell temperature often rises to 30°C–50°C rather than 25°C, the peak power under STC are unlikely to be observed under real field conditions. Field test data from a 50 kW PV system installed at the Nara Institute of Science and Technology were analysed by Nishioka *et al* (2003). It was found that the system operated in a wide temperature range throughout the year, where the maximum average module temperature was 44°C in July and the minimum average module temperature was 13°C in February. As a result, it was found that the annual output energy of the PV system increased by about 1% for each reduction of 1°C. This result indicates that it is important to consider the temperature characteristics in PV cell development. In PV modules only a small part of the absorbed irradiance, about 10–15%, is converted into electricity, with mainly heat being produced as shown in figure 2-3. This heat can be used to heat buildings, but it reduces the electrical power of the PV generator due to the module's rise in temperature. It is important to consider the module temperature of a

PV system operating in an actual environment because the standard test conditions of PV modules are not representative of field conditions. Designs for building-integrated PV need to consider cooling from the outset by allowing air to flow over the back of the modules to maintain high performance. The efficiency can be improved by cooling the cells, and some systems have been designed to make use of the heat absorbed by the cooling fluid in solar heating applications. It is also likely to be necessary with all types of modules to avoid unwanted heat gain into the space, which could cause discomfort and increase cooling loads further (Eicker 2003).

Most PV facades are built as curtain walls in front of thermally insulated buildings with air ducts in between. The convective and radiation heat exchanges at the module rear are especially influenced by the installation situation. The general indicative values of power reduction for crystalline silicon modules in various roof mountings are shown in table 2-1 (Roberts and Guariento 2009).

Active ventilation with PV facades allows a reduction of cell operating temperatures of the order of 18 K, resulting in an 8% increase in electrical energy output at an air velocity of about 2 m/s (Krauter *et al* 2001). Cell temperatures increase by ~20.7 K for thermally insulated PV facade elements without cooling; this causes a 9.3% loss of electrical yield. PV facade elements combined with a water-cooling system, which could also serve for hot water heating, lower the operating cell temperature by ~20K and increase the electrical yield by 9% relative to conventional PV facades (Krauter *et al* 2001). The loss of efficiency due to the raised PV array temperature can be reduced by heat removal from the rear surface into a cooling duct in which air flow is induced passively by buoyancy and wind forces.

Table 2-1: General indicative values for power reduction for crystalline silicon modules in various roof/facade mountings compared to the power output of a completely freestanding array 22°C warmer than ambient.

Roof mountings	Vertical façade mounting
With a large gap: -1.8% reduction in PV modules power output. 28°C warmer than ambient.	Good ventilation: -3.9% reduction in PV modules power output. 35°C warmer than ambient.
With good ventilation: -2.1% reduction in PV modules power output. 29°C warmer than ambient.	With poor ventilation: -4.8% reduction in PV modules power output. 39°C warmer than ambient.
With no ventilation: -5.4% reduction in PV modules power output. 43°C warmer than ambient.	With no ventilation: -8.9% reduction in PV modules power output. 55°C warmer than ambient.

It has been shown that when the PV component temperatures are highest and efficiency is most adversely affected, there exists an optimum value of the depth of the duct such that, for a given set of operating conditions, the temperature of the heated wall will have the lowest possible value. For a duct of length L, long enough for the flow to become fully developed, the optimum conditions is found to occur when the ratio L/D is about 20, where D is the hydraulic diameter (Brinkworth *et al* 2006). The value is not affected much by other variables, and in particular is nearly independent of the inclination of the array, so that similar duct proportions are appropriate for most PV installations, from those integrated into vertical facades to those in roofs of typical slope.

For thermal regulation of PV claddings, the general effects of the operation of thermal regulation ducts show that the mean velocity of the induced air flow is typically less than 0.5 m/s, but a reduction of cell operation temperature of 15-20 K can be obtained with significant increase in efficiency and reduction in heat gain to the building (Brinkworth *et al* 1997). In addition, the outlet temperature of air increased to 66°C with the lowest mass flow rate of 0.02 kg/s and 54°C with the highest mass flow rate of 0.05 kg/s. This behaviour may be explained by longer contact times of air with the hot surfaces inside the collector, and a collector efficiency increase with increasing mass flow rate of fluid. The temperature of absorber surfaces increased up to 71°C depending on the incident solar radiation. The corrugated geometry collector is more efficient than the flat-plate collector, with the maximum efficiency for a corrugated collector being 55% as opposed to 17% for a flat-plate collector (Benlia and Durmus 2009).

From the above investigations it can be concluded that for most PV technologies the hotter the air the lower the efficiency. PV modules work well during high solar radiation and low ambient temperature. During high air temperature days there is likely to be significant de-rating of power output. When the average ambient temperature is over 23°C and the incident solar radiation above 400W/m^2, conventional air-cooling arrangements are insufficient to maintain good PV performance (Huang *et al* 2011). Consequently, it is important to consider the climate influence on cell efficiency. PV cells convert approximately 6-18% of incoming irradiance into electrical energy. The rest is reflected, re-radiated or lost as low temperature heat. The build-up of heat provides an impetus to remove unwanted heat from behind PV modules by using fluid flow to utilise the thermal energy.

Active heat dissipation using air or water cooling introduces costs associated with both pumping and increased system maintenance – although these costs can be offset if the captured thermal energy can be utilised in the building. The main purpose of PCM is to control the PV cell temperature to around the ambient temperature. In a PV/PCM component, the PV becomes a heat source when its temperature rises above the melting temperature of the PCM. When the PCM temperature reaches the phase change limit, the PCM becomes a heat sink, absorbing heat from the PV contact surface and exchanging heat with the external environment, which determines the charging-discharging direction and efficiency of the PCM phase change cycle. The time to complete the charging and discharging process depends on the PCM and the diurnal ambient temperature difference. If the synchronisation between the phase change temperature and the daily change in ambient temperature is achieved then it is possible to control the rise in temperature of the PV cell. To cool the PV cell to a temperature less than ambient requires the use of a cooling fluid such as water with a temperature less than the prevailing external air temperature.

2.8 Latent Heat Storage and Moving Boundary Phenomena

Heat transfer problems in melting and solidification processes is termed the moving boundary problem; it is a complicated phenomenon in which the solid–liquid boundary moves depending on the speed at which the latent heat is absorbed or lost at the boundary (Ozisik 1994). When the material that solidifies is pure, the solidification occurs at a single temperature, as shown in figure 2-4 (solid curve).

But when it is impure or, as in the case of a compound, the solidification takes place over a range of temperatures, causing a two-phase, 'mushy' region to form between the solid and liquid volumes as shown in figure 2-4 (dash curve)

(Mehling and Cabeza 2008). It can be seen from figure 2-4 that specific heat exhibits a non-linear relationship with temperature throughout the phase change process; in general, the thermal conductivity and density also change.
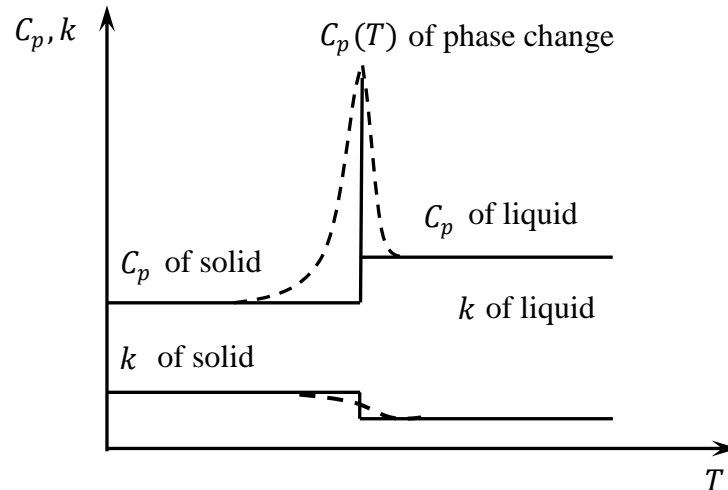
Figure 2-4: Temperature dependent specific heat and thermal conductivity for:

▬ pure materials and

– – compound materials.

Several studies have been undertaken to examine the behaviour of these thermal properties throughout the phase change, based on differential scanning calorimetric and temperature-history methods (L'azaro *et al* 2006). In their experimental study, He *et al* (2003) generated polynomial equations that represent the behaviour of the phase change heat capacity; these relations may be used in the numerical simulation of PCM systems. In this way the phase change process is modelled by directly representing the variation in the thermo-physical properties within the PCM.

The fundamental equation governing the transient heat transfer with a moving phase front is:

| Rate of heat liberated during solidification per unit area of interface | $=$ | Conductive heat flux in the negative (x) direction through the solid phase | $-$ | Conductive heat flux in the positive (x) direction through the liquid phase |

Or, stated mathematically:

$$\left(q_{liq} - q_{sol}\right)^{x=X(t)} = \rho L \frac{dX(t)}{dt} = -k_l \frac{\partial T^{-x,t}}{\partial x} + k_s \frac{\partial T^{+x,t}}{\partial x}, \ \ t > 0 \qquad \text{2.3}$$

Where ρ, L, T and $X(t)$ represent density, latent heat, temperature and the phase change of the front position at time t respectively; and thermal conductivities are related to the solid and liquid phases (k_s and k_l) respectively. From equation 2.3, the rate of change in latent heat equals the amount by which the heat (enthalpy) 'jumps' across the interface; this is termed the Stefan Condition (Ozisik 1994). The exact solution for the Stefan equation for phase change problems is limited because they are bounded by idealised situations involving semi-infinite or infinite regions of PCM and are subjected to simple initial conditions (Alexiades and Solomon 1993). Because of the non-linear nature of the phase change phenomenon, solutions are obtained by approximate analytical techniques or, more precisely, by numerical means (Habib 1971). Numerically, the transient differential equations representing heat transfer with phase change is given by equation 2.4:

$$\frac{\partial h}{\partial t} = \nabla(k \cdot \nabla T) \qquad \text{2.4}$$

By introducing an enthalpy method, the phase change problem becomes simpler and the governing equation is similar to the single phase equation; the advantage then is that there is no condition to be satisfied at the solid–liquid interface

as it automatically obeys the interface condition, and the enthalpy formulation allows a mushy zone between the two phases as shown in figure 2-5 Alexiades and Solomon (1993). Phase change problems are usually solved by the implicit finite difference method, which is preferred because of its ability to accommodate a wide range of time steps without the restriction of stability criteria.
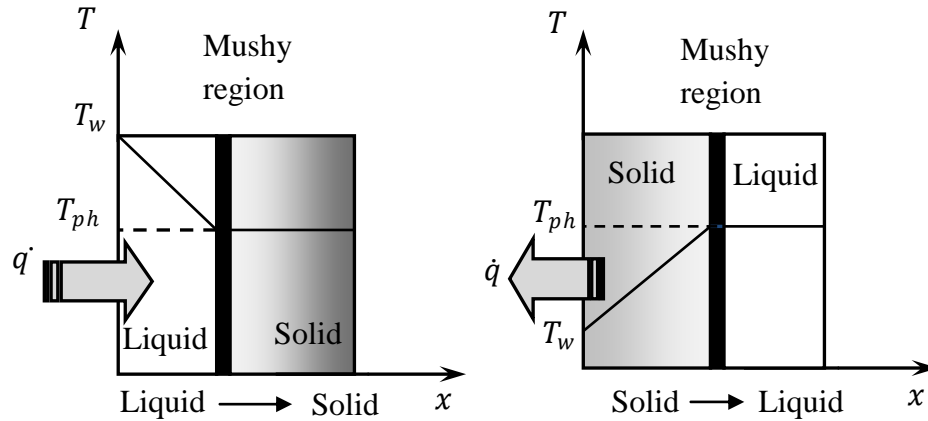
Figure 2-5: PCM layer under heating condition if $T_w > T_{pcm}$ and cooling if $T_w < T_{pcm}$.

Moreover, finite difference methods can solve equation 2.4 by assuming a linear release of latent heat over the mushy region where the variation of $H(T)$ and temperature is taken from experimental data (as in Differential Scanning Calorimetry) (Ozisik 1993; 1994). The boundary conditions used in the heat transfer equations employing the enthalpy method are:

$H = C_p T$ for $T < T_m$ solid region

$H = C_p T + \frac{T - T_m}{T_s - T_m} L$ for $T_m \leq T \leq T_s$ mushy region   2.5

$H = C_p T + L$ for $T > T_s$ liquid region

2.9 PCM Charging and Discharging Performance

There are a number of approximate formulas for estimating the freezing and melting times of different materials having a range of shapes as given by the American Society of Heating, Refrigerating and Air-Conditioning Engineers (Delgado and Da-Wen 2001). For illustration, if it can be assumed that the freezing or melting occurs at a single temperature, the time to freeze or melt t_m for a body that has shape parameters P and R, thermal conductivity k initially at a melting temperature of T_m, and which is exchanging heat with an ambient condition T_{amb} is given by (Kreith 2000)

$$t_m = \frac{L\rho}{|T_m - T_{amb}|}\left[\frac{Pd}{\bar{h}} + \frac{Rd^2}{k}\right]$$ 2.6

where L is latent heat (kJ/kg) d the diameter of the body if it is a cylinder or a sphere or thickness if an infinite slab, and P and R are shape coefficients for a number of body forms as given in table 2-2.

Table 2-2: Shape factors for equation 2.6 (ASHRAE 1993).

Forms	P	R
Slab	1/2	1/8
Cylinder	1/4	1/16
Sphere	1/6	1/24

To use equation 2.6 for the solidification process k and ρ should be the values for the substance in its solid state; when melting, they relate to the unfrozen

state (liquid). Alexiades and Solomon (1993) and Solomon (1979a) provide analytical equations for estimating the time needed to melt a simple solid body initially at fusion temperature T_m. Action occurs in one phase (liquid) only so that the problems are axes and spherically symmetric for cylindrical and spherical bodies respectively.

The melting process for differently shaped bodies can be characterised by a single geometric parameter r in the body domain $0 \leq r \leq l$ using a shape factor ω defined by:

$$1 + \omega = \frac{lA}{V}$$
2.7

Where
$$\omega = \begin{cases} 0 & \text{for a PCM slab insulated at one end.} \\ 1 & \text{for a cylinder.} \\ 2 & \text{for a sphere.} \end{cases}$$

For the case where $T_f > T_m$ is imposed at the boundary at $t = 0$, the melt time t_m can be estimated from

$$t_m = \frac{l^2}{2\alpha_l(1+\omega)Ste_l}\{1 + [0.25 + 0.17\omega^{0.7}]Ste_l\}$$
2.8

Which is valid for $0 \leq Ste_l \leq 4$; Ste is the ratio of sensible heat to latent heat.

If the heat input is convective, with a heat transfer coefficient h from a fluid at temperature T_f the approximate melt time from equation 2.9 is (Solomon 1979b)

$$t_m = \frac{l^2}{2\alpha_l(1+\omega)Ste_l}\left\{1 + \frac{2k_l}{hl} + (0.25 + 0.17\omega^{0.7})Ste_l\right\}$$
2.9

Which is valid for a Stefan Number in liquid of $0 \leq Ste_l \leq 4$ and Biot Number $hl/k_l \geq 0.1$. Equation 2.9 is claimed to be accurate to within 10% (Kreith 2000). Numerically, in the boundary layer, an additional thermal resistance acts between the heat transfer fluid and the heat exchanger wall, so that the temperature change from T_m to T_f is not just across the storage material, as shown in figure 2-6.
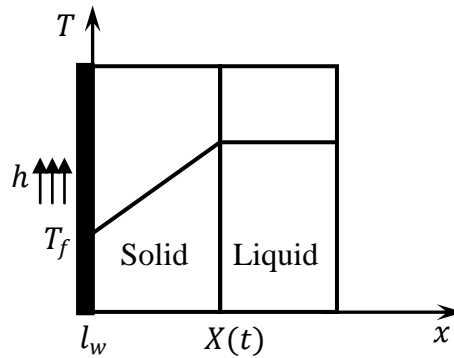
Figure 2-6: Cooling of a semi-infinite PCM layer with boundary effects.

Consider first the solidifying process on a flat cooled wall, as shown in figure 2-6. The wall with thickness l_w and thermal conductivity k_l will be cooled by a fluid having a temperature T_f whereby the heat transfer coefficient h is decisive.

On the other side of the wall a solidified layer develops, which at time t has thickness (x). The liquid is assumed to already be at the solidifying temperature T_s. From equation 2.10 during the time interval dt the phase interface moves a distance of (dx) (Mehling and Cabeza 2008). This releases the fusion enthalpy (H):

$$Q = H * A * dx$$

2.10

This must be transferred as heat through the layer that is already solidified. In a quasi-steady approximation, at each time an overall heat transfer takes place

between the interface $T = T(x(t))$, and the cooling medium $T = T_f$, as in equation 2.11:

$$dQ = \dot{Q}dt = (T(x(t)) - T_f) * A/\left(\frac{x}{k_s} + \frac{l_w}{k_l} + \frac{1}{h}\right)dt$$

2.11

Where, k_s is the thermal conductivity of the solidified body. It follows from equations 2.10 and 2.11 that

$$dt = \frac{L}{k_s(T(x(t)) - T_f)}(x + \frac{k_s}{U})$$

2.12

With:

$$\frac{1}{U} = \frac{l_w}{k_l} + \frac{1}{h}$$

The solidification time (discharging time) for a total flat layer of thickness l is found by integration:

$$t_{ch} = \frac{L * l^2}{2k_s(T(x(t)) - T_f)} * \left[1 + \frac{2 * k_s}{U * l}\right]$$

2.13

Using the thermal resistance of the heat exchanger wall as $\frac{l_{extwall}}{k_{extwall}}$ and of the fluid as $1/h$, the heat flux density into the fluid is given by

$$\dot{q}(t) = \frac{1}{\frac{x(t)}{k_s} + \frac{l}{k_{axtwall}} + \frac{1}{h}}$$

2.14

and the overall heat transfer coefficient U is given by

38

$$\frac{1}{U} = \frac{l}{k_{extwall}} + \frac{1}{h}$$

2.15

The solution of equation 2.15 for the required discharge time gives

$$t_d = \frac{LX^2}{2k_s(T - T_f)}\left[1 + 2\frac{k_s}{UX}\right]$$

2.16

Numerical simulations via a finite difference method have been undertaken to examine the feasibility and efficacy of using a PCM/air composite cellular structure as a thermal protection surface (Ho and Chu 1996). The results from parametric simulations demonstrate that the effective thermal protection duration is mainly affected by the Rayleigh Number Ra, the Stefan Number Ste the PCM/air layer thickness ratio, and the aspect ratio of the composite cell. Increase of the Rayleigh or Stefan Numbers, resulting from the natural convection enhanced melting process in the PCM layer, as well as intensified natural convection flow inside the air layer, tends to degrade the thermal protection effectiveness of the composite cell. Increasing the PCM/air thickness ratio (or aspect ratio) of the composite cell will extend the effective thermal protection duration. It can therefore be concluded that a PCM/air composite cellular structure having a high aspect ratio and/or a larger PCM/air thickness ratio is preferred for effective thermal protection. The thermal performance of a hybrid heat sink used for cooling management of protruding substrate-mounted electronic chips has been studied by Farajia *et al* (2009). The power generated in electronic chips is dissipated in the n-eicosane PCM with melting temperature T_{melt} =36°C, which fills a rectangular enclosure. The advantage of this cooling strategy is that the PCM is able to absorb the high amount of heat generated

by the electronics without requiring a fan. A two-dimensional mathematical model was developed in order to analyse and optimise a heat sink.

Table 2-3: Heat transfer coefficients for layers of different materials, thicknesses and heat transfer fluids (Mehling and Cabeza 2008).

Layer material type	Thickness l (mm)	Thermal conductivity (W/m K)	Heat transfer coefficient k/l(W/m^{2}K)
PCM	1	0.5	500
		5	5000
	10	0.5	50
		5	500
Insulating material	10	0.05	5
	100		0.5
Gap filled with gas	0.01	0.01-0.03	1000-3000
	10	0.01-0.03	1-3
Gap filled with liquid	0.01	> 0.2	>20000
	10		>20
Heat transfer fluid	*Comment*	*Heat transfer coefficient h (W/m^2 K)*	
Gas	Free convection	2-25	
	Forced convection	25-250	
Liquid	Free convection	10-1000	
	Forced convection	50-20000	

The governing equations for mass, momentum and energy transport were discretised by a finite volume approach, and the model used to investigate the effects of the Rayleigh Number and the position of the bottom electronic component on thermal behaviour. Results were obtained for velocity and temperature distribution

for modules incorporating PCM. The effect of these two key parameters on the time required for the electronic components to reach a critical temperature T_{cr}, was analysed. For a layer thickness of 10 cm and a thermal conductivity of 0.5 W/m.K, the heat transfer coefficient within the PCM is significant. When the heat transfer medium is liquid, the PCM layer with thickness of 1 cm and thermal conductivity of 0.5 W/m.K can have significant thermal resistance. PCM layers with larger or lower thermal conductivity will dominate the overall heat transfer resistance. Referring to table 2-3 (Mehling and Cabeza 2008), for a layer thickness of 10 mm and a thermal conductivity of 5 W/m.K, the heat transfer coefficient with the PCM is much larger than that of a layer with gas resulting in heat transfer by free convection. More discussion will be conducted in Chapter 4.

2.10 Phase Change and the Sub-Cooling Effect

Sub-cooling is the effect whereby the PCM temperature decreases below the melting temperature beyond which heat will be released and, as a result, the material solidifies, reaching the melting temperature again (Gunther *et al* 2007). This happens because when materials solidify they create regions for solidification that reject heat to the surrounding liquid; this increases the temperature, re-melting the solid regions (PCM nucleation) again.

This process will continue until the temperature drop in the PCM liquid region reaches a critical value, causing permanent nucleation centrals of solidification, which continue to grow, and the surrounding liquid solidifies by rejecting heat into the remaining liquid. If the rejected heat equals the extracted heat by cooling the PCM container, this will keep the temperature constant and equal to

the phase change temperature, until the remaining liquid becomes less than the solid fraction. The temperature drops because the rejected heat from phase change is less than the extracted heat by cooling from the PCM as shown in figure 2-7.
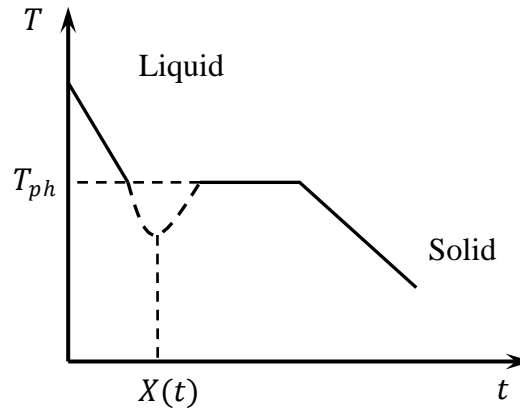
Figure 2-7: Solidifications of sub-cooled liquid.

The inorganic PCM shows strong sub-cooling especially if a nucleation agent is not added to minimise it. This effect is especially pronounced when the changes of temperature are small (e.g. in control applications); even a little sub-cooling can have a large effect on system performance (figure 2-7). In other applications (e.g. heat/cold storage), sub-cooling has a negligible effect and can usually be neglected unless the material is subjected to a high level of sub-cooling.

An exact solution for the sub-cooling problem through solidification of PCM uses the position of the phase change front $X(t)$, as part of a moving boundary problem solution. This means that the heat rejected from the solidification process increases the temperature of the hyper-cooled liquid in the adjacent layer (Alexiades and Solomon 1993; Ozisik 1994). To solve the problem analytically, the boundary condition must then satisfy the temperature and the position of the phase change. For the liquid phase $T(x,t) = T_m$, $0 < x < X(t), t > 0$ the governing heat transfer equation is

$$\frac{\partial T}{\partial t} = \alpha_{liq} \frac{\partial^2 T}{\partial x^2}$$

<div align="right">2.17</div>

While the heat transfer through the phase change front defined by

$$T(X(t), t) = T_{melt}, t > 0$$

is given by

$$\rho L \frac{\partial x(t)}{\partial t} = -k_{liq} \frac{\partial T(X(t), t)}{\partial x}, t > 0$$

<div align="right">2.18</div>

For the sub-cooling effect $T(x, 0) = T_{init} < T_{melt}, 0 < x < \infty$ is still liquid and for $X(0) = 0$:

$$T(0, t) = T_{melt} \quad \text{or} \quad -k_{sol} \frac{\partial T(0, t)}{\partial x} = 0, t > 0$$

<div align="right">2.19</div>

An analytical solution depends on the phase front location, which in turn depends on similarity (Alexiades and Solomon 1993).

By setting $\zeta = x/\sqrt{t}$:

$$X(t) = 2\lambda \sqrt{\alpha_{liq} t}$$

<div align="right">2.20</div>

$$T_{liq}(x, t) = T_{init} + B \, erfc\left[x/2(\alpha_{liq} t)^{1/2}\right]$$

<div align="right">2.21</div>

where B is an arbitrary constant. This equation satisfies the boundary condition and also the interface condition (Ozisik 1994):

$$T_{melt} = T_{init} + Berfc(\lambda)$$

<div align="right">2.22</div>

where:

$$\lambda = \frac{X(t)}{2(\alpha_{liq}\,t)^{1/2}}$$

<div align="right">2.23</div>

Equation 2.22 is solved for the B coefficient:

$$B = \frac{T_{melt} - T_{init}}{erfc(\lambda)}$$

<div align="right">2.24</div>

The temperature distribution can then be found by introducing B into equation 2.22:

$$\frac{T_{liq}(x,t) - T_{init}}{T_{melt} - T_{init}} = \frac{erfc\left[x/2(\alpha_{liq})^{1/2}\right]}{erfc(\lambda)}$$

<div align="right">2.25</div>

where $(erfc)$ is a complementary error function λ represents the root of equation 2.25; knowing λ allows the location of the solid-liquid interface $X(t)$ to be determined along with the temperature distribution (x,t) in the liquid phase.

λ, can be determined iteratively from

$$\lambda\sqrt{\pi}e^{\lambda^2}\,erfc(\lambda) = Ste_{init}$$

<div align="right">2.26</div>

Where, the initial Stefan Number is given by

$$Ste_{init} = \frac{C_p(T_{melt} - T_{init})}{H}$$

<div align="right">2.27</div>

This solution is true only if $0 \leq Ste_{init} < 1$ and, accordingly, only if

$$T_{melt} - \frac{L}{C_{pliq}} < T_{init} \leq T_{melt}$$

<div align="right">2.28</div>

From this condition, it is clear that the liquid should not be hyper-cooled initially. The numerical modelling of sub-cooling problems in the literature can be divided into two groups. One focuses on the mathematical challenge of the moving

boundary problem, often assuming simplified properties of the PCM in order to allow the mathematical modelling (Ozisik 1994).The other focuses on the storage system as a whole, seeking a method to determine the power output of the storage for different storage geometries and heat exchanger designs (Gunther *et al* 2007). Sub-cooling should not be neglected in the design of PCM storage systems because it can have a strong impact on system performance.

Chapter 3 : ESP-r Building Modelling

3.1 Introduction

The energy requirement of buildings can be reduced dramatically if energy efficiency measures are applied, such as thermal insulation, passive solar techniques, and heat recovery. In addition, active solar technologies can be used to cover a significant part of the reduced requirement, with the technologies integrated into the envelope or building systems. The advantage of using passive and active renewable energy components together is that they directly displace the more profligate building energy systems. Due to an increase in the use of air conditioning, low temperature technologies are of particular interest because they can utilise waste heat in addition to the direct use of solar energy. Apart from electricity production and solar heating and cooling, solar energy is also used in the form of daylight. It is of paramount importance to find an optimal integration of renewable energy components such as PV and PCM.

3.2 Simulation of Buildings with ESP-r

ESP-r is a simulation program for the analysis of energy and fluid flow within buildings. The program offers users the ability to assess the impact of building-integrated renewable energy components, and is applicable in both research and design contexts. Figure 3-1 illustrates the system structure (Aasem 1993). The *Project Manager* provides the user interface, supporting the description of the building and plant configuration, which can then be subjected to a real or reasonable weather influence and simulated over time (ESRU 2002). The *Project Manager* provides access to various other support facilities as follows:

1- *Standard databases* of constructions, materials, optical properties, weather collections, event profiles and plant components. The materials database

contains the thermo-physical properties of conductivity, density, specific heat, solar absorptivity and emissivity for typical homogeneous elements and was adapted and employed extensively in the present work.

2- *Tutorial exercises* that describe modelling approaches suitable for users and experts. The present work added new model exemplars corresponding to PV/PCM integrated building design.

3- *Operation profiles* that define the time dependent variations in zone occupancy, lighting, ventilation, infiltration and appliance usage.

4- *Plant and air flow components* that allow the illustration of mechanical systems of arbitrary configuration.

5- A *simulator*, which predicts building performance based on a rigorous numerical method. The building/plant system is separated into a large number of finite volumes. Then, at each time-step as a simulation continued, an energy and mass balance is applied to all volumes, giving rise to a matrix of differential conservation equations. This matrix equation is then solved by numerical methods in terms of any user-imposed *control* objectives. In the present work this numerical scheme has been adapted.

6- The *insolation* and *shading* module predicts the time-series shading of external zone surfaces (opaque and transparent) as caused by facade and site obstructions and/or the time-series insolation of internal zone surfaces (opaque and transparent) as caused by solar access through windows.

7- The *view factor* module computes the view factors between each zone surface for use by the simulator to evaluate internal longwave radiative exchanges.

8- The *results analysis module* accesses the time-series of state variables as generated by the simulator and provides a range of analyses.

Within ESP-r a building model comprises finite volumes representing parts of building spaces, HVAC components and renewable energy systems, with each part represented by a nodal network within which energy interactions take place. At each node, the conservation of mass, energy, and momentum are applied. The system governing equations (Clarke 2001) describe the physical processes occurring within each control volume, e.g. heat conduction, heat storage, airflow, moisture flow, convection, radiative exchanges etc. Sets of equations relating to each zone are grouped within an overall system matrix equation, which is organised according to a strict protocol. Solution of this matrix equation, with weather data and imposed control objectives as boundary conditions, defines the thermodynamic state of the building as it evolves over time.
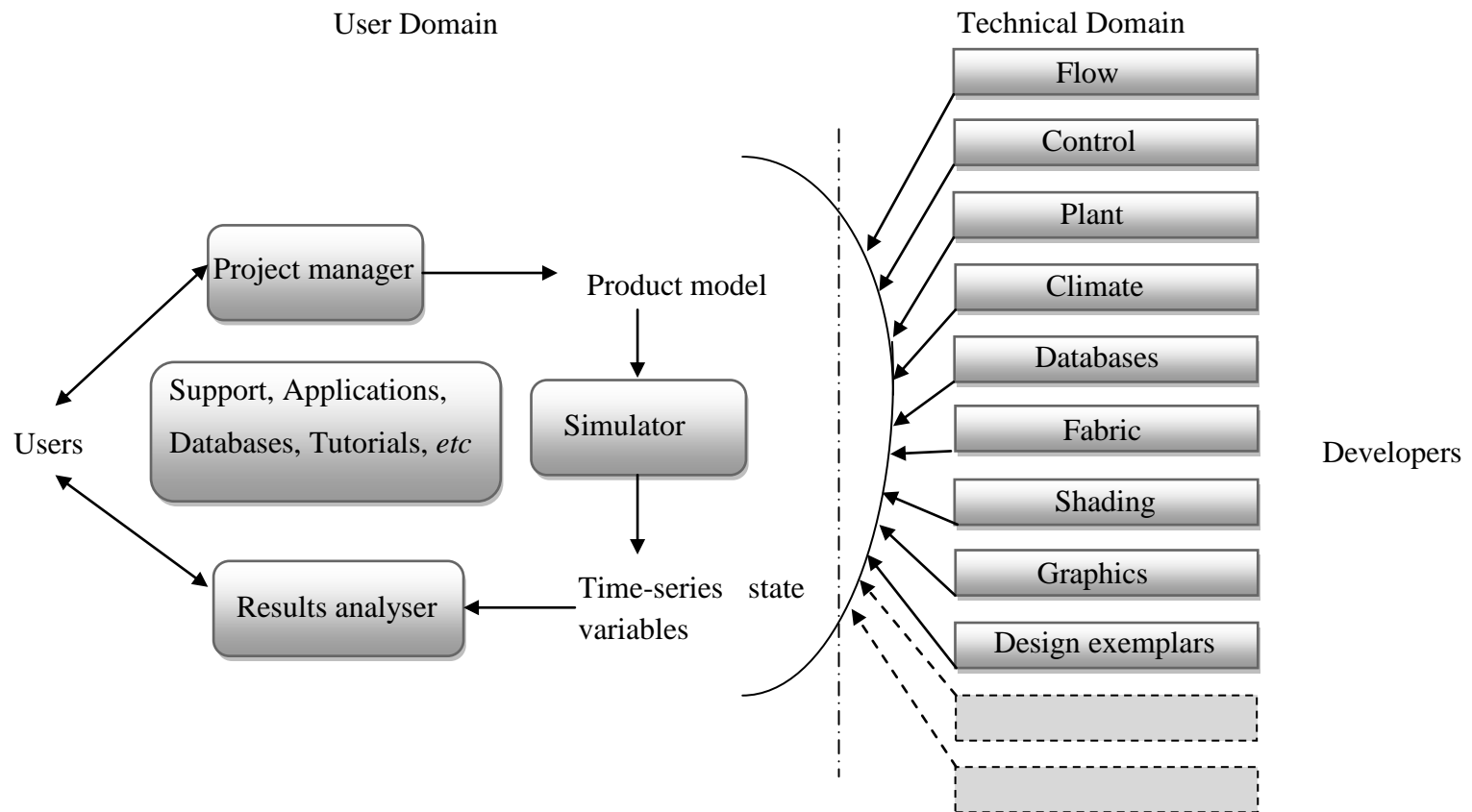
Figure 3-1: ESP-r system structure (after Aasem 1993).

For a one-dimensional conduction model, each intra-constructional node has two conduction connections, while surface nodes have one. Depending on the boundary conditions, the other possible connections for construction surface nodes are as shown in figure 3-2.
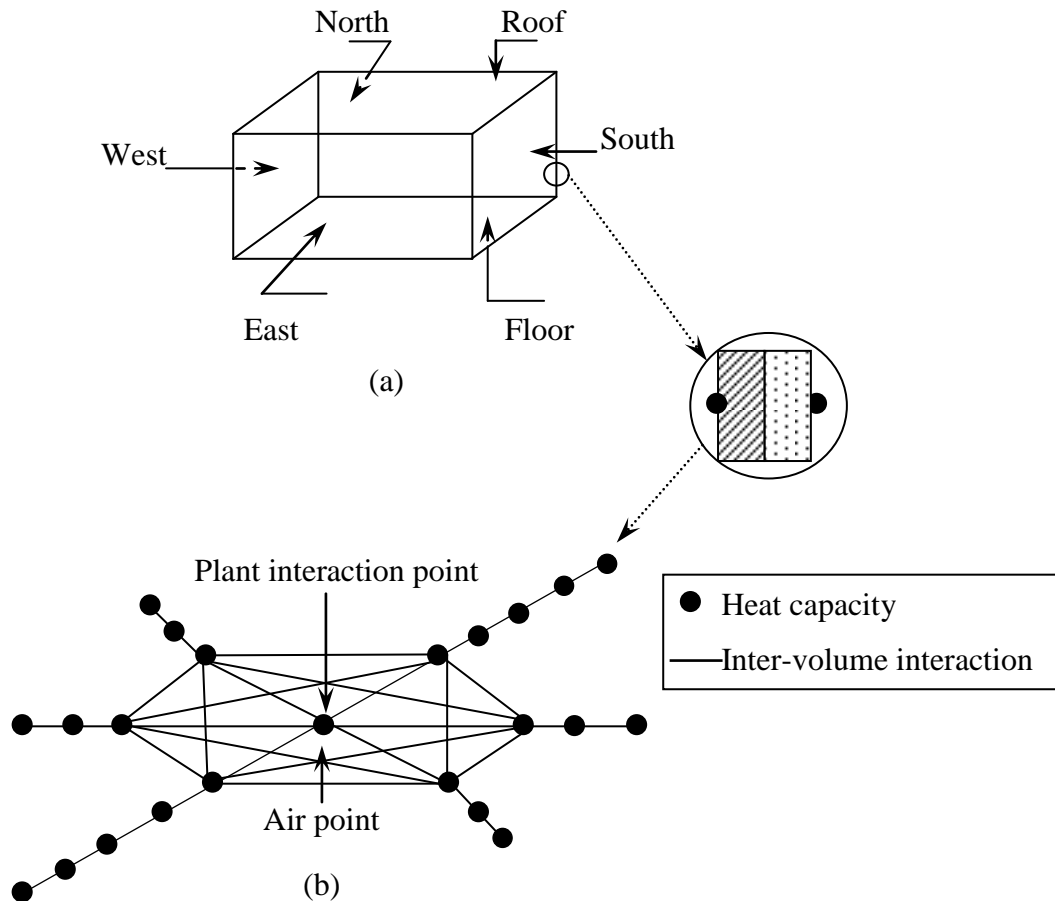
Figure 3-2: (a) A single zone system and (b) the equivalent discretisation scheme (after MacQueen 1997).

The theory of ESP-r is documented elsewhere (Aasem 1993; Clarke 2001; Hand and Strachan 1998; Hansen 1991; Kelly 1998; MacQueen 1997; Nakhi 1995; Negrao 1995). In use, a Project Manager controls model creation, simulation, and results analysis, and provides a graphical interface between the user and the underlying data model. It controls database maintenance, model manipulation, and

simulation processing via equation solvers that are customised to each model domain (e.g. thermal processes, electric power flow, air flow *etc*.). This enables an optimised treatment of the disparate equation-sets. In this manner, one solver might processes equations relating to a network air flow model to resolve inter-zone flow, while another processes equations relating to a Computational Fluid Dynamic domain to resolve intra-zone air movement (Beausoleil-Morrison 2000). Inter dependencies are handled by passing information between the solution domains on a time step basis, thus allowing the global solution to evolve in a coupled manner. The ESP-r system introduces a mathematical model of transient conduction, which is sensitive to the relative positions of the constituent elements and derives node specific formulations, which can be utilised to represent the conduction within any homogeneous medium by dividing the medium into a number of finite volumes tailored to the required accuracy level. ESP-r also provides a run-time link between building and plant models, which is crucial to an accurate simulation of the overall system (Clarke 2001). This makes it possible to implement the PCM algorithm in ESP-r and couple it within the PV component algorithm under a whole building energy system simulation scheme as shown in figure 3-1.

3.3 Special Material Concept in ESP-r

Special materials in ESP-r enable the modelling of materials that change their thermo-physical properties in response to some external excitation (such as solar radiation, temperature, or light intensity) (Kelly 1998). This allows building constructions embodying these materials to be treated in the same way as all other solid elements within the building fabric, while accounting for the special behaviour of these materials. The special material function of ESP-r may be applied to a

particular node within a multi-layer construction. Any node defined as a special material is then subjected to a time variation in its basic thermo-physical properties. Renewable energy components, such as PV, wind turbines, solar collectors; electro-chromic glazing and PCM can be treated as special components and associated with a node within the building. The special material will then act to store heat or convert solar irradiance to electricity.

3.4 Thermal Modelling

The equation sets comprising the building/plant model represent regions with significantly different time constants. Within the building fabric, temperatures change relatively slowly over time (e.g. sub hourly); while within the plant system temperatures and flows change relatively rapidly (e.g. sub minutely). A feature of the modular solution process is the ability to vary the frequency of solution of each equation set, enabling the overall solution to capture the thermal dynamics of the system without the need to constrain all parts to the lowest common denominator solver frequency. For example, zone energy equations may be processed at hourly intervals or less, while plant and flow equations are processed at one-minute intervals or less with two-way coupling imposed at the zone interval. The general heat equation for an isotropic, homogenous material is

$$\frac{1}{\alpha_i}\frac{\partial T_i}{\partial t} = \nabla^2 T_i + \frac{q_i}{k_i} \qquad\qquad 3.1$$

Where (q_i) is the heat generation per unit volume within region i (W/m^3) and α_i is the thermal diffusivity (m^2/s). Figure 3-3 depicts a 3 node per homogenous element

conduction scheme applied to a multi-layered construction (other schemes and representations in more than one dimension are possible in ESP-r).

Internal surface
(mixing node)

Internal node
(homogenous)

External node

$i-1$ i $i+1$

$\dfrac{\Delta x}{4}$ $\dfrac{\Delta x}{2}$ $\dfrac{\Delta x}{4}$

Internal element   External element
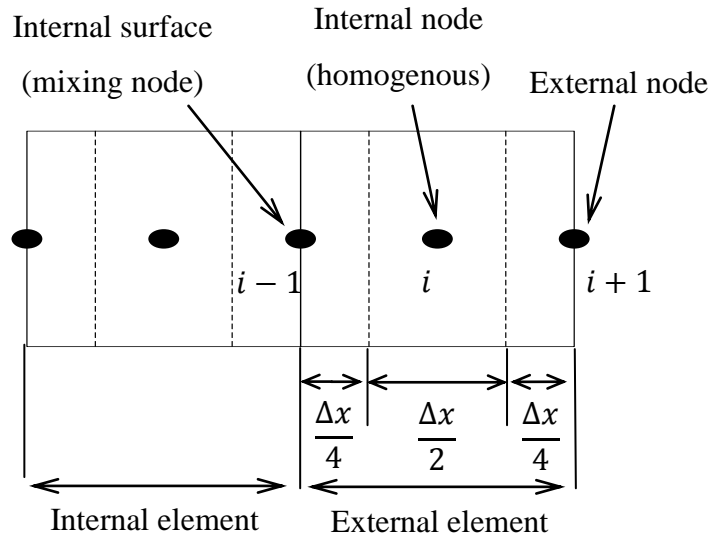
Figure 3-3: A control volume representation of a layer of homogeneous material.

This means that each multi-layered construction is presented by $(2 * NE + 1)$ nodes including surface layer nodes, where NE is the number of homogenous elements within the multi-layered construction. For an arbitrary node i situated at the centre plane of an opaque, homogenous element, the discretised form of equation 3.1 is given by:

$$
\begin{aligned}
\left[2\rho_i C_i + \frac{2\Delta t k_i}{\Delta x_i^2}\right] T_i^{t+\Delta t} &- \frac{2\Delta t k_{i-1}}{\Delta x_i^2} T_{i-1}^{t+\Delta t} - \frac{2\Delta t k_{i+1}}{\Delta x_i^2} T_{i+1}^{t+\Delta t} \\
&- \frac{\Delta t q_i^{t+\Delta t}}{\Delta V_i} \\
&= \left[2\rho_i C_i + \frac{2\Delta t k_i}{\Delta x_i^2}\right] T_i^t + \frac{2\Delta t k_{i-1}}{\Delta x_i^2} T_{i-1}^t \\
&+ \frac{2\Delta t k_{i+1}}{\Delta x_i^2} T_{i+1}^t + \frac{\Delta t q_i^t}{\Delta V_i}
\end{aligned}
\tag{3.2}
$$

For a transparent homogenous element node, the heat generation term will also include the absorption of shortwave energy as it travels through the transparent medium. The Fourier Number is the ratio of the rate of heat conduction through the control volume to the rate of heat storage within the control volume:

$$Fo_i = \frac{\left[\frac{k_i A}{\Delta x_i}\right]}{\left[\frac{\rho_i C_i V}{\Delta t}\right]} = \frac{\alpha_i \Delta t}{\Delta x_i^2} \qquad 3.3$$

With λ denoting the weighting factor between fully explicit and fully implicit representations; equation 3.2 can re-arranged as:

$$-\lambda Fo_i T_{i-1}^{t+\Delta t} + (2\lambda Fo_i + 1)T_i^{t+\Delta t} - \lambda Fo_i T_{i+1}^{t+\Delta t}$$

$$-\sum q_i^{t+\Delta t} = (1-\lambda)\, Fo_i T_{i-1}^{t} \qquad 3.4$$

$$- (2Fo_i(1-\lambda) - 1)T_i^{t} + (1-\lambda)Fo_i T_{i+1}^{t} + \sum q_i^{t}$$

Figure 3-4 depicts a node at the interface between two construction elements.
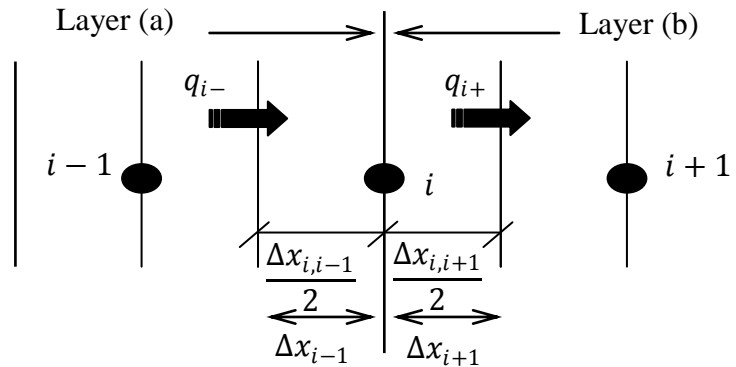
Figure 3-4: Conduction heat transfer at the interface between two layers of different materials within a composite wall.

For this situation, the discretised energy balance equation is given by:

$$\left[2\rho_{i-1}C_{i-1} + \frac{\Delta t k_{i,i-1}R_{int} + \Delta t 2\Delta x_{i-1}}{\Delta x_{i-1}(\Delta x_{i,i-1} + \Delta x_{i-2,i-1})R_{int}}\right.$$

$$\left. + \frac{\Delta t k_{i-2,i-1}R_{int} + \Delta t 2\Delta x_{i-1}}{\Delta x_{i-1}(\Delta x_{i,i-1} + \Delta x_{i-2,i-1})R_{int}}\right]T_{i-1}^{t+\Delta t}$$

$$- \left[\frac{\Delta t k_{i,i-1}R_{int} + \Delta t 2\Delta x_{i-1}}{\Delta x_{i-1}(\Delta x_{i,i-1} + \Delta x_{i-2,i-1})R_{int}}\right]T_{i}^{t+\Delta t}$$

$$- \left[\frac{\Delta t k_{i-2,i-1}R_{int} + \Delta t 2\Delta x_{i-1}}{\Delta x_{i-1}(\Delta x_{i,i-1} + \Delta x_{i-2,i-1})R_{int}}\right]T_{i-2}^{t+\Delta t} - \frac{\Delta t q_{i-1}^{t+\Delta t}}{\Delta V_{i-1}}$$

$$= \left[2\rho_{i-1}C_{i-1} + \frac{\Delta t k_{i,i-1}R_{int} + \Delta t 2\Delta x_{i-1}}{\Delta x_{i-1}(\Delta x_{i,i-1} + \Delta x_{i-2,i-1})R_{int}}\right.$$

$$\left. + \frac{\Delta t k_{i-2,i-1}R_{int} + \Delta t 2\Delta x_{i-1}}{\Delta x_{i-1}(\Delta x_{i,i-1} + \Delta x_{i-2,i-1})R_{int}}\right]T_{i-1}^{t}$$

$$+ \left[\frac{\Delta t k_{i,i-1}R_{int} + \Delta t 2\Delta x_{i-1}}{\Delta x_{i-1}(\Delta x_{i,i-1} + \Delta x_{i-2,i-1})R_{int}}\right]T_{i}^{t}$$

$$+ \left[\frac{\Delta t k_{i-2,i-1}R_{int} + \Delta t 2\Delta x_{i-1}}{\Delta x_{i-1}(\Delta x_{i,i-1} + \Delta x_{i-2,i-1})R_{int}}\right]T_{i-2}^{t} - \frac{\Delta t q_{i-1}^{t}}{\Delta V_{i-1}}$$

3.5

With the coefficients established within each time step as detailed elsewhere (Clarke 2001) and as given in equation 3.6. Note that the conductivity ($k_{i\mp1}$), density ($\rho_{i\mp1}$) and specific heat ($C_{i\mp1}$) of the region (i) are volume-weighted averages of the two constituent materials (mixing properties). R_{int}, represented an added resistance (m^2.K/W) at the material interface as shown in figure 3-4. If the Fourier Number for layer (a) is given by

$$Fo_{i,i-1} = \left[\frac{\frac{k_{i,i-1}\Delta t}{\Delta x_{i,i-1}}}{\rho_{i,i-1}C_{i,i-1}\Delta x_{i,i-1} + \rho_{i,i+1}C_{i,i+1}\Delta x_{i,i+1}}\right]$$

3.6

And the Fourier Number for layer (b) by

$$Fo_{i,i+1} = \left[\frac{\frac{k_{i,i+1}\Delta t}{\Delta x_{i,i+1}}}{\rho_{i,i-1}C_{i,i-1}\Delta x_{i,i-1} + \rho_{i,i+1}C_{i,i+1}\Delta x_{i,i+1}} \right] \tag{3.7}$$

Substituting equations 3.6 and 3.7 in equation 3.4, gives

$$-2\lambda Fo_{i,i-1}T_{i-1}^{t+\Delta t} + \left(2\lambda Fo_{i,i-1} + 2\lambda Fo_{i,i-1} + 1\right)T_i^{t+\Delta t}$$

$$- 2\lambda Fo_{i,i+1}T_{i+1}^{t+\Delta t} - \frac{\Delta t q_i^{t+\Delta t}}{\Delta V_i}$$

$$= 2(1-\lambda)Fo_{i,i-1}T_{i-1}^t$$

$$- \left(2(1-\lambda)(Fo_{i,i-1} + Fo_{i,i+1}) - 1\right)T_i^t + (1$$

$$- \lambda)Fo_{i,i+1}T_{i+1}^t + \frac{\Delta t q_i^t}{\Delta V_i} \tag{3.8}$$

For a surface node i receiving radiant energy from other surfaces and convective exchange with an adjacent air node, the general heat equation is

$$\frac{k_{i,i+1}}{\Delta x_{i+1}^2}T_i^{t+\Delta t} - \sum_{s=1}^{n}\frac{h_{rs,i+1}}{\Delta x_{i+1}}T_s^{t+\Delta t} - \frac{h_{cs,i+1}}{\Delta x_{i+1}}T_a^{t+\Delta t} - \frac{q_{i+1}^{t+\Delta t}}{\Delta V_{i+1}}$$

$$= \left[\frac{2\rho_{i+1}C_{i+1}}{\Delta t} + \frac{k_{i,i+1}}{\Delta x_{i+1}^2} + \sum_{s=1}^{n}\frac{h_{rs,i+1}}{\Delta x_{i+1}}\right]T_{i+1}^t \tag{3.9}$$

$$+ \frac{k_{i,i+1}}{\Delta x_{i+1}^2}T_i^t + \sum_{s=1}^{n}\frac{h_{rs,i+1}}{\Delta x_{i+1}}T_s^t - \frac{h_{cs,i+1}}{\Delta x_{i+1}}T_a^t - \frac{q_{i+1}^t}{\Delta V_{i+1}}$$

Where, h_{cs} is the convective heat transfer coefficient at the surface and T_a the temperature of the adjacent air volume. $\sum_{s=1}^{n}h_{rs,i+1}$ are the radiativeheat transfer coefficients (W) that characterise the long-wave radiant heat transfer between this node and the n other surfaces within the zone. The term q represents solar and other

radiant gains (W) to the surface (e.g. from plant and occupants). Neglecting heat generation, equation 3.9 becomes:

$$(2\lambda Fo_{i,i+1}B_i + 2\lambda Fo_{i,i+1} + 1)T_i^{t+\Delta t} - 2\lambda Fo_{i,i+1}T_{i+1}^{t+\Delta t} - \frac{q_i^{t+\Delta t}}{\Delta V_i}$$

$$= 2\lambda Fo_{i,i+1}B_i((1-\lambda)T_o^t + \lambda T_o^{t+\Delta t})$$

$$- (2(1-\lambda)Fo_{i,i+1}(B_i + 1) - 1)T_i^t + 2(1$$

$$- \lambda)Fo_{i,i+1}T_{i+1}^t + \frac{q_{i+1}^{t+\Delta t}}{\Delta V_i}$$

3.10

where:

$$B_i = \frac{hC_i}{\frac{k_i}{\Delta x}} = \frac{hC_i\Delta x_i}{k_i}$$

3.11

The heat transfer equations can be solved numerically using the finite difference method. If $\lambda=0$, the equations will be identical to the corresponding equations for an explicit method and will become those for the implicit method if $\lambda=1$. In a Crank-Nicholson scheme $\lambda=0.5$ and the solution will be unconditionally stable (Patankar 1980) for all space and time steps (although large discretisations will adversely affect accuracy). For a homogeneous or non-homogeneous region, the heat transfer equations can be rearranged in a general form as follows.

$$C_{s,i}^{t+\Delta t}T_i^{t+\Delta t} - \sum_{i=1}^{N}C_{c,i}^{t+\Delta t}T_i^{t+\Delta t} - \frac{\Delta t q_i^{t+\Delta t}}{\Delta V_i}$$

$$= C_{s,i}^t T_i^t - \sum_{i=1}^{N}C_{c,i}^t T_i^t - \frac{\Delta t q_i^t}{\Delta V_i}$$

3.12

Where, $C_{s,i}^t$ is the self-coupling coefficient at time t, $C_{c,i}^t$ the cross-coupling coefficient, and N the number of inter-nodal layers (Clarke 2001). These coefficients will typically contain thermo-physical properties, convection/radiation coefficients, and inter-zone airflows depending upon the location of the node under consideration. From equation 3.12 it is clear that the cross-coupling coefficients contain the transport property while the self-coupling coefficients contain the storage properties. Larger cross coupling coefficients will produce a larger temperature variation while larger self-coupling coefficients will give rise to a lesser temperature variation (Nakhi 1995), i.e. the self-coupling coefficient acts as a damper for temperature variations. In general terms, any node within a multi-layered construction is constrained to the form

$$A * T_{i+1}^{t+\Delta t} + B * T_i^{t+\Delta t} + C * T_{i-1}^{t+\Delta t} + D * Q_i^{t+\Delta t}$$
$$= E * T_{i+1}^t + F * T_i^t + G * T_{i-1}^t + H * Q_i^t$$

3.13

where $T_{i+1}^{t+\Delta t}$ is the future temperature at the outer node in thermal contact with the node in question $T_i^{t+\Delta t}$ the future temperature at the node in question $T_{i-1}^{t+\Delta t}$ the future temperature at the inner node in thermal contact with the node in question $Q_i^{t+\Delta t}$ the future heat injection at the node in question and T_{i+1}^t, T_i^t, T_{i-1}^t, Q_i^t are the present temperatures and heat generation at the same nodes.

3.5 PCM Heat Capacity Method in ESP-r

PCMs are modelled in ESP-r via a 'special materials' facility. The effect of phase transition is added or extracted by appropriate adjustments to the corresponding general energy balance equation (Clarke 2001). The latent heat effect is calculated according to the effective heat capacity method. In this technique, a

temperature profile is assumed between the nodes; rather than determining an apparent capacity in terms of the nodal temperature, an effective capacity is calculated based on the integration through the control volume (Hu and Argyropoulos 1996).

$$C_{p,effc}(T) = \frac{\int C_{p,app} \, dV}{V} \qquad \text{3.14}$$

The mathematical relationship of equation 2.4 for the effective specific heat throughout the phase change is substituted by a linear relationship of equation 3.15. This relationship is experimentally determined by a differential scanning micro-calorimeter, which can be used to measures gypsum compounds with fatty acids under isothermal change of phase. The melting temperature range is from 13.7°C to 33.3°C and the heat of phase change is from 11.1 kJ/kg to 82.4 kJ/kg (Heim 2005). The linear relationship is given by

$$C_p(T) = AT + B \qquad \text{3.15}$$

Where A and B are constants with values dependent on the material used.

To simplify the mathematical model, several assumptions are employed. First, the PCM is considered self-nucleating, chemically stable and exhibits no overheating or overcooling effect. Second, gypsum composites are treated as homogeneous. Third, the heat transfer process across the PCM–impregnated gypsum board is one-dimensional. Nakhi (1995) introduced a non-linear variation of the thermo-physical properties in equation 2 .4; the result is given by equation 3.16.

$$\frac{\partial}{\partial t}\rho(T)h(T) = \nabla \cdot [k(T)\nabla T(t)] + q(t) \qquad 3.16$$

In order to change equation 3.16 to an equation in terms of the heat capacity method, some modifications need to be applied as follows.

When

$$\partial/\partial\rho \approx 0$$

and

$$\frac{\partial h}{\partial t} = \frac{\partial h}{\partial T}\frac{\partial T}{\partial t} = C_p(T)\frac{\partial T}{\partial t} \qquad 3.17$$

Equation 3.16 becomes

$$\rho(T)C_p(T)\frac{\partial T}{\partial t} = \nabla \cdot [k(T)\nabla T(t)] + q(t) \qquad 3.18$$

From equation 3.18, the nodal distribution is dependent on the thermo-physical properties of materials, which may vary throughout the simulation period. In ESP-r, a dynamically adaptive 1-dimensional grid is required to accommodate a large variation in one or more of the thermo-physical properties (Nakhi 1995). The linear relationship of specific heat C_p in equation 3.15 is substituted in equation 3.18. The phase change temperature regulates the initial thermo-physical properties (liq, sol and $effc$ representing the liquid, solid, and effective phases throughout the phase change respectively) (Halford and Boehm 2007; Heim and Clarke 2004) as follows

$$T < T_{melt} \ , C_p = C_{p,sol} \ \text{ Solid phase} \qquad 3.19$$

$$T \geq T_{melt} \ , T \leq T_{sol} \ , C_p = C_{p,effc} \quad \text{Transition phase}$$

$$T > T_{sol} \ , C_p = C_{p,liq} \quad \text{Liquid phase}$$

Where for all boundary conditions $\rho = \rho_{sol} = \rho_{liq}$ and $k = k_{sol} = k_{liq}$.

By evaluating effective heat capacity at each step, it is ensured that the method correctly accounts for the latent heat effect and the solution is independent of the artificial phase change temperature range. An assumption of a large artificial phase change temperature range is not required. The results were relatively insensitive to the time step and generally precise both on the entire domain and near the moving boundary. As a result, very small building time steps have to be used in ESP-r modelling, this method in order to overcome its shortcoming. Within the phase change field, many researchers consider thermal properties to be constant whereas they should be considered as a function of temperature through the phase change (mushy region) to represent the real situation as shown in figure 3-5.
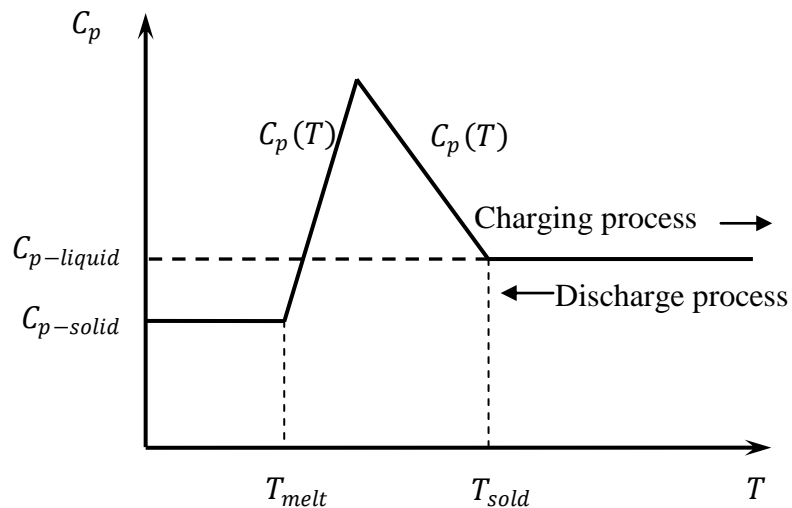
Figure 3-5: Effective specific heat during the charging and discharging process (Heim and Clarke 2004).

Companies who supply PCMs provide limited data on transitional thermo-physical properties although they do provide information for the solid and liquid phases. Therefore, the purpose of the present work is to account for the actual values of the thermo-physical properties in the transition region where high non-linearity exists. Different relations have been developed in the literature to represent the thermal properties of PCMs in the mushy region. Heim and Clarke (2004) applied a simple average of the liquid and solid phases:

$$k_{effc} = \frac{(k_{sol} + k_{liq})}{2}$$ 3.20

When the temperature of phase change is reached, the heat generation term in equation 3.4 is activated and its value is set as a function of the PCM node temperature and thermal properties. Continuous absorption of heat then maintains the PCM node temperature at a constant value (which in turn affects the neighbouring nodes in the system). The process continues until the PCM is exhausted and the PCM node temperature is allowed to change. This process can be represented by a simple counter to control the storage of latent heat at any time as a function of some material behaviour algorithm Clarke (2001):

$$T_{melt} < T_{node} < T_{solid}, \quad \sum_{1}^{n} q_i(t + \Delta t)\Delta t$$ 3.21

where n represent the number of sub-steps. During sensible cooling or heating at time t, $q_i(t) = 0$. When the temperature of phase change is reached, the counter is invoked and heat absorbed or released $q_i(t + \Delta t) \neq 0$ to ensure isothermal conditions at the PCM node; that is, the following condition is maintained:

$$T(t + \Delta t) \approx T(t)$$

The direction of phase change (heat storage or release) dictates the sign of q_i. The PCM algorithm developed in this thesis ensures the inclusion of variable thermal property behaviour, and introduces the effect of convection in the liquid phase as well as sub-cooling effects.

3.6 Modelling PV Constructions

In most construction materials (excluding PCMs), the absorption of solar radiation produces a temperature rise. The absorption of this radiation at the PV surface material node i is here represented by a heat injection $q_{e,i}$, to the characteristic surface equation as shown in figure 3-6.

Internal surface PV-EVA mixing property node $i-1$

Internal PV homogenous node i

Internal surface PV-Glass mixing property node $i+1$

Internal EVA homogenous node

Internal glass homogenous node

Internal surface EVA –PCM node

External glass mixing-property node
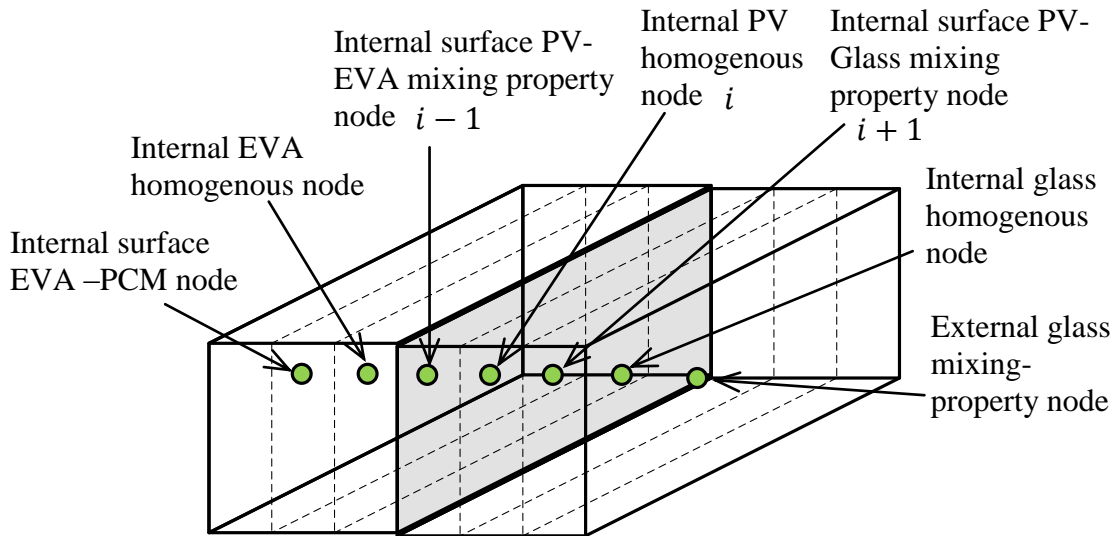
Figure 3-6: PV construction control volumes.

However, a PV material is regarded as a special material in ESP-r, as not all the absorbed solar energy is converted to heat, a proportion being converted to electrical energy and transported away as electrical current in the conducting

elements. The characteristic equation of the PV material control volumes must therefore be altered to take account of this fact by the addition of an extra term to account for the production of electrical energy (here for node i):

$$T_{i-1}^{t+\Delta t} + \left(2\lambda Fo_{i,i-1} + 2\lambda Fo_{i,i-1} + 1\right)T_i^{t+\Delta t} - 2\lambda Fo_{i,i+1}T_{i+1}^{t+\Delta t}$$

$$-\frac{\Delta t q_i^{t+\Delta t} - \Delta t q_{e,i}^{t+\Delta t}}{\Delta V_i}$$

$$= 2(1-\lambda)Fo_{i,i-1}T_{i-1}^t \qquad\qquad 3.22$$

$$-\left(2(1-\lambda)(Fo_{i,i-1} + Fo_{i,i+1}) - 1\right)T_i^t + (1$$

$$-\lambda)Fo_{i,i+1}T_{i+1}^t + \frac{\Delta t q_i^t - \Delta t q_{e,i}^t}{\Delta V_i}$$

In order to model a system over all expected operating conditions, a modelling method that uses module temperature and solar irradiance as inputs is required. PV module performance at other than standard operation condition can then be calculated by considering each solar cell as an equivalent circuit model which encapsulates the electrical characteristics of the solar cell; one such model is shown in figure 3-7 (Kelly 1998).
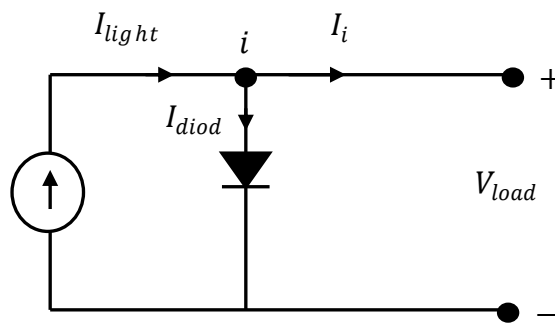
Figure 3-7: The equivalent circuit of the solar cell Kelly (1998).

The current generated by the absorption of solar radiation in the cell is termed the light generated current. The diode is included to provide a flow path for a diode

current, which opposes the flow of the light generated current. A characteristic equation can be constructed for this equivalent circuit by the application of Kirchoff's Current Law to the equivalent circuit of figure 3-7. This result in a current balance equation about electrical node i as follows.

$$I_i = I_{diod} - I_{light} \qquad\qquad 3.23$$

Where, I_i is the current flowing from node i, I_{diod} the diode current and I_{light} the light generated current (all A).

$$I_i = I_{diod} \left[\exp\left(\frac{eV_{load}}{\lambda k T_{cell}} \right) - 1 \right] - I_{light} \qquad\qquad 3.24$$

Where, e is the charge on an electron ($1.6*10^{-19}$C), k the Stefan-Boltzmann constant ($1.38 * 10^{-23}$ J/k) and λ an ideality factor representing the losses caused by imperfections in the PV material.

Chapter 4 : Enhancements to the ESP-r PCM Model

4.1 PCM Thermal Properties in Phase Change

From figure 3-5, the existence of a melting range has an influence on the melting front leading to a mushy region. The heat storage capacity, thermal conductivity, and density will therefore vary as a function of the melting range. The relation between the property and the amount of existing phase change in the mushy region can be calculated via a liquid fraction parameter f_l (Dincer and Rosen 2002), where the liquid fraction is a function of the phase temperature:

$$f_l = \frac{T - T_{melt}}{T_{sol} - T_{melt}}, \quad T_{melt} < T < T_{sol}, \text{ mushy region}$$

$$f_l = 1, \ T_{sol} < T, \text{ totally liquid} \tag{4.1}$$

$$f_l = 0, T < T_{melt}, \text{ totally solid}$$

or, for $T_{melt} < T < T_{sol}$:

Fraction of solid in mixture $= (1 - f_l)$

The mixture conductivity $= k_{sol}(1 - f_l) + f_l k_{liq}$ (4.2)

Density$= \rho_{sol}(1 - f_l) + f_l \rho_{liq}$

In addition, the overall thermal conductivity, density, and apparent specific heat become as follows.

$T \leq T_{melt}, C_p = C_{p,sol}, \ k = k_{sol}, \ \rho = \rho_{sol}; \text{Solid phase}$

$T > T_{melt}, \ T \leq T_{sol}, \ C_p = C_{p,effc}, \quad k = k_{effc}, \ \rho = \rho_{effc}$

                             (4.3)

; Transition phase

$T > T_{sol}, \ C_p = C_{p,liq}, \ k = k_{liq}, \ \rho = \rho_{liq}; \text{Liquid phase}$

Previous studies consider impregnating traditional building materials with PCM, e.g. brick, concrete, plasterboard *etc.*, and representing these by homogenous properties extracted from experiments (Hawes *et al* 1993). However, such experimental data are rarely available from suppliers. It is therefore necessary to know the weight percentage of PCM, f_{PCM} to determine the overall thermal properties of a structure:

$$k_{tot} = k_{App} f_{PCM} + (1 - f_{PCM}) k_{stru}$$

$$\rho_{tot} = \rho_{App} f_{PCM} + (1 - f_{PCM}) \rho_{stru} \qquad 4.4$$

$$C_{p,tot} = C_{p,App} f_{PCM} + (1 + f_{PCM}) C_{p,stru}$$

The low conductivity of PCM is the main factor that affects the heat storage release efficiency. Improving the thermal conductivity can be achieved by using high conductivity particles, e.g. carbon or aluminium particles, or by introducing a metal matrix within the PCM. This requires a model to describe the effective conductivity of such an arrangement:

$$k_{eff} = \frac{k_{part} \, k_{App}}{k_{part} + k_{App}} \qquad 4.5$$

4.2 The Effect of Convection in the Liquid Phase

In addition to natural convection, solid-liquid density change is an important factor that has an influence on the phase-change heat transfer. To make an accurate prediction of the heat transfer characteristics during melting or solidification, it is necessary to include both the natural convection in the melting process and the density change (Hoseon and Ro 1991). A change in density takes place between

liquid and solid phases at the melting temperature, i.e. $\rho_{liq} \neq \rho_{sol}$, and in the presence of gravity a temperature gradient induces flow due to buoyancy resulting from natural convection motion in the liquid (Alexiades and Solomon 1993). The density and dynamic viscosity of the liquid PCM depends on its temperature (Kandasmy *et al* 2007). The density can be expressed as

$$\rho_{liq} = \frac{\rho_{liq}}{\beta(T - T_{melt}) + 1} \qquad 4.6$$

Where: ρ_{liq}, is the density in the liquid phase and β the thermal expansion coefficient (0.001 K^{-1}). The dynamic viscosity of the liquid PCM can be expressed as

$$\mu = 0.001 * \exp(A + \frac{B}{T}) \qquad 4.7$$

Where A=-4.25 and B=1970.

For PCM capsules, this assumption amounts to using a maximum PCM thickness S_{max} for which the Rayleigh Number remains smaller than 5000 (Dincer and Rosen 2002):

$$S_{max} \leq \left(\frac{500 \upsilon_{liq} \alpha_{liq}}{g\beta\Delta T}\right)^{1/3} \qquad 4.8$$

where υ_{liq}, α_{liq} and β are the kinematic viscosity, thermal diffusivity and thermal expansion coefficient of the liquid phase respectively; g is the gravitational acceleration and ΔT the temperature difference between the heat source and the melting point of the PCM as shown in figure 4-1.
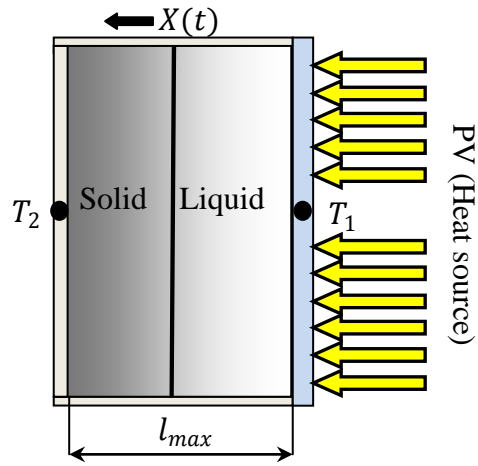
Figure 4-1: Phase change moving front.

From figure 4-1, the heat flux was assumed to be one-dimensional and orthogonal to the PV external surface, to prevent edge effectit can consider that the boundary condition on the peripheral surfaces adiabatic. Smaller values of S_{max} are desirable because of the enhanced heat transfer rate. In capsules, if the thickness is larger than S_{max} then natural convection prevails in the melting process and should not be ignored. In buoyancy driven flows, there are times in the melt when the PCM thickness is larger than the recommended values specified for l_{max}. This effect is taken into account in the model by an enhanced effective thermal conductivity k_{effc}, which is a function of the Rayleigh Number based on the melting layer thickness S_{max}:

$$k_{effc} = k_{liq}.C.Ra^n$$

4.9

$$Ra = \frac{g\beta\Delta T S_{max}^{3}}{v_{liq}\,\alpha_{liq}}$$

4.10

Where: C and n are constants determined experimentally; for a vertical heated surface C=0.12 and n=0.25, while for a horizontal plate C=0.05 and n=0.25 (Adine

and ElQarnia 2009; Laouadi and Lacroix 1999). Figure 4-2 represents the algorithm as developed in the present work and implemented within the ESP-r system. In the liquid or mixing phase, the critical thickness represents the key condition that dictates whether convection occurs.
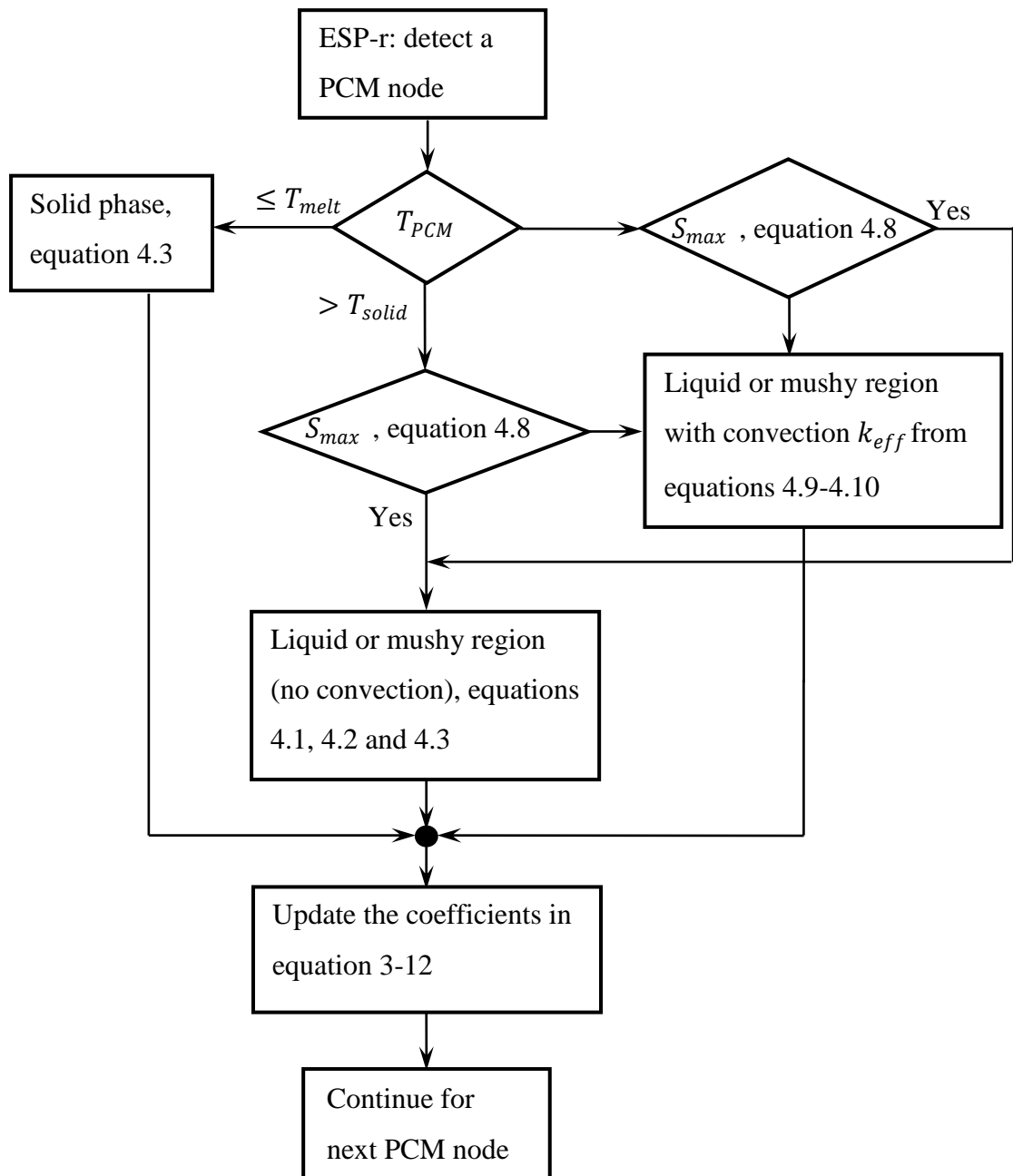
Figure 4-2: Flow chart for the simulation of convection in the liquid phase.

4.3 Sub-cooling Effects

The formation of a crystal may require the movement of atoms into the solid lattice structure; it may well happen that the temperature of the material is reduced below melting temperature without formation of solid. Thus super-cooled liquid, that is, liquid at temperatures below melting temperature, may appear; such a state is thermodynamically meta-stable. For the super-cooling curve of figure 2.7, the temperature rapidly rises back to the melt temperature when crystallization does take place. This can occur only if the latent heat released upon freezing is sufficient to raise the temperature to melting temperature, i.e., the liquid was not cooled too much. Most existing methods to calculate heat storage depend on the relationship between enthalpy $h(T)$, specific heat $C_p(T)$ and temperature. Gunther *et al* (2007) introduced a parameter to represent the degree of phase change within an enthalpy function algorithm $h(T, Phase)$, where *Phase* is either solid or liquid. The phase change velocity depends on the speed of the material crystal growth in liquid. A similar device can be applied to the apparent specific heat method as shown in figure 4-3.
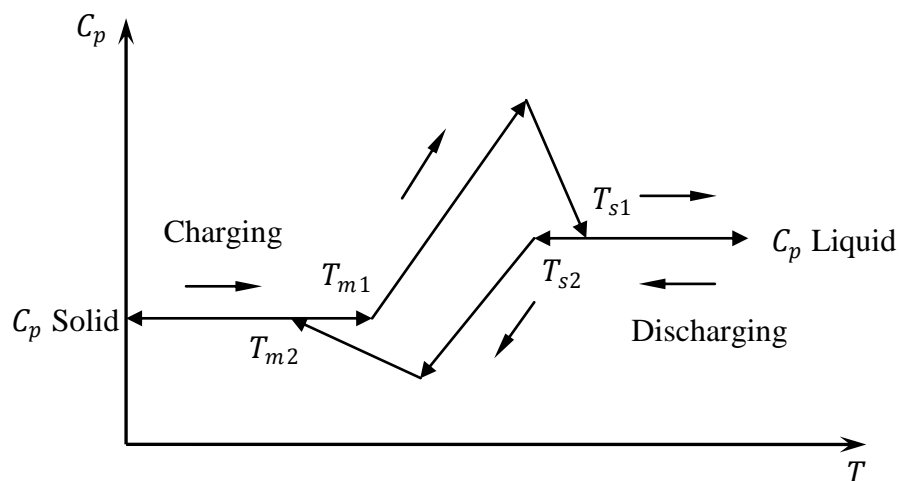
Figure 4-3: Modified effective specific heat during the charging and discharging process, including sub-cooling during discharge.

Two new parameters are required, the first is a flag $flagPCM$, which indicates the phase state; the other is the degree of sub-cooling $Subde$. With these two parameters it is possible to control the amount of energy that transfers as sensible heat (but not latent) because sub-cooling affects the apparent specific heat $C_p(flagPCM, Subde)$. For a given boundary condition (represented by the node temperature), phase change flag and degree of sub-cooling, the algorithm is as follows.

For cooling process at $t + \Delta t$, if $T_{sol} \geq T \geq (T_{sol} - Subde)$

$$Subde1 = T_{sol1} - T_{sol2},$$

$$Subde2 = T_{mel\,1} - T_{mel\,2}$$

Where, the parameter definitions are as given in figure 4-3.

If $\quad T_i^{t+\Delta t} < T_i^t \quad$ Cooling process

Then $C_{p,opp} = C_{p,liq}$ Sensible heat rejected

Figure 4-4 illustrates the algorithm as developed in the present work and implemented within the ESP-r system. Hysteresis appears during cooling as shown in figure 4-3: the melting process arises at a temperature higher than for the solidification process (Bony and Citherlet 2007; Kuznik and Virgone 2009). This results in a delay of the phase change (termed shafting). The difference between the melting and solidification peak temperatures therefore characterise the hysteresis. There are several effects which cause hysteresis, the most common one being sub-cooling, which leads to differences between the heating and cooling process. Another

cause of hysteresis is when the latent heat is released too slowly on cooling, e.g. because the crystallisation rate formation is slow or when the material forms a crystalline structure that is different from the structure at the beginning of the melting phase (Mehling and Cabeza 2008).
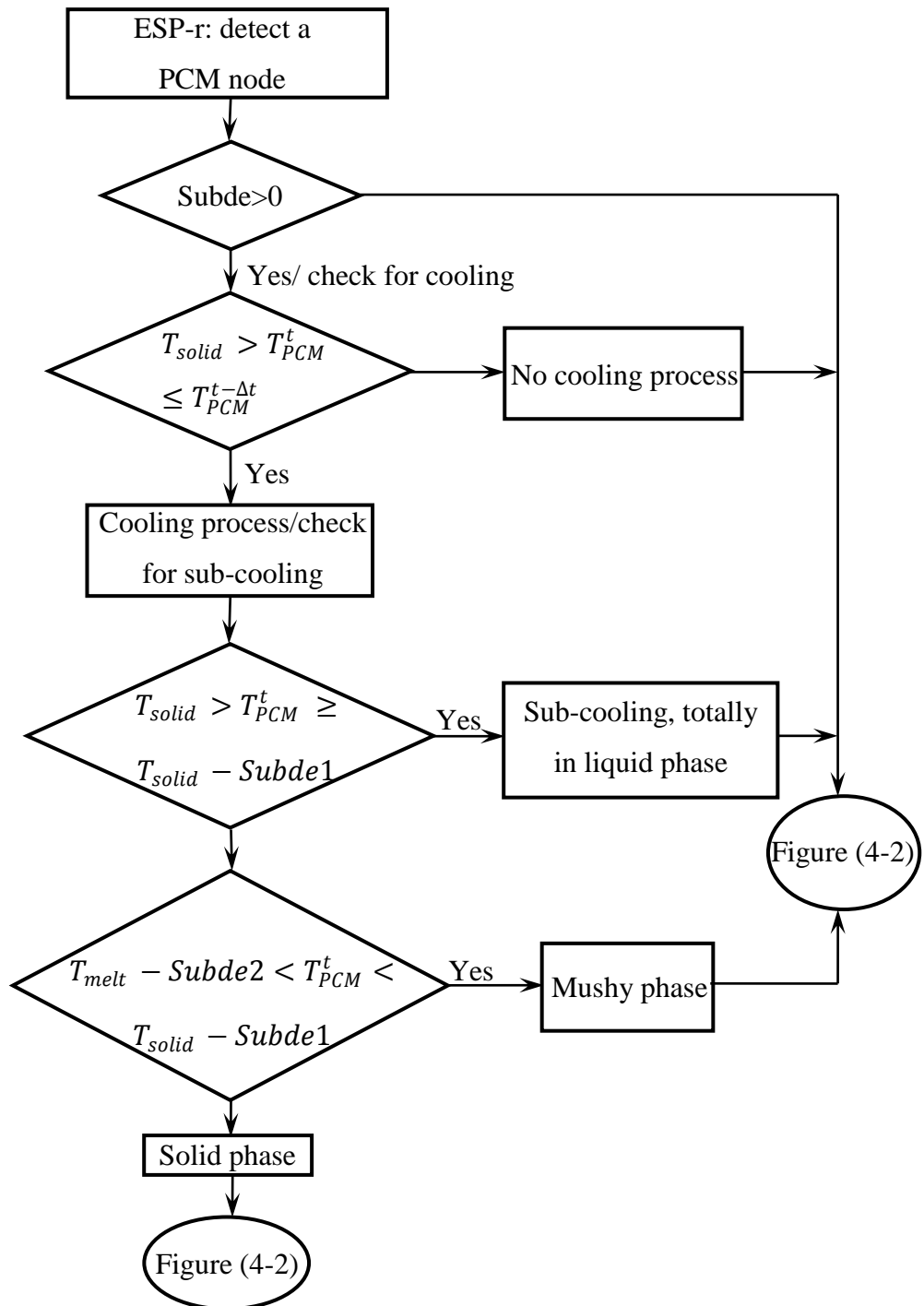
Figure 4-4: Flow chart representing sub-cooling effects when discharging.

4.4 Temperature Effects on PV

Mathematically, the electrical power output generated from the PV cell is given by

$$P = V_{load}\, I_{load}$$

4.11

To solve equation 4.11, data obtained under standard test conditions are used to find the light current, diode current and voltage at different operation values for temperature and light intensity (e.g. short circuit current, open circuit voltage, and the current and voltage at maximum power point, as shown in figure 4-5). The light current depends on the light intensity absorbed and can be described by a linear function, while the voltage can be obtained at maximum power from

$$\frac{dP}{dV} = 0$$

4.12
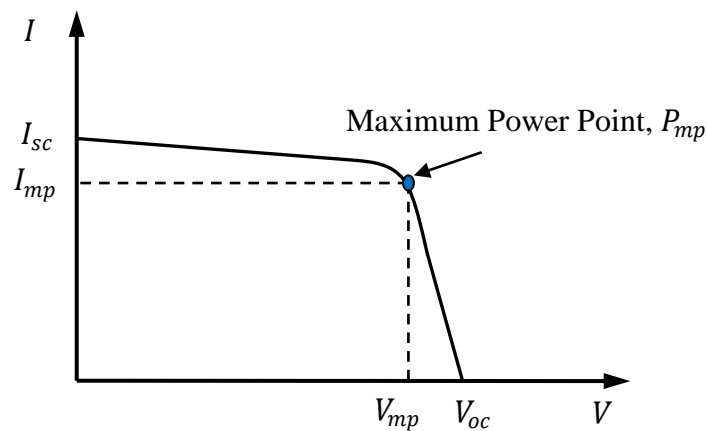
Figure 4-5: Current–voltage characteristic of a silicon solar cell.

With high irradiance, the PV module temperature is usually above the ambient temperature, even at low ambient temperature. The electrical power P_{mp}, of a PV module decreases linearly with the module temperature, the proportional decrease being calculated from the total of the voltage and current coefficients (Eicker 2003):

$$\frac{\alpha_{P_{mp}}}{P_{mp}} = \frac{\frac{d(VI)}{dT}mp}{P_{mp}} = \frac{\frac{dV}{dT}I_{mp} + \frac{dI}{dT}V_{mp}}{V_{mp}\,I_{mp}} = \frac{\beta_{mp}}{V_{mp}} + \frac{\alpha_{I_{mp}}}{I_{mp}} \qquad 4.13$$

With average power loss coefficients of 0.3–0.4% per Kelvin, at usual module temperatures of 50°C a performance decrease of as much as 7.5–10% may be expected. To predict a PV module's I-V characteristic for temperatures where data are not available, temperature coefficients are necessary. Temperature coefficients demonstrate the change in module performance with respect to module temperature. King *et al* (1998) determined that 4 temperature coefficients are necessary to accurately model the effect of temperature on a module's I-V characteristic.

$$I_{sc}(T) = I_{sc}(T_{ref}) \cdot \left[1 - \alpha_{I_{sc}} \cdot (T_{ref} - T_{PV})\right] \qquad 4.14$$

$$V_{oc}(T) = V_{oc}(T_{ref}) + \beta_{V_{oc}} \cdot (T_{ref} - T_{PV}) \qquad 4.15$$

$$I_{mp}(T) = I_{mp}(T_{ref}) \cdot \left[1 - \alpha_{I_{mp}} \cdot (T_{ref} - T_{PV})\right] \qquad 4.16$$

$$V_{mp}(T) = V_{mp}(T_{ref}) + \beta_{V_{mp}} \cdot (T_{ref} - T_{PV}) \qquad 4.17$$

Equations 4.14 through 4.17 can be used with coefficients from table 4-1 to determine module parameters I_{mp}, I_{sc}, V_{mp} and V_{oc} at operation cell temperature T_i given parameters at a cell temperature T_{ref}. The values $\beta_{V_{oc}}$ and $\beta_{V_{mp}}$ in equation 4.14 and equation 4.17 are the array or module values expected at standard test condition. These values are usually located on a module label by the suppler. For arrays, the module values must be multiplied by the number of modules in series.

Table 4-1: Typical temperature coefficients for commercial modules at standard test condition (King *et al* 1997)

Module type	$\dfrac{dI_{sc}}{dT}$ $\alpha_{I_{sc}}$ (1/°C)	$\dfrac{dI_{mp}}{dT}$ $\alpha_{I_{mp}}$ (1/°C)	$\dfrac{dV_{sc}}{dT}$ $\beta_{V_{sc}}$ (1/°C)	$\dfrac{dV_{mp}}{dT}$ $\beta_{V_{mp}}$ (1/°C)
ASE300, mc-Si	0.00091	0.00037	-0.0036	-0.0047
AP8225, Si-Film	0.00084	0.00026	-0.0046	-0.0057
M55, c-Si	0.00032	-0.00031	-0.0041	-0.0053
SP75, c-Si	0.00022	-0.00057	-0.0039	-0.0049
MSX64, mc-Si	0.00063	0.00013	-0.0042	-0.0052
SQ-90, c-Si	0.00016	-0.00052	-0.0038	-0.0048
MST56, a-Si	0.00099	0.0023	-0.0041	-0.0039
UPM88, a-Si	0.00082	0.0018	-0.0038	-0.0037
US32, a-Si	0.00076	0.0010	-0.0043	-0.0040
SCI50, CdTe	0.00019	-0.0012	-0.0037	-0.0044

4.5 PV/PCM Analysis

The use of PCMs for electronic systems has increased due to the passive nature of the technique. The use of passive cooling has the advantage of low maintenance and high reliability because there are no moving parts. The PV module surfaces are exposed to solar loads as well as thermal loads from the solar cells they contain. In some instances, passive cooling techniques are unable to provide the required cooling at times of peak solar radiation. A possible solution is the use of a

PCM heat exchanger as shown in figure 4-6a. In a PV cell, the cell reaches its steady state temperature when the solar power absorbed is equivalent to the electrical power delivered to the load, plus the dissipated power in the form of heat to the air gap.
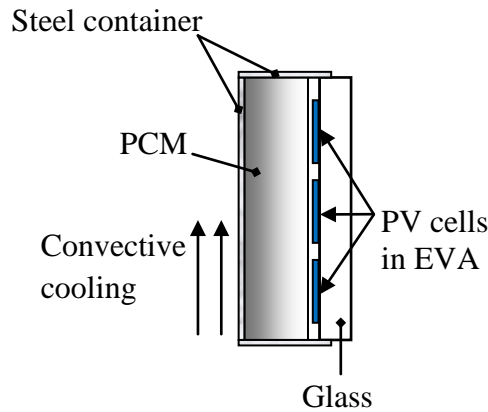
Figure 4-6a: A PV/PCM building-integrated facade.
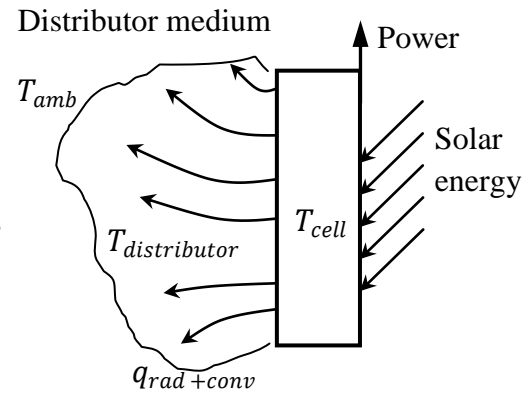
Figure 4-6b: Heat distribution through the PV layer.

The final temperature depends on the dominant method of dissipation and on the relevant power. From figure 4-6b, it can be seen that the conduction process cannot act as a heat sink but merely as a way of transporting heat towards the surfaces where, through convection and radiation, heat is released into the air gap. The PCM effectively acts as a constant temperature heat sink for the electronic cells (source of heat) within the PV modules. In general, PV/PCM components are constructed of several elements:

1. PV cover (e.g. glass);
2. PV material (semiconductor), conductors layer (considered as homogenous);
3. resin (EVA) layer;
4. PCM layer; and
5. metallic casing.

ESP-r deals with multi-layered building constructions; the PV component is associated with one or more construction, with one of the material nodes producing electrical energy from the absorbed solar radiation. Consider the façade-integrated PV/PCM component shown in figure 4-6. The solar radiation magnitude is reduced to reflect the fact that not all the absorbed solar radiation is converted to heat because a proportion is converted to electrical energy at the PV node. The PV cell temperature T_i, is given by equation 3.4 for an internal homogenous node i. If an opaque PV layer is used, all solar energy is absorbed in the first PV mixed layer, i.e. node $i+1$. The electrical power produced is $\frac{\Delta t \, q_{e,i+1}^{t}}{\Delta V_{i+1}}$ in the $i+1$ node per unit volume. This fraction will not convert to heat but will decrease the cell temperature compared with the case of no electrical output (Kelly 1998). The heat energy input to each control volume at the future and present time rows are as follows.

Future time: $\frac{\Delta t q_{i+1}^{t+\Delta t} - \Delta t q_{e,i+1}^{t+\Delta t}}{\Delta V_{i+1}}$

Present time: $\frac{\Delta t q_{i+1}^{t} - \Delta t q_{e,i+1}^{t}}{\Delta V_{i+1}}$

The ESP-r space discretisation approach for special materials as used for PV representation can also be used to represent PCMs. By means of the finite difference discretisation scheme described in Chapter 3, the system of governing differential equations is transformed to an algebraic finite difference form. PCM can be represented by a homogenous middle node and two mixed material nodes at the material boundaries as shown in figure 4-7. In order to integrate the variable thermo-physical properties of PCMs, equation 4.1 is rewritten with variable thermo-physical properties as in equation 3.22. For the phase change layer, high non-linearity in the

thermal properties with temperature requires that the storage and transfer properties

be estimated at each time step. The effect appears in the self-coupling coefficient $C_{s,i}^t$

and the cross-coupling coefficient $C_{c,i}^t$ at time t, as shown in equation 3.13 (Clarke

2001). Within the simulation, the PCM layer is divided into three sub-layers each

represented by anode, one in the middle with total thickness $\frac{\Delta x}{2}$ and one at each

surface with thicknesses $\frac{\Delta x}{4}$.
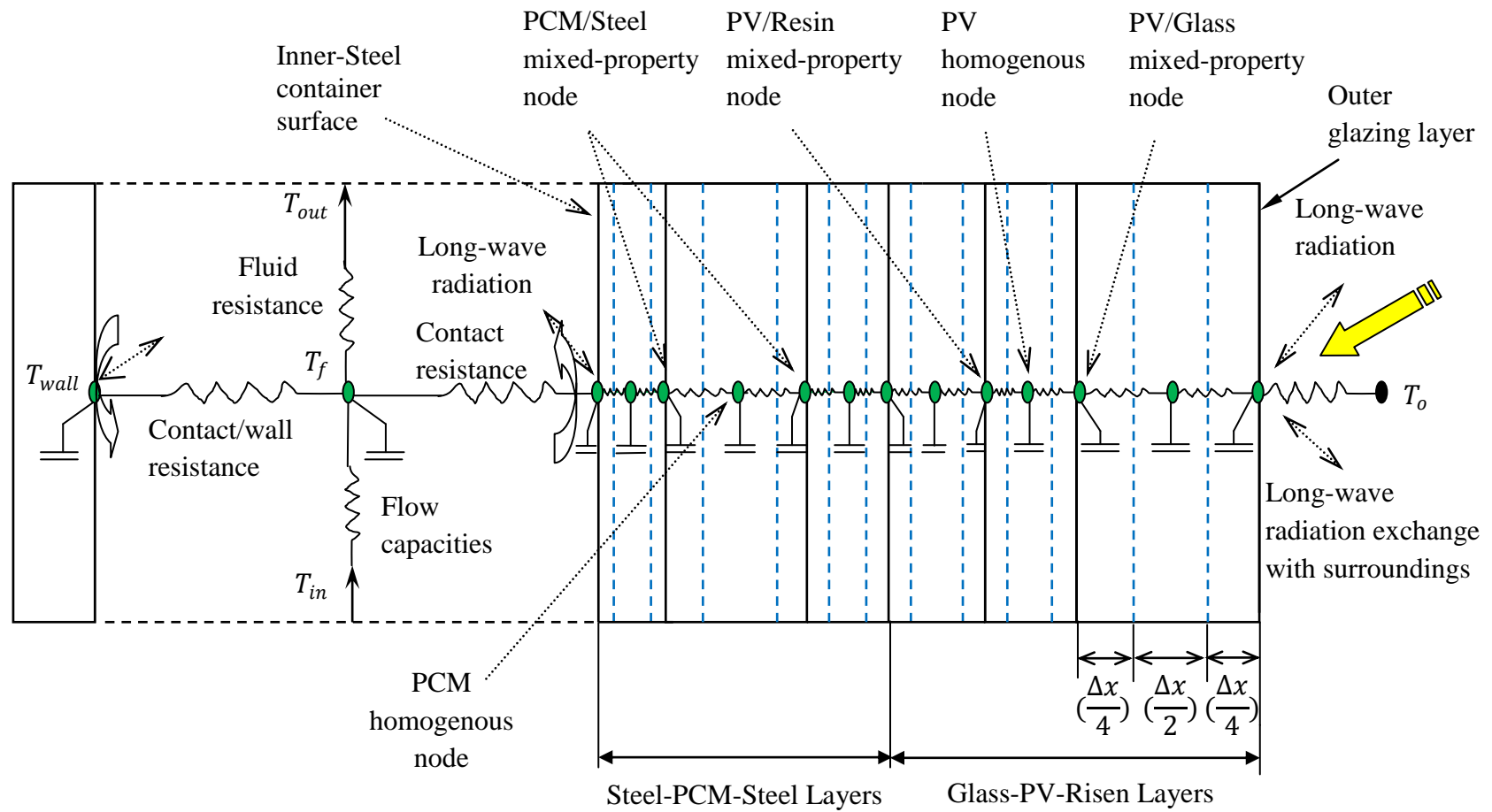
Figure 4-7: ESP-r space discretisation approach for a building façade with integrated PV/PCM components.

Initially, PCM node temperatures are represented in the zone thermal matrix within the whole system matrix equation. A simulation controller compares the PCM layer node temperatures with upper and lower phase change temperature limits. If the node temperature is below the melting temperature, the final state is solid and the thermal properties will correspond to the first condition in equation 4.3. If the PCM node temperature is greater than the solidification temperature, the final state is liquid and the thermal properties will correspond to the third condition. If the PCM node temperature is lower than the phase change limit, then the second condition applies. The impact of PCM is modelled by updating the appropriate self-coupling and cross-coupling coefficients to reflect the thermal property changes, and inserting these in the zone matrix at the next simulation time step. Finally, the heat storage within each node is calculated using equation 3.12**.**

4.6 ESP-r Reduction Time Step for PCM Simulation

Because of the non-linear nature of the phase change problem, most solutions involve the use of numerical methods or approximate analytical techniques. In ESP-r, a numerical solution is implemented within which PCM thermo-physical properties are considered as a function of the nodal temperatures at the previous time step. Where the PCM properties are highly non-linear, iteration is employed so that the properties will, eventually, relate to the temperatures prevailing at the future time row. Figure 4-8 depicts a sequence in which the general energy equation coefficients (equation 3.13) are generated when PCM behaviour is involved in the calculations; it ensures that at time step t_0 the PCM and PV temperatures are calculated; then, at the next time step t_1 they are recalculated. However, when the PCM node temperature at time step t_1 is within the phase change temperature, the thermo-physical properties

are recalculated to quantify the phase type (liquid, solid, or mixture). Therefore, the general energy equation coefficients at this time step are modified by the new thermo-physical properties. Thereafter, the temperatures at the PV and PCM nodes are recalculated at the new step t_2. This set-up is implemented at each building time step as shown in Appendix (B).
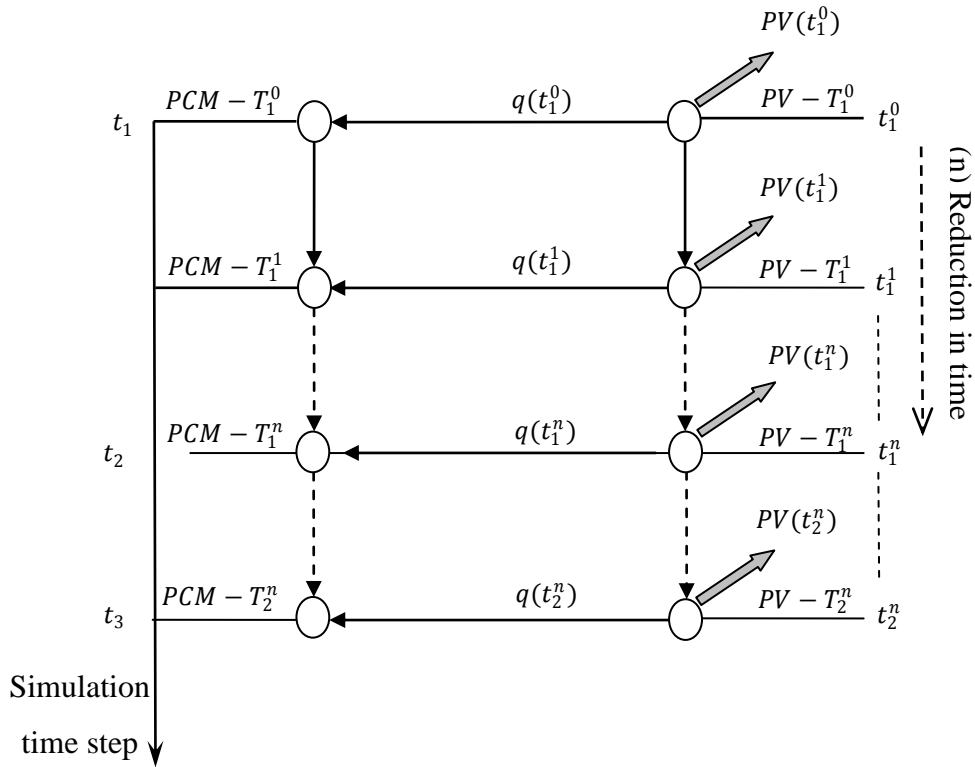
Figure 4-8: Reduction time step to support PV/ PCM modelling.

The previous procedure gives a delay to reflect the effect of phase change on the PV temperature control. This delay depends on the simulation time step used, as is shown in section 4.10.1, and how the simulation process treats the PV/PCM interaction at each time step. For a specific time step, if the phase change takes place, effective integration is achieved when the PCM layer starts absorbing the accumulated heat at the PV layer and re-calculates the new temperature distribution

at the same time step. This technique is achieved by using a control loop to sense the PCM temperature at the time step, e.g. t_1^1, and comparing it with the phase change range in order to decide the appropriate PCM phase; the thermal properties (ρ, C_p and k) are then updated and the heat storage value calculated. Before the simulation continues to the next time step, the heat transfer equation is re-solved to find the new temperature distribution based on the updated PCM thermal properties and heat storage. These new temperatures are used for the existing time step t_1^1, to re-calculate the PV power output for use as an initial condition at the next time step t_1^2. The control loop is reactivated again to re-adjust the PCM thermal properties and the procedure above is repeated until convergence is achieved.

4.7 PV/PCM with PCM Optical Properties Control

In addition to high latent heat property, the optical properties of liquid-solid type PCM vary in response to temperature. Transparent or semi-transparent PV panels can be integrated with PCMs; figure 4-9 shows a PCM inserted into the gap between the PV layer and glass to create a PCM container with high energy density. Part of the incident solar radiation is immediately converted into electricity and transmitted away, while the other part is absorbed in the PV layer. If the PV temperature is below the PCM melting temperature, the solid PCM layer (crystallisation state) diffuses a large part of the solar radiation. If the PCM temperature reaches the melting point, phase change starts to produce a liquid fraction in the PCM layer. The optical property can be considered as a function of the PCM liquid fraction, where the change in liquid fraction is a function of time with and without the effects of radiation for three sets of conditions, (results for other thermo-physical properties behave in a similar fashion):
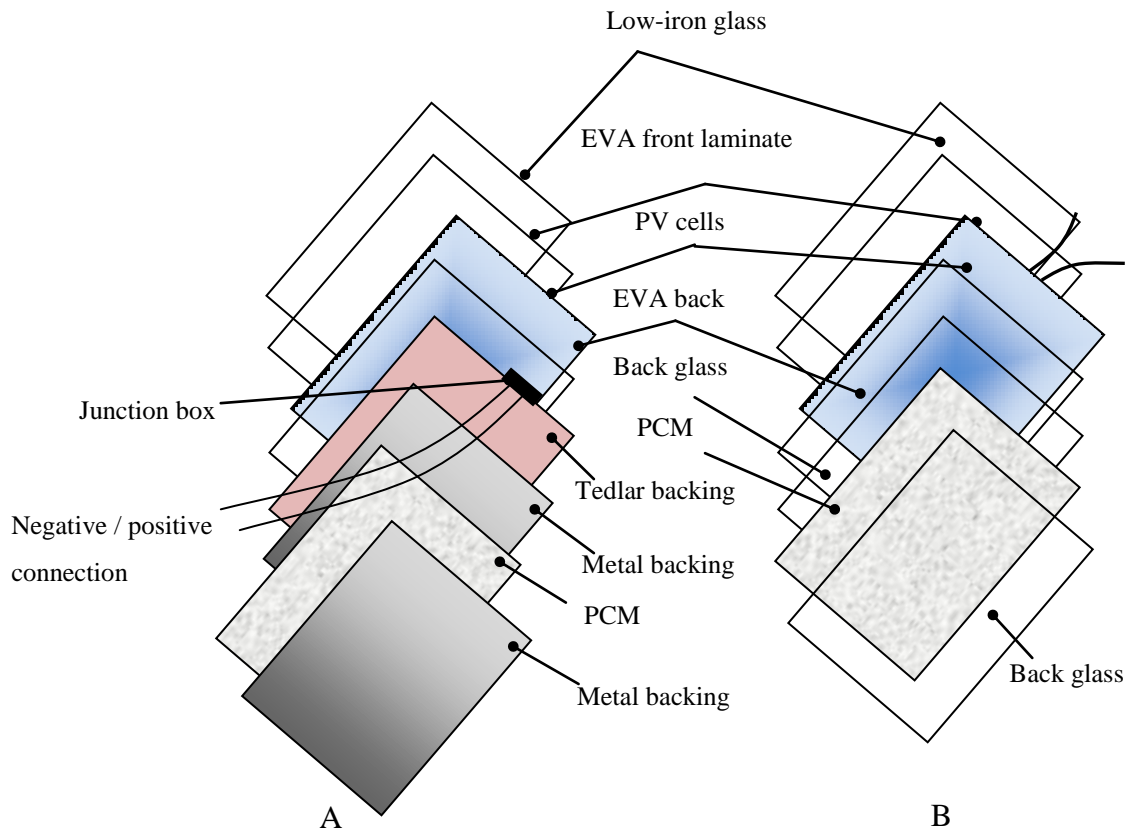
Figure 4-9: Typical assembly (as seen from the back) of a crystalline silicon PV module made: a) opaque by the Tedlar-Metal-PCM-Metal backing and b) semi-transparent by the Glass-PCM-Glass backing.

$$f_l \leq 0 \text{ , Opaque (totally solid)}$$

$$1 > f_l > 0 \text{ , Mixing (semi-transparent)}$$

$$f_l \geq 1 \text{ , Liquid (transparent or semi-transparent)}$$

As will be discuss in chapter 5, the optical properties are controlled so that the liquid fraction is utilised in the material's selection. If the liquid fraction is zero then the PCM is solid; when it is less than one, the PCM is in the mixed mode; when it is equal to one it is liquid. This liquid fraction is directly related to how much solar radiation is being admitted into a surface; this will affect the temperatures at the PCM and PV nodes, which in turn influence the PV's efficiency. The external glass-

PV receives the solar radiation: part of it is absorbed, part reflected and the rest is transmitted to the PCM region (initially in the solid phase), which absorbs part of the energy and reflects the rest (the internal temperature remains unchanged). At the interface between the internal PV and the PCM, the radiation absorbed by the PCM and the heat conducted by the PV-glass surface raises the PCM temperature, converting a layer of the PCM to liquid. This process continues until all the PCM changes into liquid and, consequently, the internal air duct temperature starts to change. A well-designed component will ensure that the external temperature will start to decline before total melting of the enclosed PCM occurs. Several researchers have examined the possibility of controlling the natural light in a building using thermotropic glass, which encapsulates a polymer gel as a PCM (Watanabe 1998; Takashi 2003; Nitz and Hartwig 2005; Takashi *et al* 2008). Here, the PCM undergoes phase transition at a characteristic temperature: the lower temperature or solid phase form is transparent, while the higher temperature gel form is cloudy. The liquid fraction will dictate the optical properties that result:

$$f_l \leq 0 \qquad \text{Opaque (totally transparent)}$$

$$1 > f_l > 0 \quad \text{Mixed (semi-transparent)}$$

$$f_l \geq 1 \qquad \text{Liquid (cloudy or semi-opaque)}$$

Figure 4-10 illustrated the algorithm for optical variation as implemented within the ESP-r system during the present project.
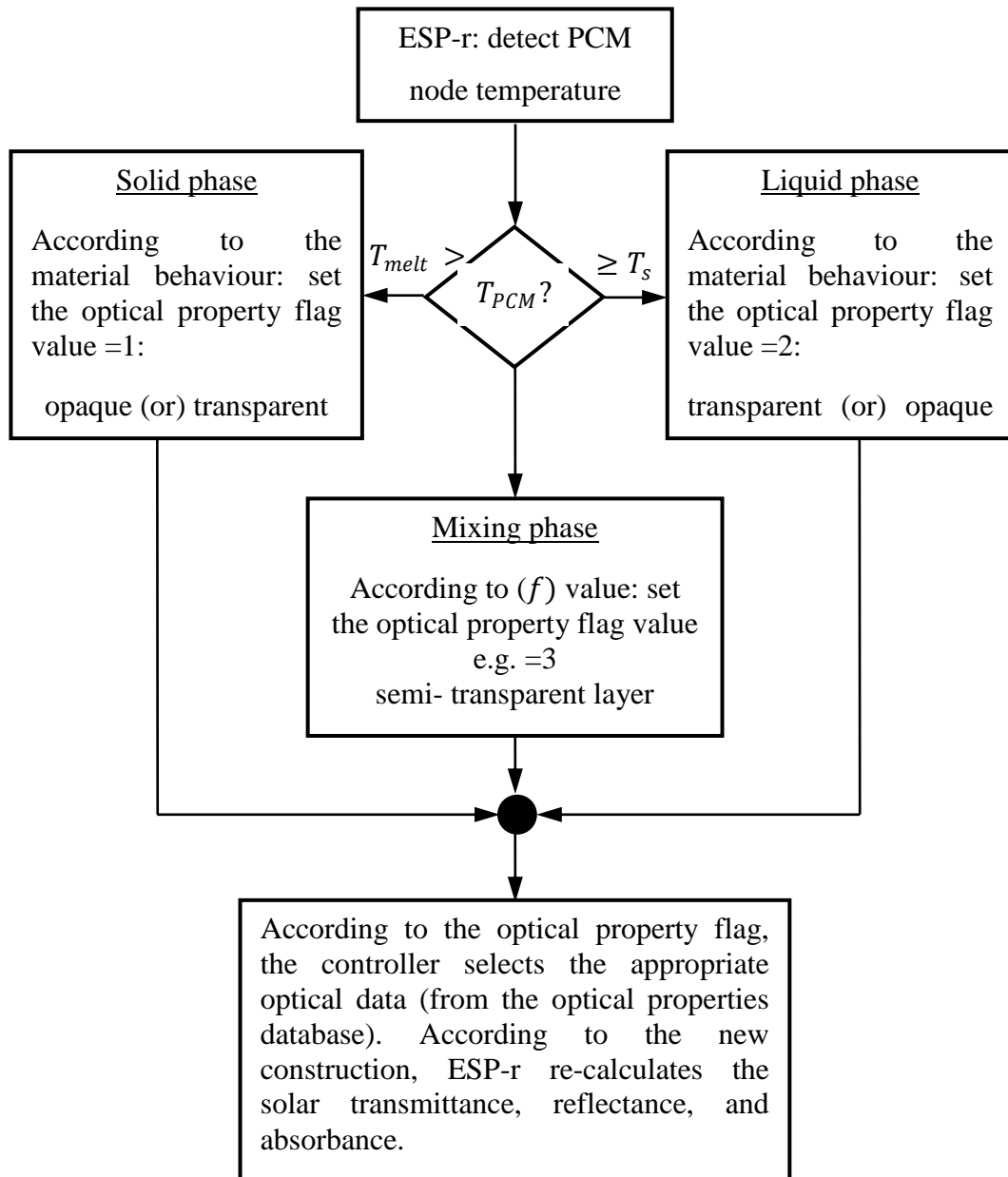
Figure 4-10: Flow chart represents the PCM optical variation with phase change.

4.8 PCM layer Treatment

The analysis of heat transfer problems in phase change processes is complex because the solid–liquid boundary movement depends on the speed at which the latent heat is absorbed or lost at the boundary. The phase-transition region where solid and liquid coexists is called the interface. Its thickness may vary and its

microstructure can become complicated, depending on several factors such as the material itself, the rate of cooling, the temperature gradient in the liquid, surface tension, *etc*. Most pure materials solidify at a fixed melting temperature where the interface appears locally planar and of negligible thickness as shown in figure 4-11(a). Referring to figure 4-11(b), when the phase change extends over a temperature range, the phase transition region may have apparent thickness and is referred to as a mushy zone.
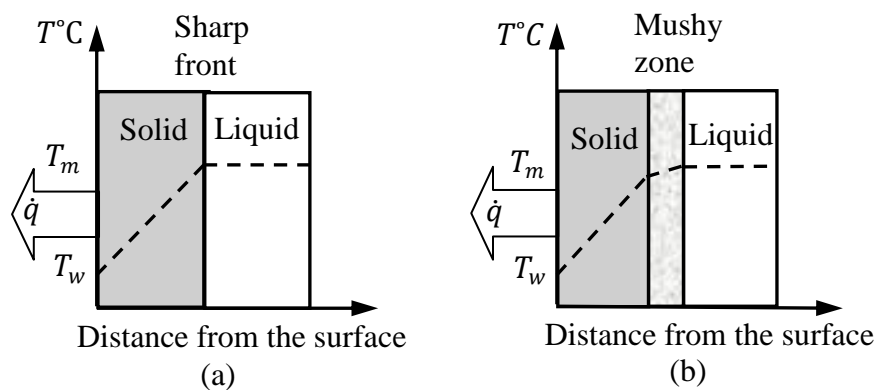
Figure 4-11: Melting front-sharp front and mushy zone front.

For PCM phase change to occur, the following general stages for the melting process are undergone.

a. Heat is supplied at the start-up charging period increasing the temperature of the solid PCM where pure conduction heat transfer occurs.
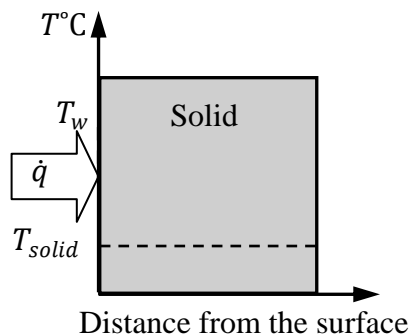
Figure 4-12a: Sensible heat added to solid.

Figure 4-12a shows the heating of a PCM layer with finite thickness initially at $T_{sol} < T_m$. The temperature of the heat transfer surface at the left side suddenly increases to $T_w > T_m$.

b. Heat purely transferred by conduction from the heated wall to the PCM. The moment the melting process occurs the solid–liquid interface commences (figure 4-12b).
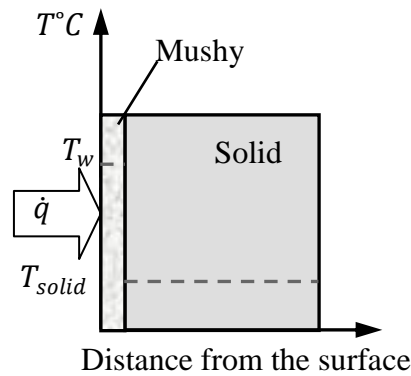
Figure 4-12b: Mushy region develops and melting starts within the adjacent solid.

c. The transition from conduction to natural convection commences as the thickness of the melted layer increases and the interface starts to move. At the interface, there exists equilibrium, which can resemble solid particles surrounded by liquid as shown in figure 4-12c.
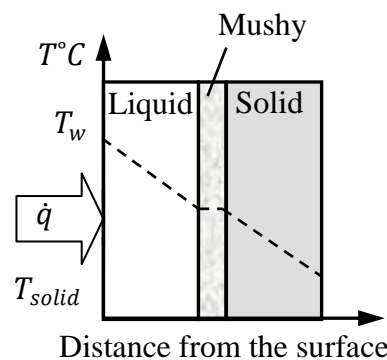
Figure 4-12c: Mushy region moves into solid and melt layer increases.

d. The convection regime dominates when most of the solid is melted (figure 4-12d).
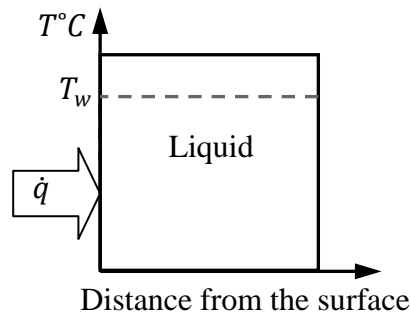
Figure 4-12d: Mushy region disappears and all solid melts.

e. If the phase front proceeds into the layer from both sides then the two phase fronts will meet and heating is finished (figure 4-14e).
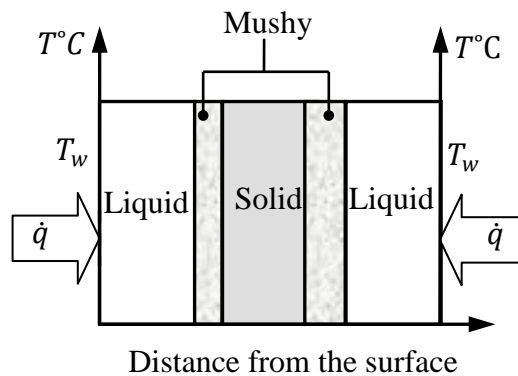
Figure 4-12e: Phase front proceeds into the layer from both sides.

During phase change, the solid–liquid interface moves away from the heat transfer surface. Thus, the surface heat flux decreases due to the increasing thermal resistance of the growing layer of melted PCM. Thermal resistance increase takes place more often in the solidification process where the main heat transfer mode is conduction. What happens is that the PCM solidifies at the heat transfer surface and behaves as a self-insulator due to the low heat conductivity. The PCM melts more quickly than it solidifies because natural convection speeds up the melting. If there is

an efficient temperature gradient in the liquid PCM layer, natural convection exists in the liquid–solid interface.

4.9 Mushy Region Tracking Scheme

As stated in Chapter 3 a finite difference discretisation is applied to multi-layered constructions, with each layer represented by two surface nodes and one central node. The same procedure applies to the surface that contains a layer with phase change behaviour. Each node surrounded by a control volume represents a virtual layer with arbitrary thickness δ, as shown in figure 4-13.
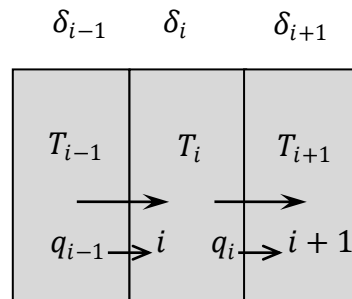
Figure 4-13: Nodal discretisation for a PCM layer within a construction.

Each virtual layer is characterised by a temperature change that determines the status of the material phase and the temperature distribution in the PCM layer. Here i represents the node under consideration, while $i+1$ and $i-1$ represent the neighbouring nodes in the positive and negative x-direction respectively (the direction of heat flow). The rate of change of the control volume's temperature determines whether the material initial state is solid, liquid or mushy. Table 4-2 shows phase change tracking through virtual layers under arbitrary heat flux direction at different time steps.

Table 4-2: PCM layer divided arbitrary into 3 virtual layers, tracking the mushy region at each time step according to the arbitrary flux direction.

Flux direction	$i-1$	i	$i+1$	$t=$
Charging	S	S	S	1
Charging	M	S	S	2
Charging	L	M	S	3
Charging	L	L	M	4
Discharging	L	M	S	5
.	.	.	.	.
.	.	.	.	.

When PCM node i at time step t=1 is in a solid state, the heat applied can be used to raise the node's temperature up to the melting point. If extra heat is still available then it is used to melt the PCM and therefore increase its liquid fraction f_i. In order to calculate the temperature and the liquid fraction of node i, the PCM node temperature T_i, is compared with the melting temperature T_m. If T_i is less than T_m then the heat will only be able to raise the temperature of the node to below T_m and therefore the node will still be in the solid state, i.e. $f_i = 0$, and the effective thermo-physical properties will equal their original values when in the solid phase. However, if T_i is equal to T_m then the absorbed heat flux raises the node temperature to the melting temperature T_m, but no heat is available to start the melting of node i; in other words, the liquid fraction $f_i = 0$ and again the PCM thermo-physical properties equal their original values in the solid phase. If T_i is greater than T_m then a portion of the heat flux absorbed is used to raise the node

temperature to T_m and the remaining portion is used to melt the node (to increase its liquid fraction from zero, i.e. $0 < f_i < 1$); the node is in its mushy phase. The thermo-physical properties are adjusted to new values representative of the mushy phase (according to equation 4.1 and figure 4.2). If node i is in the mushy state then, when heat is applied to the node, the node liquid fraction f_i, increases and its temperature either remains constant or rises above T_m depending on T_i. If T_i is less than T_s then the node stays in the mushy zone but its liquid fraction increases (again the effective thermo-physical properties are calculated according to equation 4.1 and figure 4.2). If T_i is equal to the solidification temperature T_s, then the node is about to leave the mushy state but remains at the melting point and $f_i = 1$ and effective thermo-physical properties for the liquid phase are determined according to equation 4.1. If T_i is greater than T_s then the node temperature rises above the melting point. Part of the heat brings f_i to unity, whilst the remaining portion of the heat flux raises the node temperature. If the node is in the liquid state then the heat applied is used to increase its temperature further. Effective thermo-physical properties are calculated as illustrated in figure 4.2 and according to equation 4.1, taking into consideration the effect of natural convection if this is indicated by testing the liquid thickness using equation 4.8 and updating the thermal conductivity according to equation 4.9. The procedure above is repeated for the other virtual layers ($i - 1$ and $i + 1$) and the total heat stored/extracted from the PCM layer calculated according to equation 3.21.

4.10 PCM layer Modelling

Using an enclosure with a higher aspect ratio produces a flatter phase front compared to that of a lower aspect ratio. A PCM layer of high aspect ratio and less thickness decreases the convection heat transfer effect since decreasing the PCM

thickness reduces the Rayleigh Number and hence reduces the convection heat transfer coefficient and contributes significantly to suppression of the convection heat transfer effect (Tan and Leong 1994; Ho and Chang 1994; Agyenim *et al* 2010). Fortunately, in the present application, the use of PCM can be characterised by a high aspect ratio (a small dimension in the x-direction compared with the dimensions in the other directions, i.e. $x \ll y \& z$).   In addition to small PCM thickness, the PCM's low thermal conductivity represents the main controlling parameter for the heat transfer rendering a 1D treatment of conduction possible. At the end of the melting phase, if natural convection in the PCM liquid layer is the dominant mode (according to equation 4.8) then the convection effect is represented via the use of an enhanced thermal conductivity for the liquid layer, i.e. $k_{effc}(h_{liq})$ (equation 4.6). The influence of the PCM depends on the phase change existence where mushy region tracking is possible.   Both the size of the PCM domain and the surface temperature strongly influence the temperature distribution and the phase change location (Savovic and Caldwell 2003).

For this reason, two approaches were examined as follows.

1) The effect of reducing the simulation time step.

2) The effect of increasing the number of virtual layers.

To assess the above approaches an integrated model encapsulating a PV/PCM component was established and simulated. A description of this 4 zone model is given in appendix (D) and figure D-1. The duct zone includes a PV/PCM component with a PCM layer of 10 mm thickness and thermo-physical properties as listed in table D-1. For an insolation level of 750 Wm^{-2} and ambient temperature of 24°C, the

PV cell temperature rises to over 45˚C. The phase change temperature range was selected as 25-30˚C and different simulations were under taken under the same weather conditions.

4.10.1 Impact of time step

The simulation time step was varied from 1 hour to 1 minute while the PCM layer of thickness l was arbitrarily divided into 3 virtual layers each of thickness δ. Figure 4-14 shows the discretisation scheme.
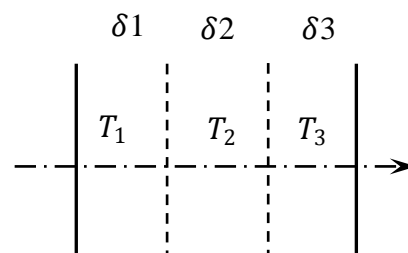
Figure 4-14: PCM layer schematic - each virtual layer is divided into 3 virtual layers each represented by three nodes.

In figure 4-15, the nodal temperature change is arrived at by using the effective heat capacity of equation 4.3. The new temperature for time step $j + 1$ at node i is calculated using the heat capacity at time j. If the simulation time step, Δt, is too large (e.g. t=1hr as in figure 4-15(a)) then large temperature differences will occur as shown in figure 4-16(a). Such differences increase the discontinuity in the node temperature in the time domain. Thus, this node temperature will be out of the phase change limit and a large amount of sensible heat will be transferred from the boundaries to impact on the node temperature as illustrated in section 4.9. With reference to figure 4-15(a), all node temperatures increase sensibly above the lower phase change limit to the upper limit without any clear occurrence of phase change. The same behaviour also applies to the case of cooling. When the time step is

reduced significantly (i.e. Δt=1min as in figure 4-15(b)), the in existence of a mushy region was solved and the performance improves significantly. (Note the small difference generated between present and previous node temperatures as shown in figure 4.16(b)). The smooth transition of the node temperature variation increases the possibility of the temperature being located within the phase change limits. From figure 4-15(b), the effect can be seen clearly in the second and third nodes where the phase change occurs and the temperature varies slowly as discussed in section 4.9.
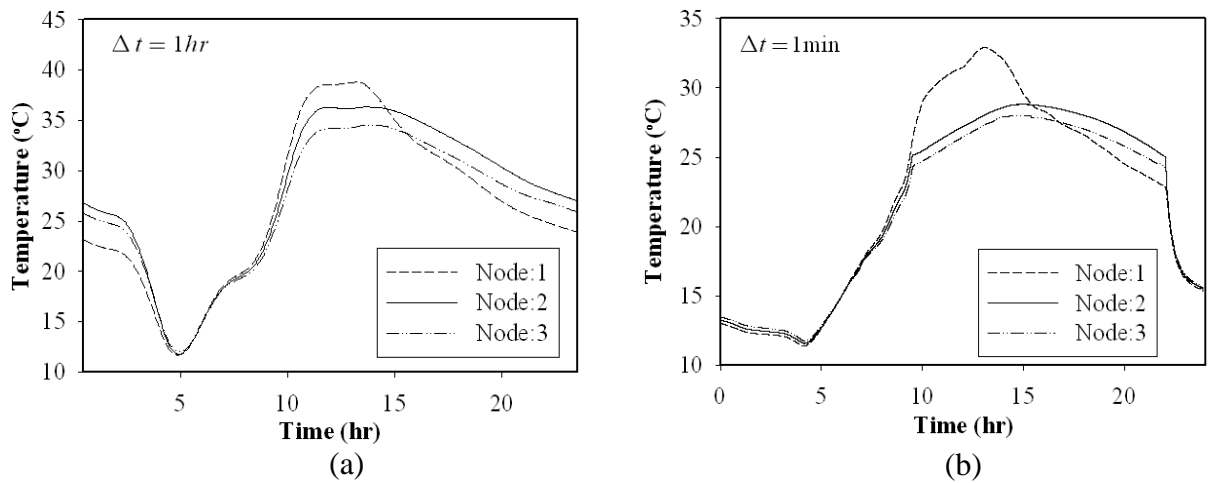
Figure 4-15: Results represents the modelling of a PCM layer using two values for the time step.
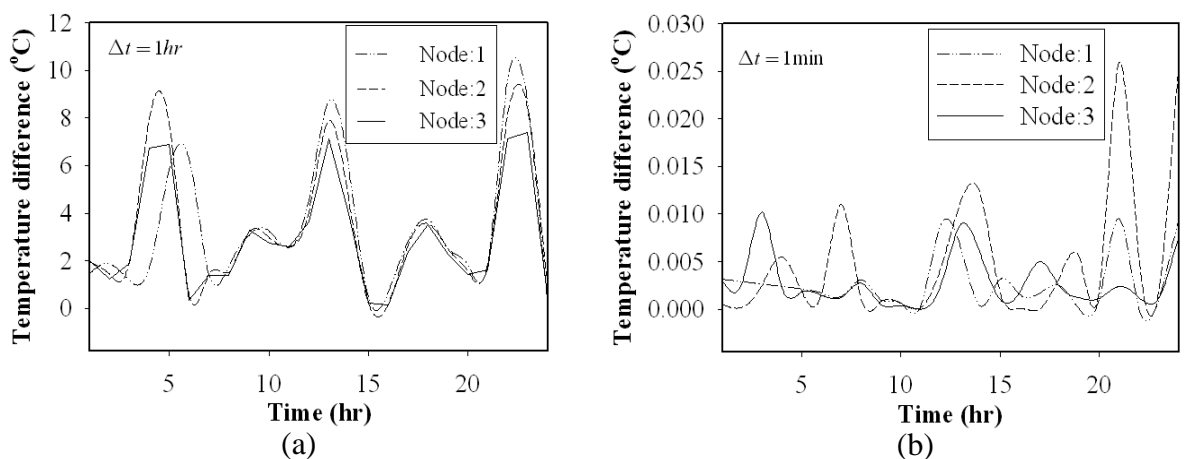
Figure 4-16: The distribution of the differences in the node temperatures at the present and previous time steps ($\Delta T = T_{i,j} - T_{i,j-1}$) for two simulation time steps.

It can be concluded that the simulation of a rapidly changing heat capacity is required; therefore, the use of a small time step in the simulation will yield more accurate results.

4.10.2 Impact of PCM layer discretisation

In this case, the effect of changing the spatial resolution of the temperature distribution in the PCM layer is introduced. The 10 mm PCM layer is divided into 2 then 3 layers of equal thickness. In each configuration, the simulation is repeated using two time steps (Δt=1hr and Δt=1min).

A- Two layers: In this configuration, the PCM layer is divided into 2 layers with each layer further divided into 3 virtual layers as shown in figure 4-17 (as in the case when the time step was changed).
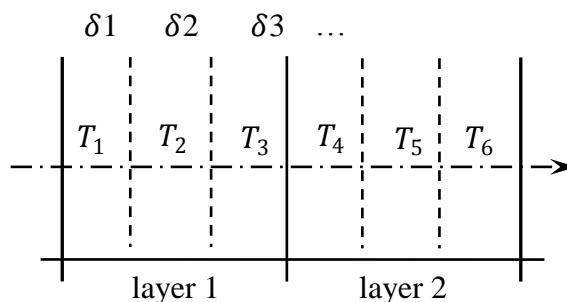
Figure 4-17: PCM layer comprising 2 sub-layer nodes.

Figure 4-18 (a & b) show the temperature distribution through each virtual layer. With a large time step, the temperature distribution gives nearly the same behaviour as found when the PCM consisted of one layer only. The temperature starts increasing rapidly and ignores the existence of the PCM completely. As a result, increasing the PCM space discretisation gives an improvement in the temperature distribution but still generates large temperature swings for each node at

the previous and present time steps within a simulation. In figure 4-18(c & d) the results show agreement with the results found from the configuration with one layer under a small time step.

(a)

(b)

(c)

(d)
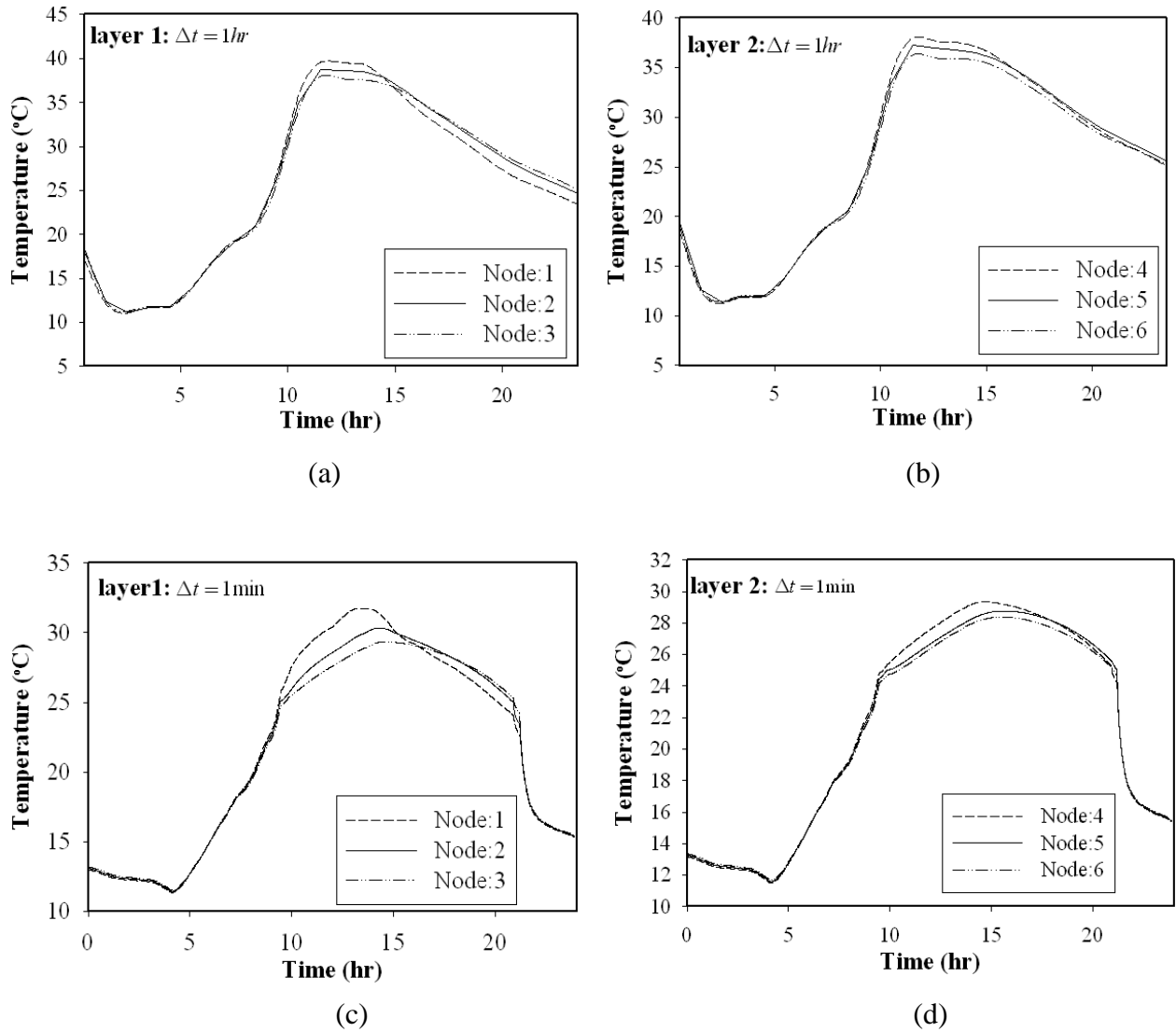
Figure 4-18: Results for a PCM layer divided into 2 layers simulated using two time steps:

1- $\Delta t = 1$ hr (a & b).

2- $\Delta t = 1$ min (c & d).

The temperature distribution follows the discussion in section 4.9: the first node absorbs a large part of the heat and its temperature rises, reaches the upper phase change limit and increases the liquid fraction very fast transforming all PCM to the liquid phase and extending the mushy region to the other nodes. Increasing the PCM volume discretisation and using a small simulation time step improves the temperature distribution and increases the accuracy of the mushy region tracking (when compared with the case of one layer).

B- Divided into three layers: in this configuration the PCM layer is divided into 3 layers with each layer divided into 3 virtual layers (as shown in figure 4-19) as in the case when the time step was changed.
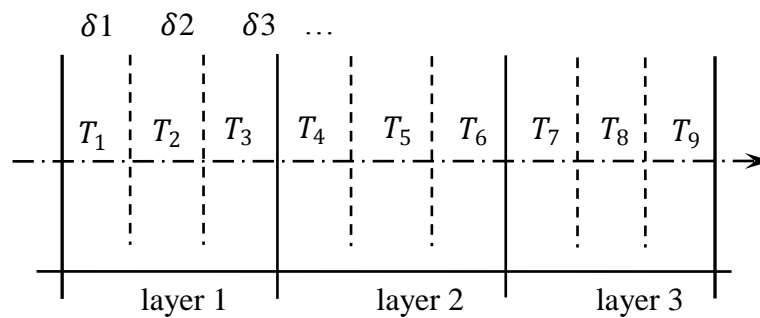
Figure 4-19: PCM layer comprising 3 sub-layer nodes.

Figure 4-20 (a to c) shows the temperature distribution through each virtual layer. Again, the simulation takes place for two time steps. With a large time step, as in the case where the PCM was divided into 2 layers, the same scenario is repeated: the temperature distribution gives nearly the same behaviour as found when the PCM consisted of two layers. In all layers, the temperature increases rapidly and disregards the existence of the PCM completely.
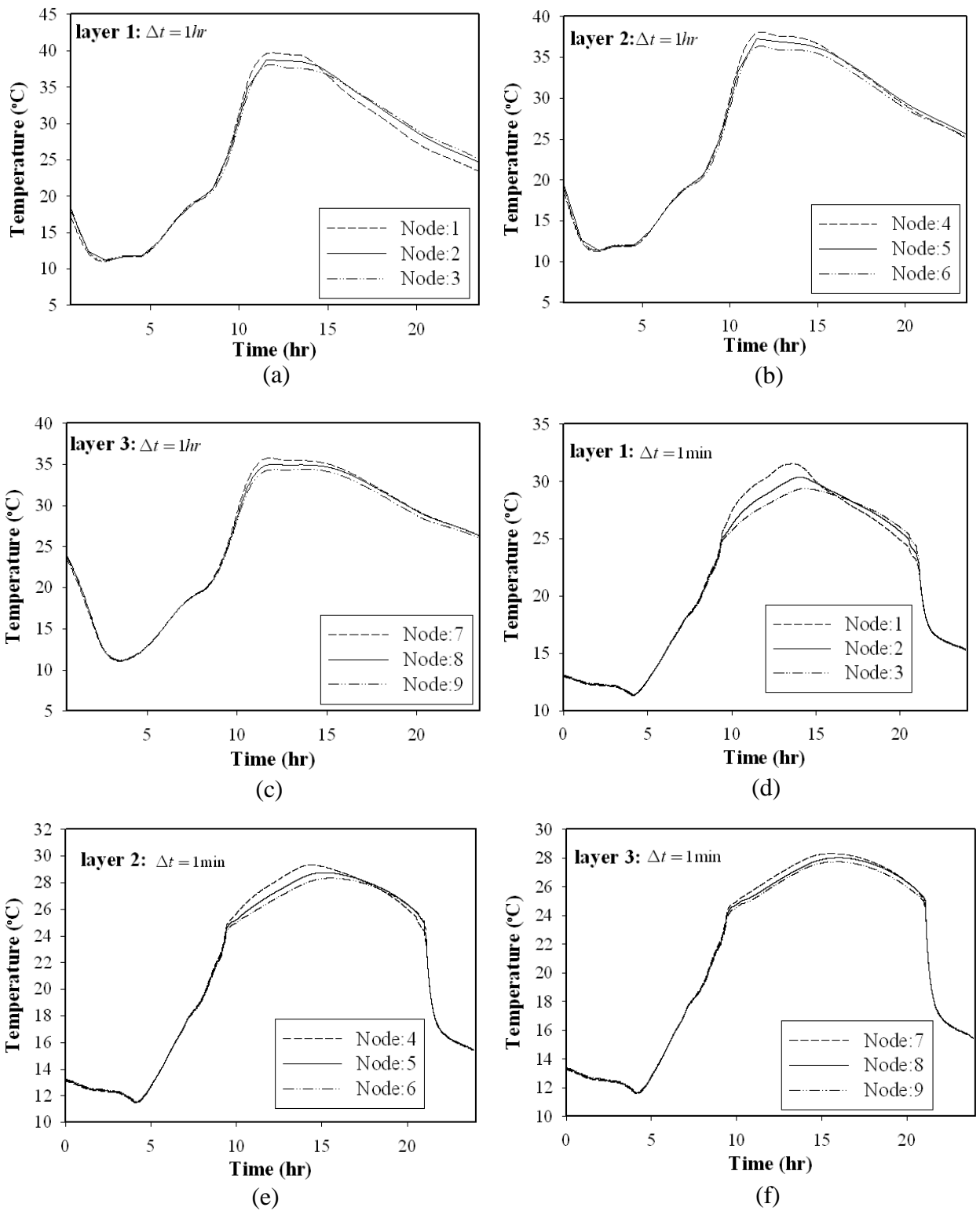
Figure 4-20: Modelling of a PCM layer divided into 3 layers and simulated using two different time steps:

1- $\Delta t = 1$ hr (a, b and c).

2- $\Delta t = 1$ min (d, e and f).

Figure 4-20 (d to f) shows agreement with the results found from the configuration of PCM with two layers under a small simulation time step. Increasing the PCM volume discretisation and using a small time step improves both temperature distribution and gives rise to a smooth temperature transition, increasing the utilisation of the phase change tracking (when compared with the one layer case).

4.10.3 Impact of convection effect

In order to analyse the influence of natural convection during the melting process, the variation of temperature with time were studied for a model with real conduction and a model with an effective conduction that incorporates the natural convection effect. The switch between real and effective conduction is shown in figure 4.2. From figure 4.21, a PCM layer with 3 virtual layers is selected where the PCM starts heating from one side giving rise to the phase change possibilities illustrated in section 4.9.
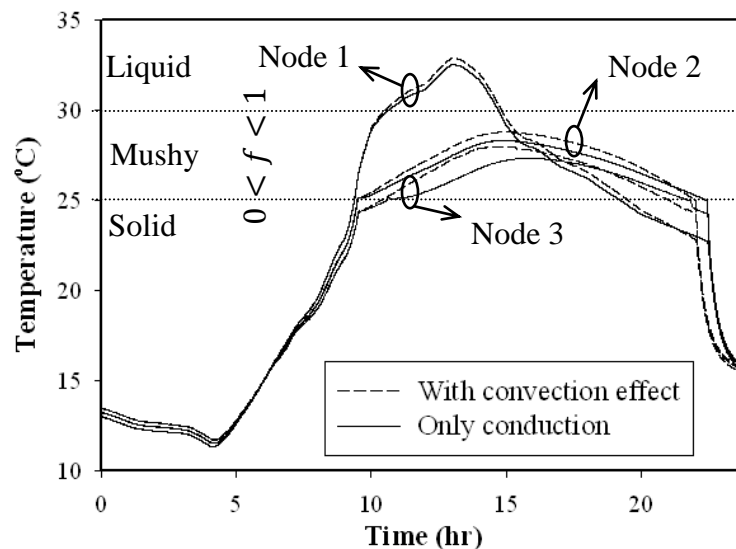
Figure 4-21: The effect of phase change with pure conduction and with natural convection included.

102

If the first virtual layer temperature is high enough to produce liquid, this melted layer is larger than the maximum thickness value as in equation 4.8, natural convection prevails in this layer and the effective thermal conductivity is calculated using equations 4.9 and 4.10. High node temperatures accelerate the liquid fraction and as a result increase the liquid region, ending the mushy region quickly across this layer and reaching the next layer. In the second layer, the low temperature variation allows the liquid fraction to increase slowly. In the charging process, this slow variation delays the melting process and controls this layer where the mushy region lasts for more time. In general, results show that if natural convection exists, then the effective heat conductivity of liquid PCM is enhanced.

4.11 Convection Versus Conduction for Phase Change Controllability

According to equation 2.16, the thermal conductivity k was varied between 0.1, 0.5, 5 and 25 W/m K, these values being typical for organic and inorganic PCM. The corresponding phase change enthalpy and temperature drops will be $L = 152$ kJ/kg and $\Delta T = T_{PCM} - T_f = 5°C$ for this example. The heat transfer resistance of the wall of the heat exchanger, as shown in figure 2-6, equals 0.001/250 for a wall thickness of 1 mm and aluminium thermal conductivity of 250 W/m.K. For the convection effect, h values were varied between 1, 2, 25 and 250 W/m^2.K, these corresponding to typical applications. The time necessary to solidify the entire PCM layer with the different conditions was then assessed as listed in table 4-2. The time to solidify for a depth $l = 10$ mm and thermal conductivity 0.1 W/m.K was $t_d =$ 88.67 hours; a long period that spans more than three days for low natural convection

equal 1 W/m^2.K. For a sensible heat façade wall, the above result would not be particularly disturbing. If a few sunny days occurred, then the sensible heat storage material would just get hotter, but within acceptable limits. However, if this happens to a surface containing PCM it might not be able to discharge its latent heat as will show in chapter 6. In a given PCM quantity, to improve the discharging process by increasing the property of the thermal conductivity of the phase change material is small compared with the increase in convection heat transfer coefficient, as shown in the table 4-3.

Table 4-3: Estimated discharge time, t_d, for a 10 mm PCM layer thickness and phase change temperature difference of 5˚C as shown in figure 2-6.

$k_s(W/m \cdot K)$	$h(W/m^2 \cdot K)$	$U(W/m^2 \cdot K)$	$t_d(hr)$
0.1	1	≈1	88.67
0.5			85.28
5			84.52
25			84.46
0.1	2	≈2	46.44
0.5			43
5			42.3
25			42.24
0.1	25	20	8.44
0.5		23.8	4.39
5		24.87	3.48
25		≈25	3.39
0.1	250	71.42	5.4
0.5		166.67	1.35
5		238	0.44
25		247.52	0.39

Due to the fact that the free convection discharge mode requires excessive time, forced convection is the preferable mode of heat transfer. From table 4-4, the low thermal conductivity of the PCM had a negative effect on the rate of heat transfer. The increase in the quantity of the PCM necessitates the need to increase the time of charging or discharging significantly. If the PV temperature was any higher, the charging time would become smaller. There needs to be tradeoffs between charge parameters to ensure that all available heat is stored and subsequently discharged. This may be possible in some cases depending on the PCM properties and the system's ability to move heat quickly in and out of storage.

Table 4-4: Charging time calculated using different quantities of PCM.

PCM thickness (m)	$\Delta T\ ^\circ$C	Charging time t_{ch}(hr)
0.001	1	0.093
	5	0.0187
0.01	1	9.375
	5	1.875
0.02	1	37.5
	5	7.5

The above estimates may be used to provide order-of-magnitude predictions of system performance. Once this is done, candidate PCMs can be selected. For example, using an alternative PCM with a higher melt temperature would tend to lower the degree of overheating of the PCM although not as effectively as controlling the heat loss at the surfaces. Heat removal is proportional to the film coefficients and to the temperature gradient available to drive it. Since the film coefficients for forced convection is limited by fan size and PV temperature, the heat flow from wall to air

will only be relatively large when the temperature of the wall face is high. Given an appropriate strategy for PCM discharge, a strong degree of controllability can be achieved.

4.12 PCM Quantity Optimisation

There are a number of factors in determining the appropriate quantity of PCM for a particular application. The phase change temperature limits represent the most important factors that must be considered for the purpose of ensuring repeated melting and solidification within the range of the diurnal temperature change. For PV application, the phase change temperature should be around the ambient temperature. However, to control the temperature of the PV cell close to the phase change temperature range for a prolonged period of time depends on the amount of material used and the boundary conditions (as shown in section 4.9). If a large thickness of material is used, part of the PCM will not melt or become solid within the daily change of temperature. Thus, only a portion of the PCM will be used and the system becomes less cost-effective. To determine the amount of PCM required, it is necessary to calculate the amount of heat that can be stored and then withdrawn from the internal surface of the PCM heat exchanger. In general, phase change will improve convection at the surface through the enhancement of natural convection inside the air gap. In the present example, a convective heat transfer coefficient of 2 W/m^2°C was assumed for the purpose of calculating the required thickness. In the case of discharging, the heat transfer from the inner surface of the PCM to the air gap leads to solidification of a portion of the PCM: the heat output from the PCM internal surface is equal to the heat extracted to a façade zone; in mathematical terms:

$$Q_{out} = A \cdot h \cdot \Delta T \cdot t_d$$

The necessary thickness of PCM and the time for release of the stored energy to the façade zone may be estimated from

$$Q_{out} = A \cdot h \cdot \Delta T \cdot t_d = A \cdot \rho_{sol} \cdot L \cdot X_{sol}$$

and therefore

$$\frac{X_{sol}}{t_d} = \frac{h \cdot \Delta T}{\rho_{sol} \cdot L}$$

For a PCM latent heat of $L = 172$ kJ/kg, density 785kg/m^3, temperature difference between air and PCM of $\Delta T = 5°$C and the PCM initially in the liquid phase, the result would be 0.267 mm/hr, which implies, for the boundary condition assumed here, about 0.27 mm of solid PCM front depth obtained per hour or about 2.67 mm on a daily cycle with 10 hours. The PCM is now discharging an amount of heat roughly equal to $135*10^6*0.00267=360.5$ kJ/m^2. For a PCM layer of 10 mm thickness, 7.33 mm will be under charging and therefore not used at the next cycle. As shown in table 4-2, improved discharging can be realised with forced convection. If the convection coefficient is increased to 7 W/m^2.K, the solid front moves to 0.93 mm/hr or 9.3 mm on a daily cycle with 10 hours. Here, all the heat stored in the PCM layer is rejected by convection and the PCM is ready to use in the next cycle. In the case of charging, if the maximum temperature of the PV layer reaches nearly 30°C, the thermal conductivity of the liquid is 0.2 W/m.K, and the PCM is initially in the solid phase at its melt temperature of 25°C, then the heat transferred by conduction to the PCM body will commence melting. The melt time for all the 10 mm thickness will be

$$t_{mel} = \frac{l^2 \rho_l L}{2 k_l \Delta T} = \frac{0.01^2 * 135 * 10^6}{2 * 0.2 * 5} = 1.875 \text{ hr}$$

For PCM thermal properties equal to that assumed above, the melting time will be 1.875 hr and the amount of heat stored will be equal to 1350 kJ/m². The discharging time for the same thickness will then be 10.3 hr. If the convection coefficient increases further to 25 W/m².K, the discharge time decreases to 3 hours indicating an improvement in the charging/discharging cycling efficiency.

In conclusion, with low values for the convection coefficient, the effect of increasing the thermal conductivity has little impact as shown in table 4-2. For a convection coefficient equal to 25 W/m².K, representing a gas with forced convection or a liquid with free convection, the discharging time is about 3 hours for a thermal conductivity equal to 0.2 W/m.K. For the case of natural convection in air, with a convection coefficient equal to 7 W/m².K, it would take around 1 hour to cool a 0.93 mm PCM layer.

Chapter 5 : Experimental Validation

5.1 Introduction

For the PV/PCM component to be fully characterised, a prototype was constructed and tested. This chapter reports the outcomes from experimental and theoretical testing studies. The objective is to determine the performance impact of the PCM. A steel container filled with a commercial blend of heavy cut hydrocarbons (paraffin) was used as the PCM and attached to a mono-crystalline PV module. In the following sections, the performance of the PV component with and without air-cooling is examined alongside the performance of the PV/PCM component, again with and without air gap cooling. The impact of applying PV/PCM in building design is then examined theoretically.

5.2 PV/PCM Prototype Setup

Figure 5-1 shows the PV/PCM prototype in cross section.
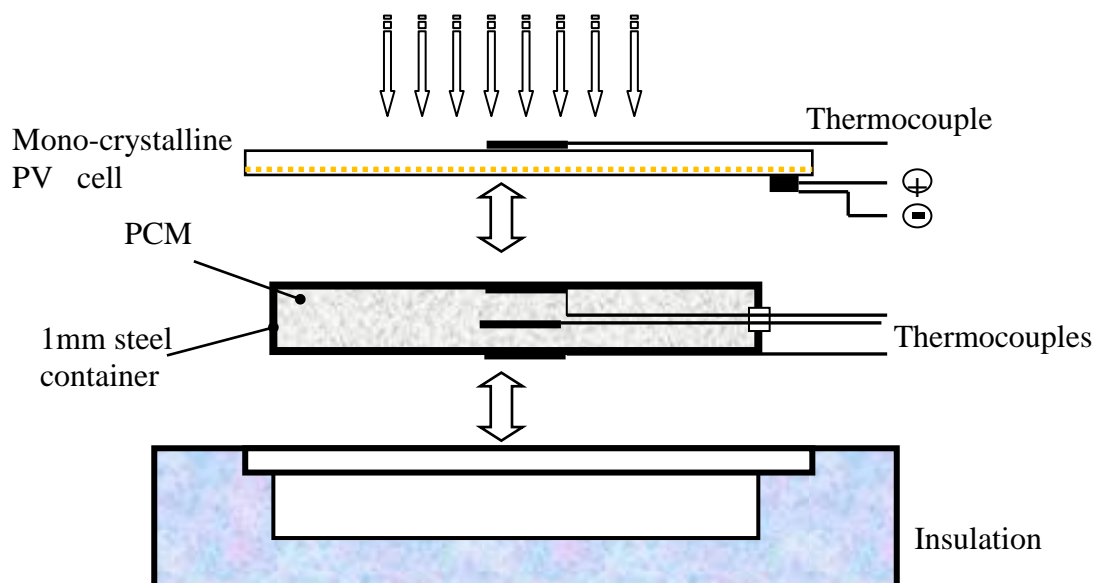
Figure 5-1: Prototype PV/PCM detailing.

This comprises a container assembled from steel plating (100mm *110mm*2mm) with an opening at the top. The thermal properties for steel used in

the analysis are density 7800 kg/m^3, specific heat capacity 502 J/kg.K and thermal conductivity 50 W/m.K. The PV component was used to close the container, so it represents the top surface. Adhesive material was used to glue the container edges to the bottom surface of the PV component to prevent edge effect. This process was preformed several times to avoid leaking of the PCM when in the liquid phase. The PCM in liquid form was injected into the container through a small orifice, with complete filling to ensure that no air was present inside the container. After filling, the orifice was sealed and the container insulated with cork. The PV/PCM component total mass was 0.255 kg of which the PCM was 0.155 kg. The technical specifications for the PCM and PV module cells are as follows.

5.2.1 PCM

The PCM is a commercially available organic solution material called PlusICEA25 (from Phase Change Material Products Limited, http://www.pcmproducts.net). This material is made from a blend of heavy cut hydrocarbons (paraffin wax) with a melting temperature of 25°C. PlusICEA25 is non-toxic, chemically inert with most materials and does not pose a danger to either health or the environment. A list of the principal thermal properties is given in table 5-1. Appendix (B) gives a thermal energy storage design guide for different PCM types.

5.2.2 PV

Two types of mono-crystalline PV cells were used: framed large panel and unframed small module. The unframed, 6V module was constructed from toughened

glass, with Tedlar backing as shown in figure 5-2; the specifications are given in table 5-2 and 5-3.

Table 5-1: The specification for PCM Type A25.

Commercial label: PCM type A25	Blend of heavy cut hydrocarbons
Form: solid-colours	White
Boiling point	>250°C
Freezing point	25°C
Density	770 kg/m^3
Conductivity	~0.2W/m K
Solubility in water	<0.01 mg/l
Viscosity at 20°C	3.7 cP
Flash point	>120°C
Vapour pressure	<0.046 kPa
Latent heat	135 MJ/m^3
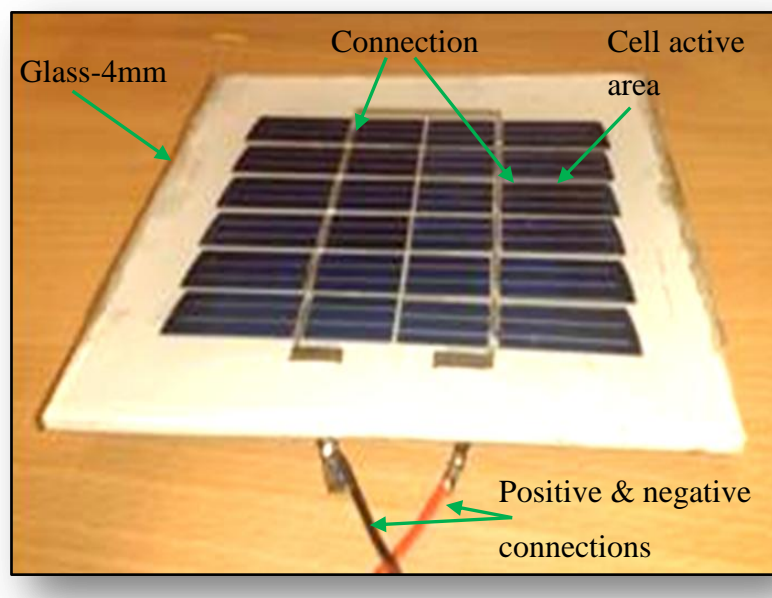
Figure 5-2: Mono-crystalline solar cell (Source: Sunshine Solar Company, product code UNF002, http://www.sunshine).

Table 5-2: Mono-crystalline solar cell specification.

Cell type	Mono-crystalline
Maximum voltage load	6 V
Maximum current load	250 mA
Size	130 mm x 130 mm
Weight	60g

Table 5-3: Solarex solar cell specification.

Cell type	Solarex
Max. power	51.3 W
OC voltage	21.1 V
SC current	3.23 A
Voltage at maximum power	17.1 V
Current at maximum power	3A

5.3 Instruments Used

5.3.1 Data logger

This captures the meteorological and performance data at short time intervals. The DL2e logger used (http://www.delta-t.co.uk/) is compatible with most sensors that give an output in terms of direct current voltage, resistance, count, frequency or status. It offers 15-60 analogue or counter inputs, 6-24 channels for PRT and 4-wire sensors, two resident digital inputs and two output relays as standard during programming; each channel can be set up for sensor type and range, conversion

factor, logging frequency (1 second to 24 hours) and valid reading range. Data collected from pyranometers, thermocouples and PV are stored in battery-backed RAM, with a capacity of 128 KB of readings. The DL2e comes complete with the Ls2W PC's software package.

The program interface can be used for system setup, controlling the logger and collecting the stored data. A library of sensor conversions is available to organise modem communications, automatic data collection and data graphing. In the present work, sampling and logging were undertaken at a 30 s frequency.

5.3.2 Thermocouples

Common types of thermocouples are given in table 5-4. The application range of these thermocouples includes the PCM's transitional temperature. Both T- and K-type thermocouples were used to sense the temperature of the PV/PCM component.

5.3.3 Pyranometer

A radiometer designed to measure the irradiance on a plane surface, normally from solar radiation and lamps. These instruments are used in meteorological research, solar energy research, material testing, and climate control in greenhouses and buildings. In this investigation, the Kipp and Zonen CM11 pyranometer was used, for which characteristics are given in table 5-5.

5.3.4 Solar simulator chamber

The experiments were conducted within an environmental chamber using a lighting gantry of mercury vapour bulbs. This chamber is located within the Energy

Systems Laboratory of the Department of Mechanical Engineering at the University of Strathclyde of Glasgow. The irradiance of the gantry was controlled using a potentiometer as shown in figure 5-3.

Table 5-4: Specifications of K and T type thermocouples.

Characteristic	K- type	T- type
Operational range ($^{\circ}$C)	-200 to 1350	-200 to 350
Sensitivity (μV/$^{\circ}$C)	41	43
*Absolute accuracy ($^{\circ}$C)	1.5	0.5-0.8

*http://www.microlink.co.uk/tctable.html

Table 5-5: Kipp and Zonen CM11 pranometer characteristics.

Sensitivity (x10^{-8}V/(W/m^2))	4.61
Spectral range (x10^{-6}m)	310-2800
Response time (s)	6
Directional error (W/m^2)	10
Maximum irradiance (W/m^2)	4000
Tilt error (%)	<0.2
Uncertainty in daily total (%)	<2

Figure 5-3: Solar simulator chamber parts: mercury vapour bulbs and potentiometer.

5.4   Experiment Setup

As shown in figures 5-1 and 5-4, the heat flux was assumed to be one-dimensional and orthogonal to the upper surface of the panel. Insulation was used to prevent edge effect so that all other surfaces could be considered adiabatic as shown in figure 5-5. The electrical power produced by the solar panel was calculated from the voltage drop across a series of electrical resistors. The data logger has the limitation that it can only measure up to 2 V. Since the maximum circuit voltage of the solar panel is more than this value, a potential divider circuit was set up and multiple voltage readings taken. The circuit diagram for this setup is shown in figure 5-4. The K- and T-type thermocouples are distributed over the top and bottom surfaces of the solar panel and PCM container. The data logger recorded the thermocouple average value at 30-second intervals. In order to determine the

temperature rise across the panel surface, the first experiment involved no panel cooling. The boundary conditions for temperature and light intensity were measured. Subsequent experiments with PV/PCM recorded the temperature of the PV upper and lower surfaces and the PCM container inside and outside (lower) surface as shown in figure 5-5. The temperature fluctuation at the PV surface was monitored by using several thermocouples. These thermocouples were first tested to ensure that the voltage output increased appropriately with increasing temperature. Several thermocouples were placed on the PV outer glass surface, while others were distributed inside the PCM container.
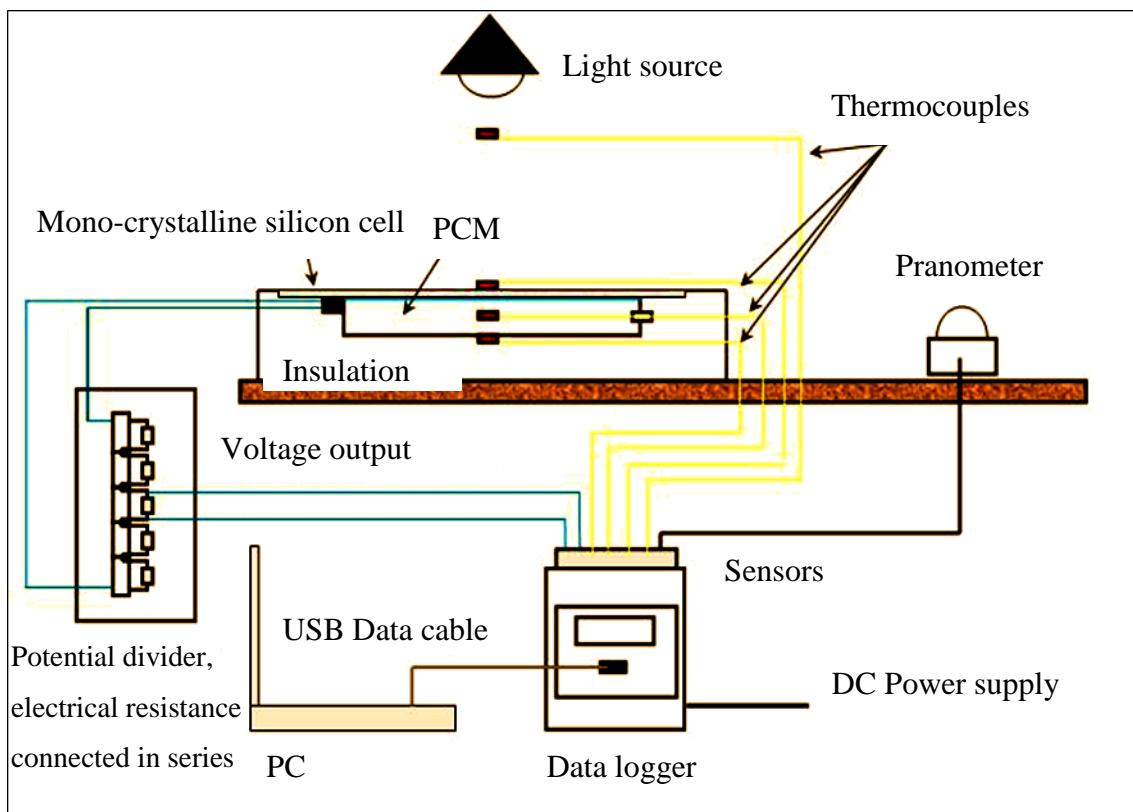
Figure 5-4: Experimental setup.

For data logging purposes a program was prepared using the DL2 software on a Dell Inspiron 6400 laptop. This allowed the properties of a given sensor to be selected and a corresponding channel allocated. When all the instruments were readied, the logging process was commenced and checks made to ensure that all sensors were working well. The recorded data was imported into Microsoft Windows XP Excel.
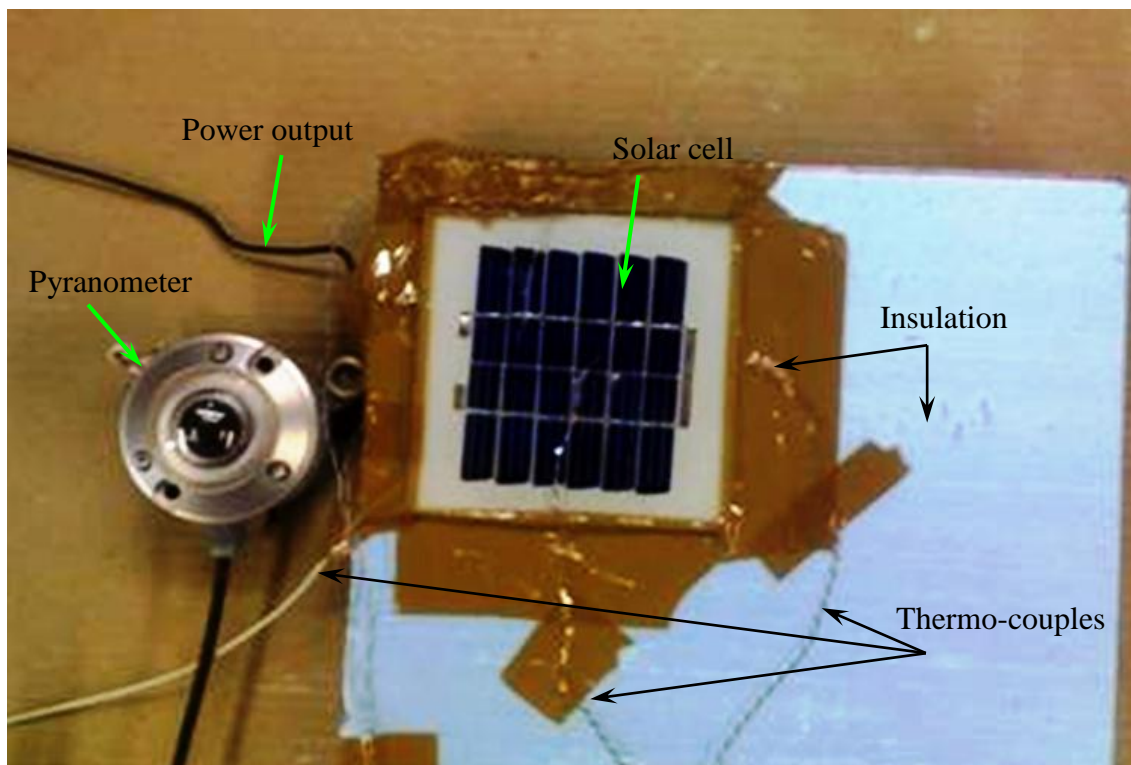
Figure 5-5: PV/PCM experiment setup.

The testing was carried out over a typical cycle, which included both charging and discharging process periods. For accuracy purposes, the experiments were repeated several times to reduce uncertainties and provide comparable results. Each experiment was continued until all of the PCM in the system had melted. When the solar simulator was switched off, the temperature in the system decreased and the PCM solidified again. The cycle was repeated when the system temperature

equalled the chamber temperature. The heating (charging) and cooling (discharging) process was as follows.

5.4.1 Charging process

The charging process is illustrate in Figure 5-6a.

(a)

(b)
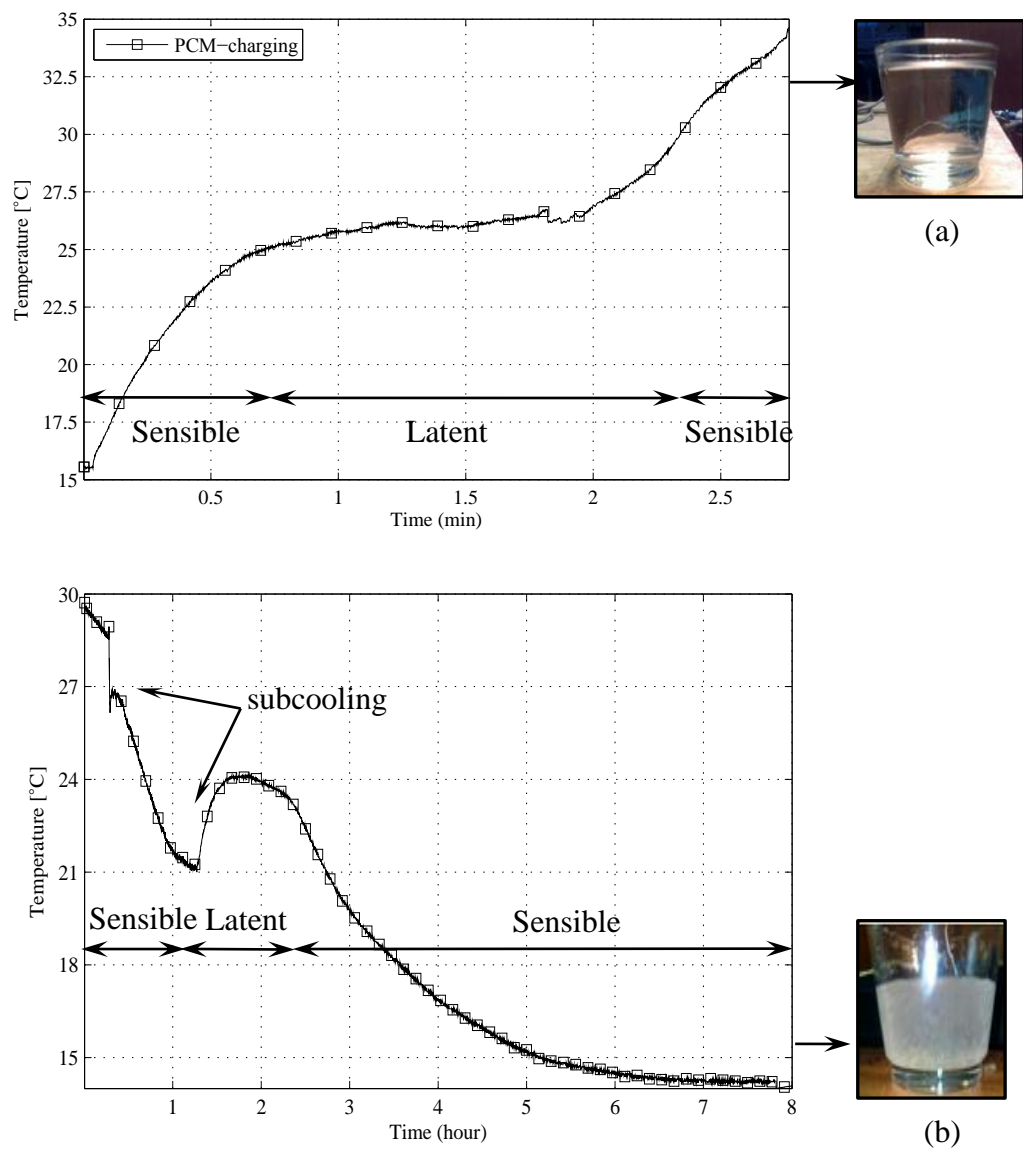
Figure 5-6: PCM temperature change throughout a) charging and b) discharging.

The solar simulator was heated until the temperature on the PCM external surface reached the melting temperature. Due to the sensible heating process, the solid PCM upper surface temperature starts to rise until a thin melting layer is

created. This layer continues to grow and the result is a slowing of the PCM temperature increase to a near constant value. When the liquid volume fraction becomes more than its solid counterpart, adding heat sensibly increases the PCM temperature. The temperature curve then flattens when the entire solid is melted and the system reaches its maximum temperature.

5.4.2 Discharging process

The discharge process is illustrated in figure 5-6b. After attaining the total PCM melted state, the heating process ceases and the cooling process activates naturally. It can identify three regions during the cooling process, the first region starts when liquid region lose a significant heat sensibly and a gradual decrease occurs in its temperature. This will continue until PCM reaches its melting temperature. Through this region, the liquid encounters two sub-cooling zones. The first appears early and its effect is limited by the presence of large amounts of liquid at high temperature (greater than the melting temperature). This situation does not allow the solid particles to persist and they return to the liquid phase. When the liquid reaches the melting temperature, a second stage super-cooled breakdown occurs. Now a large amount of latent heat is released into the super-cooled PCM. This energy causes the temperature of the liquid to rise again to its melting temperature. The PCM starts to solidify and solid particles grow in the liquid; this solidification process continues until the temperature levels out. When the solid volume fraction in the PCM is more than its liquid equivalent, the heat rejected from the phase change process becomes less than the cooling rate from the PCM to the chamber and finally the temperature will decrease sensibly.

5.5 Experimental Results

5.5.1 PV panel without cooling

In order to view the effect of the temperature rise across the surface of the panel, the first experiment entailed no panel cooling. The boundary conditions inside the chamber are given in figure 5-7. These conditions are approximately constant at 225 W/m² for light intensity and 20±1˚C for ambient air temperature above 10 cm from PV upper surface.
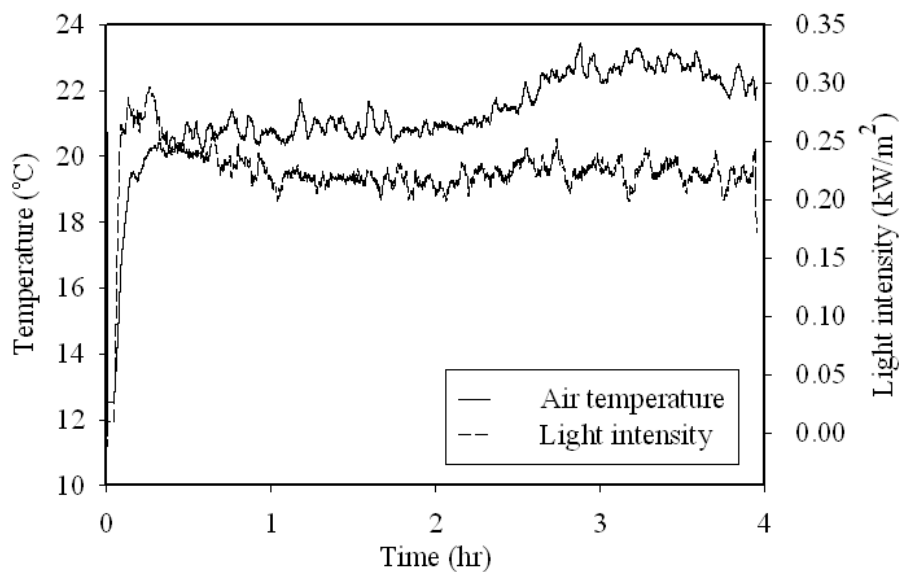
Figure 5-7: Boundary condition in solar simulator including light intensity and air temperature.

As the experiment runs, the temperature on the upper surface of the PV panel rises from ambient to around 46˚C, at which point it reaches its maximum value and levels off; the effect of the temperature rise on output voltage is shown in figure 5-8. The temperature increases rapidly and reaches a steady state when the heat input to the PV cell due to irradiation is equal to the ambient heat loss primarily due to convection. The steady state temperatures were attained after an elapsed time of 177 minutes.
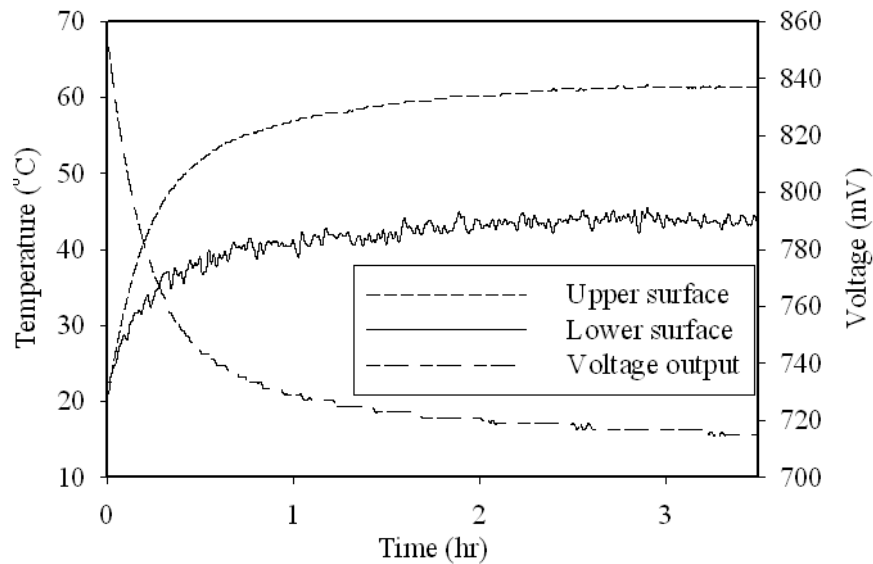
Figure 5-8: Solarex PV panel upper and lower surface temperatures and output voltage with insulation at the lower surface (no cooling).

The PV surface responds exponentially to the incident radiation and rises rapidly from the initial temperature, reaching almost 38°C after 38 minutes as shown in region number one. The temperature continues to rise, now linearly, for a longer period until it reaches 46°C after 140 minutes as shown in region two. The last region, number three, represents the temperature of the surface after stabilisation and continues to the end of the experiment; this is the upper limit temperature. As the temperature of the panel surface rises there exists an opposite effect on the actual output voltage; as the temperature approaches its maximum value, the voltage simultaneously approaches its minimum. This indicates an inverse correlation between temperature increase and power production. In this instance, a 31.4°C temperature rise corresponds to a 4.5V reduction per degree Celsius temperature increase. The lower inner PV surface temperature increased to its high level around 61°C; the PV cell temperature can be approximated as the average between the upper inner and the lower inner surface, here equal to 53.5°C. This temperature represents 28°C more than the phase change temperature.

5.5.2 PV with air cooling

For the PV component with the lower surface air cooled as shown in figure 5-9, it can be seen that the PV upper surface reaches a first maximum temperature of 32.4°C after 18 minutes, and a second maximum value of 34°C after 123 minutes.

5.5.3 Cooling PV using PCM *(lower surface without insulation)*

An additional experiment was undertaken in which the heat build-up across the panel was controlled to maintain the mean surface temperature lower than its maximum level as much as possible. This was achieved by packing the PCM container underneath the PV panel, thereby removing some of the heat from the surface. From figures 5-7 and 5-8, ambient temperature reach 20°C, the PV cell temperature can rise to over 45°C, PCM with a phase change temperature range of 25°C-30°C can be used. A comparison between the temperature rise profiles for this experiment and the previous one is shown in figure 5-9. The second curve represents the PV/PCM prototype. After five minutes, the upper PV surface temperature increases rapidly to PCM melting temperature 25°C. Between 5 and 56 minutes the temperature raises within phase change limits of 25°C-30°C. After 67 minutes, as the phase change process ends and all material becomes liquid, the additional heat absorbed by the PV/PCM causes its temperature to be increased sensibly and the curve levels out when the heat lost from the system by natural convection and radiation equals the heat gained. In the liquid PCM layer, natural convection effects increase the total effective conductivity, and this accelerates the phase change process and transfers heat from the upper PV surface to the lower PCM surface, as shown in figure 5-10.
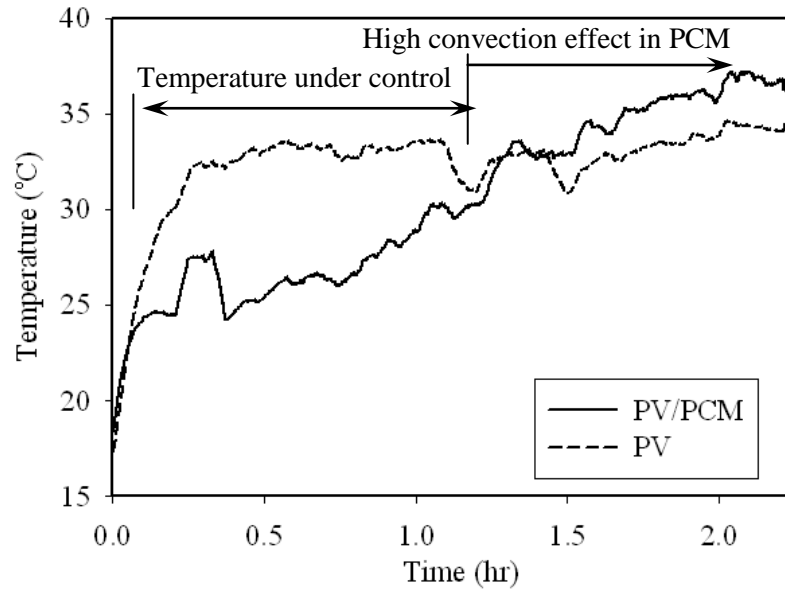
Figure 5-9: Upper surface temperatures for PV and PV/PCM with cooled lower surfaces via an air gap.

Figure 5-10: Section of the PV/PCM.

Poor cooling of the lower surface will accumulate the heat absorbed in the PCM layer and improve the internal heat convection; consequently, this will increase the PV and PCM temperatures rapidly, as shown in figure 5-9 (i.e. a high convection effect within the PCM). This convection effect is illustrated in figure 5-10. The heat transfers from the PV inner surface mainly by conduction. The PCM contact interface starts to melt and the liquid volume fraction increases. The convection and

density difference at the contact melting surface and PV inner surface increases the effective thermal conductivity of the PCM. From figure 5-9 it can be seen that as the liquid fraction increases, the heat energy accumulated and the temperature builds up rapidly.

5.5.4 Cooling PV using PCM (lower surface with insulation)

Here, the PCM is inserted into a block of cork to insulate the PCM heat sink lower surface as shown in figure 5-11. Because of the stratification behaviour of the phase change process, heat is accumulated and the temperature reaches a maximum value of above 50°C at lower surface. As shown in figure 5-11 through 5-12, the system temperature reaches a steady state value of 45°C after 80 minutes; the temperature build-up to 30°C due to the sensible heating of the solid PCM by conduction heat transfer shows little deviation from the reference system.
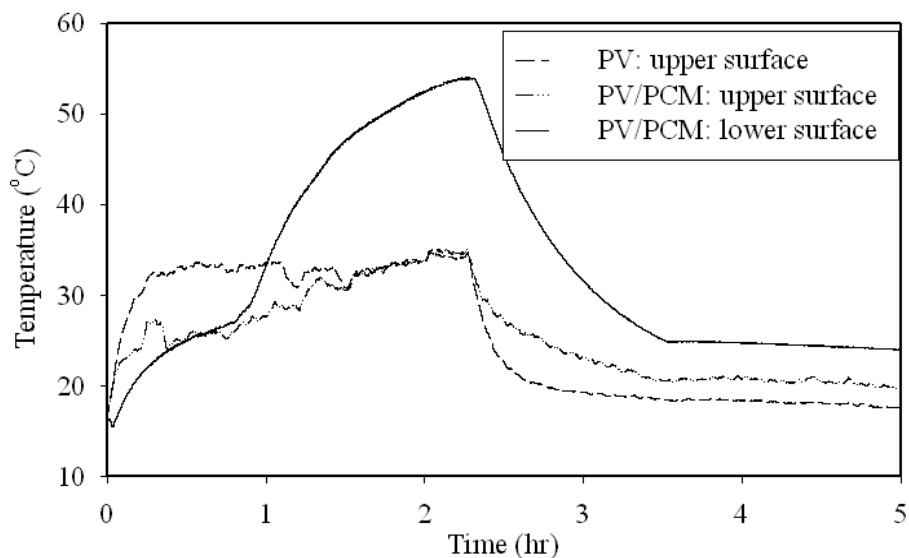
Figure 5-11: PV upper surface temperature with air gap and PV/PCM upper and lower surfaces temperatures over a complete heating and cooling cycle.

When the temperature of the front PV surface reached 30°C, the PCM layer in direct contact with the PV back surface reached its melting point. The gradient of the

temperature rise decreased and the temperature of the PV layer deviated from the reference value. After the PCM layer has begun to melt, the combination of convective heat transfer in the melted portion and conductive heat transfer in the solid portion continues.
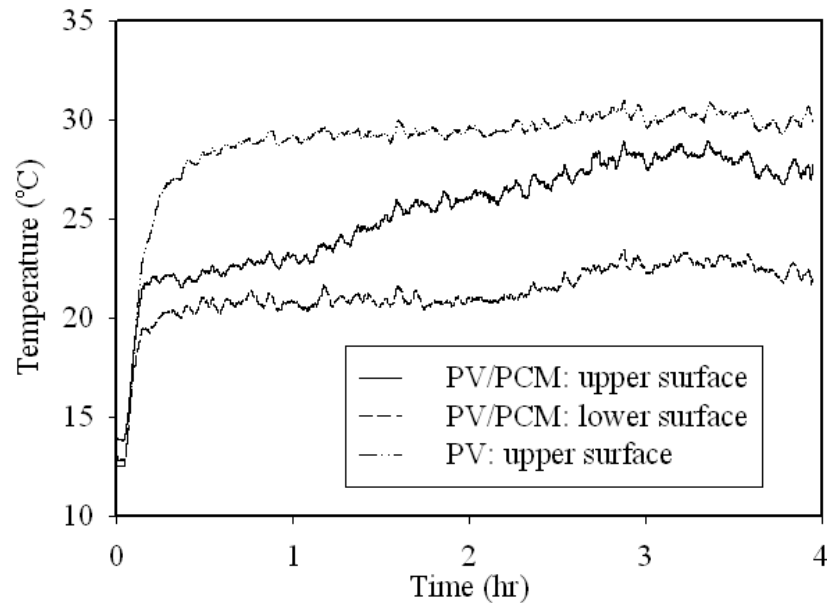
Figure 5-12: Comparison of upper surface temperatures for PV with air gap and PV/PCM with air gap.

The convective heat transfer continued to increase as the melt fraction increases, resulting in the increased sensible heating of the PCM. The absorption of heat continued until all the PCM had melted; this resulted in convection dominant heat transfer and sharply increased temperature gradient until the PV temperature flattened at its maximum value at the end of the experiment. With a full charging/discharging cycle as shown in figure 5-12, the absorbed heat in the PCM released at a low rate when compared with the temperature of the upper PV surface. In figure 5-11, the heat transfer direction is always upwards from the PV due to the insulation below the PCM heat sink. This raises the PV surface temperature more than would happen in the absence of the PCM heat sink. If the PCM heat sink were

exposed to air, the heat transfer direction would be downward as in figure 5-12. The following conclusions were drawn from the experiment results.

1. PV performance without cooling agrees with the literature (e.g. Skoplaki and Palyvos 2009; Roberts and Guariento 2009 and Eicker 2003) –the result indicates an inverse correlation between temperature increase and power production. Thus, PV cooling becomes a requirement.

2. Using PCM control elevates the PV temperature to around its transition point; the control time depends on the phase change temperature, the PV temperature and the boundary condition.

3. Again, the experiment agrees with the literature if an air gap is used to cool the PV. However, this method has limitations when compared with PCM use. In addition to the PV and boundary temperatures, it strongly depends on the heat balance between the PV outer and inners surfaces. PV temperature starts to increase rapidly until this balance is achieved. With PCM, the temperature increases more slowly than with an air gap.

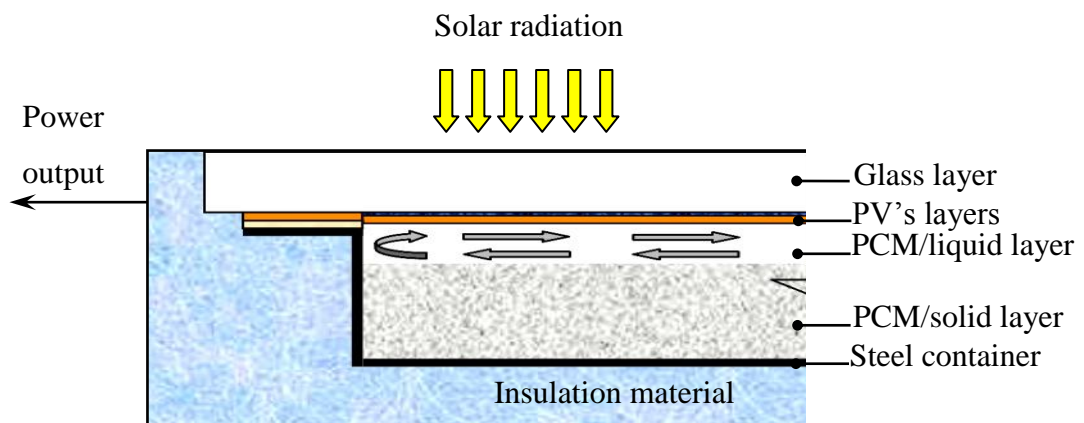4. In both approaches, poor cooling of the lower surface will accumulate the heat absorbed in the PCM layer and improve the internal heat convection; consequently, this will increase the PV and PCM temperatures rapidly.

Referring to figure 5-11, when there is no solar gain the PV temperature drops. At this point, the PCM is discharged and its heat is released in both directions. Unless the conduction on the outer surface of the PCM is greater, the heat will conduct back into the PV component. To prevent this reverse heat transfer, a high conductivity material may be used or an appropriate geometrical modification introduced. The PCM thickness must also be optimised. The problem here is that a

large PCM thickness will result in greater charging and discharging times that may be in conflict with the diurnal temperature variation. From figure 5-12, it can be seen that PCM with air ventilation allows for continuous charging/discharging, increasing the charging time in the presence of solar gain and decreases it at other times.

5.6 PCM Model Validation

A schematic diagram of the physical model is shown in figure 5-1; a counterpart numerical model was developed in ESP-r and simulation outcomes compared with the trends observed in experiments. Figure 5-13 shows the measured and predicted variation in PV/PCM upper surface temperature when the system is exposed to air-cooling from below. The boundary conditions as shown in figure 5-7 were used in the simulations.
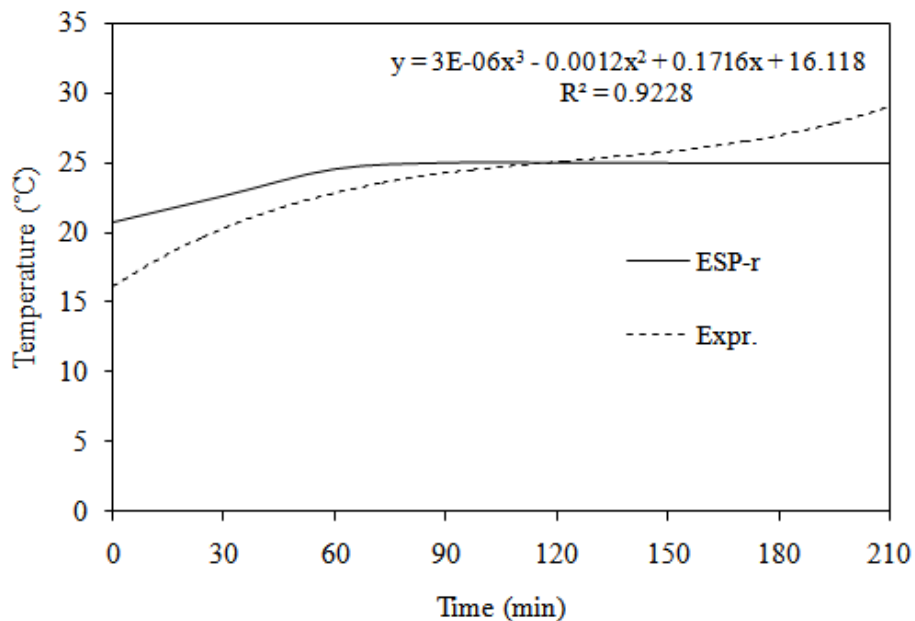
Figure 5-13: ESP-r model validation: the predicted PV upper surface temperature compared with that observed in experiment for PV/PCM without insulation at the lower surface.

The direct normal solar radiation was held constant at 225 W/m^2, the ambient temperature at 20˚C (recorded 10 cm above the PV upper surface) and the local air speed identically zero. PCM thermo-physical properties for A25 PCM types were used to represent the material in the solid phase: these data are given in Appendix (A). In figure 5.13, experimental data shows the temperature of PCM increases with a slowing-down rate as time goes on (before melting), which is different from the corresponding numerical results. This can be attributed to the more heat loss as the temperature rises. However, in the present one-dimensional analysis the perfect insulation boundary condition has been used, neglecting the heat loss at the boundary, and thereby leading to nearly straight heating lines shown in numerical results. The variable convection at the PV upper surface acting to increase the heat loss and decrease the temperature, this possibility was studied via a parametric analysis in which the surface heat transfer coefficient was systematically varied. From figure 5-13, when the temperature of the front PV surface reached the phase change temperature, the PCM layer in direct contact with the PV back surface reached its melting point, at which time a melt front progressed from the PV bottom surface to the top layer of the PCM and heat was stored in latent as well as sensible forms. When the temperature of the front PV surface reached the phase change temperature, the PCM layer in direct contact with the PV back surface reached its melting point, at which time a melt front progressed upwards from the PV bottom surface and heat was stored in latent as well as in sensible forms. After the PCM layer had begun to melt, the combination of convective heat transfer in the melted portion, and conductive heat transfer in the solid portion, ensured that the PV surface remained within the phase change temperature range. Experimentally, sensible

heating dominated where heat is stored in the solid PCM in the form of specific heat. The measured readings show that this process requires more time than was evident within the simulation results. This is due to the high variation of temperature and intensity of light that is striking the surface. After two hours of the experiment, the temperature had risen to over 25˚C. This resulted in convection dominated heat transfer, with the temperature gradient sharply increased until the PV temperature flattened out at its maximum value. This behaviour can be explained as a reaction to a decrease in the heat dissipated by unstable convection. This problem and others were solved in the simulation by reducing the simulation time step for the PCM module calculations; it was then possible to reduce the temperature oscillations. The simulation results were then in good agreement with the experimental values.

Chapter 6 : Strategies for Effective Integration of PV/PCM in Buildings

6.1 PV/PCM Installation Effect

A schematic diagram of three physical systems is shown in figure D-1. The counterpart numerical models were established in ESP-r and simulation outcomes compared with the trends observed in the experiments. PV/PCM structures were then integrated into the external south wall of an ESP-r hypothetical office block model as described in table D-1. The models were then exposed to real boundary conditions representing the variations of solar radiation and external temperature throughout the simulated period; the PV/PCM construction was modelled as a multi-layer system, with each layer represented by thermal properties and geometry identical to that employed in the experimental work. The module was simulated under realistic outdoor conditions using the modified algorithms as incorporated in ESP-r. For the case without PCM, the PV temperature was in the range 59°C-61°C as shown in figure 6-1.
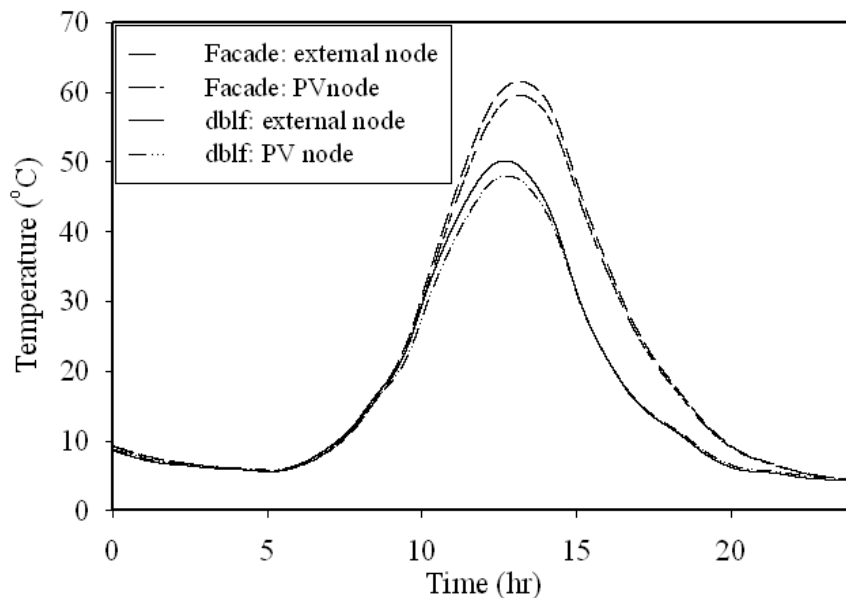
Figure 6-1: Temperature profiles for PV/PCM without phase change effect.

As the temperature increased, the band gap of the intrinsic semiconductor shrank, and the open circuit voltage V_{oc}, decreased. At the same time, the lower band gap allows more incident energy to be absorbed because a greater percentage of the incident light has enough energy to raise charge carriers from the valence band to the conduction band, resulting in a larger photocurrent result. The increase in the current corresponding to a given temperature rise is however proportionately lower than the decrease in voltage. Hence, the efficiency of the cell is reduced. The efficiency can be improved by cooling the cells via, for example, passing cool air in a duct behind the façade (or, as in this work, introducing PCM in intimate contact with the PV layer). The active ventilation of conventional curtain wall PV facades allows a reduction of cell operating temperatures of around 10˚C, resulting in an increase in the electrical power output as shown in figure 6-2.
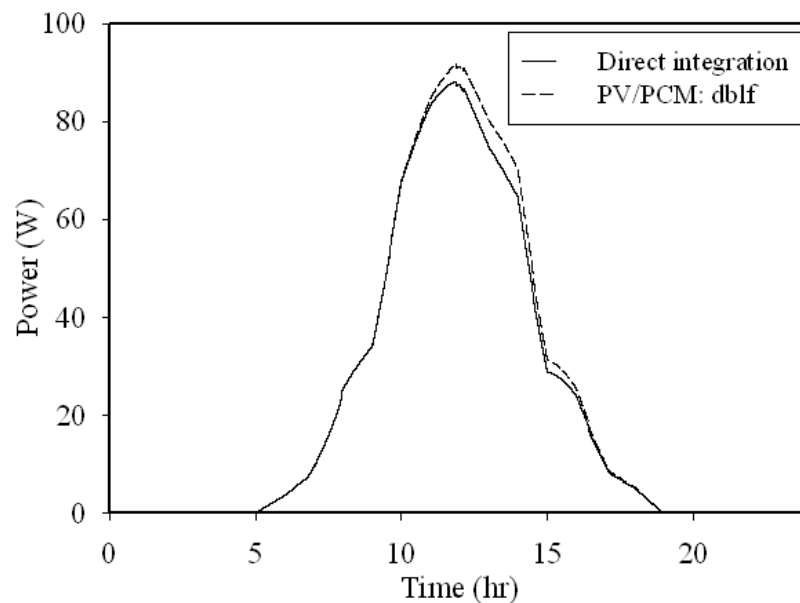
Figure 6-2: PV power output without phase change effect using two configurations, direct and in-direct installation.

After the PV surface temperature increased to above melting temperature, the PCM temperature is nearly constant as shown in figure 6-3 and 6-4. This active

reduction keeps the temperature controlled around 30°C, which leads to an increase in the maximum electrical power output as shown in figure 6-5. From figure 6-3, the delay in the discharging process leads to a decrease in the PCM latent heat utilisation in the later charging period; as a result, the PCM and PV temperatures increase. The effect of air-cooling via a duct behind the PV façade improves the phase change cycling significantly by removing all or part of the heat absorbed by the PCM as shown in figure 6-4.
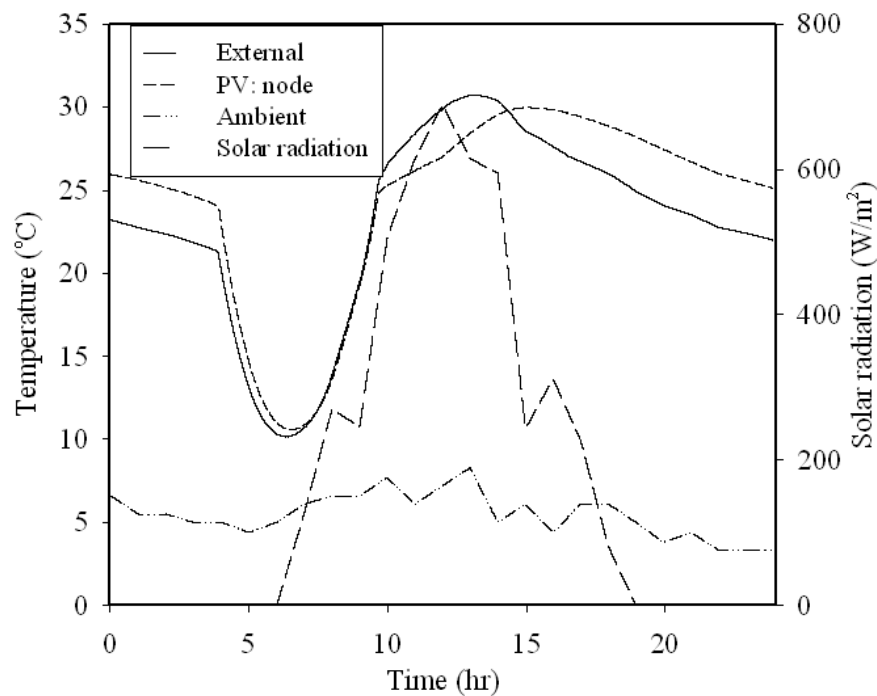
Figure 6-3: Temperature profiles for PV/PCM in direct contact (no air gap).

In insulated and non-ventilated PV/PCM facades, the PV surface temperature will be more than the PCM melting temperature for long periods of time when compared with PV/PCM with air cooling as shown in figure 6-2. However, in direct integration, because the PCM layer takes more time to complete the discharging process, the PV upper surface has a higher temperature for a prolonged period of time.
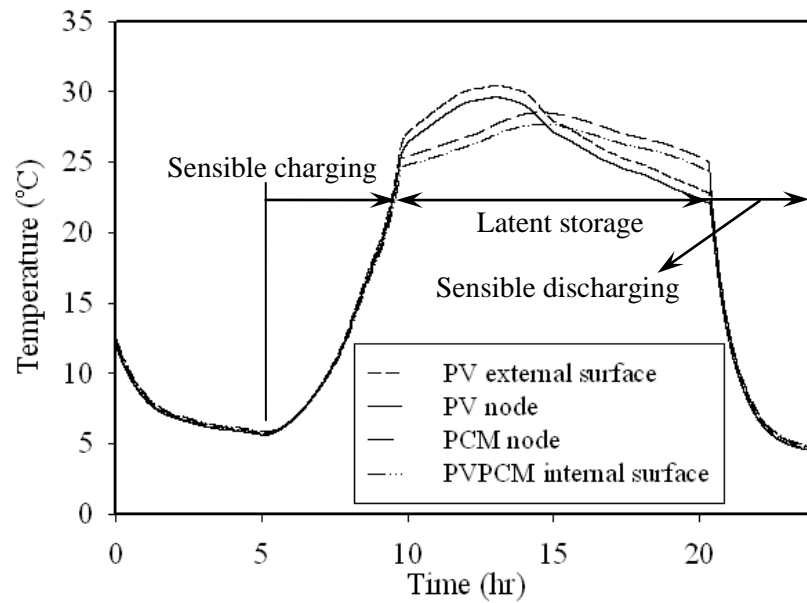
Figure 6-4: Temperature profiles for PV/PCM integrated within façade.
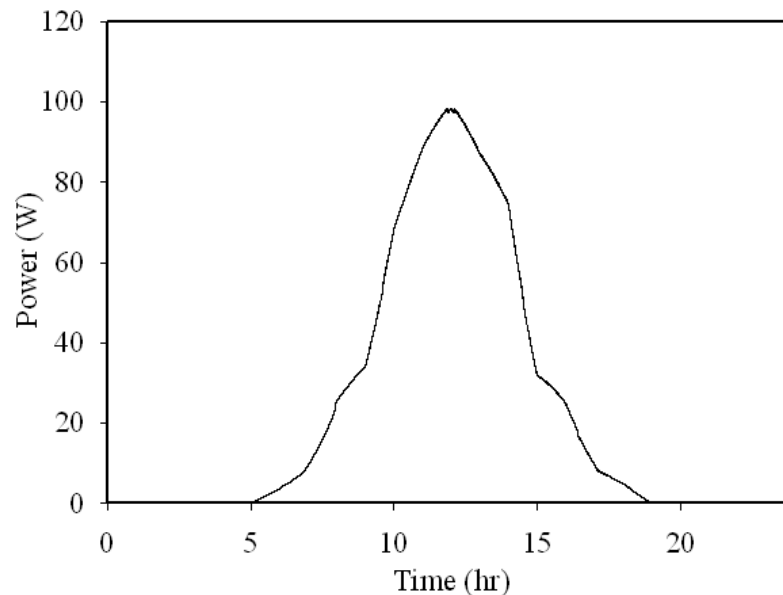
Figure 6-5: PV power output with phase change cooling in both direct and in-direct configuration.

6.2 Changing the PCM Optical Properties

Modelling of transparent and opaque PV/PCM components was undertaken to study the effects of optical property changes on performance. The geometry of the ESP-r building model corresponds to a two-storey block. Within the model, only the

façade component is taken into account and treated as three connected zones. The south side of the building is formed by two types of PV/PCM panels, one transparent, the other opaque as shown in figure E-1. The PV panels have dimensions 1m∗5.4m: one panel comprises crystalline silicon solar cells encapsulated in EVA in a low-iron glass/glass system with a PCM layer; the other an opaque panel constructed from crystalline silicon solar cells encapsulated in EVA in a low-iron/glass-aluminium plate with PCM. The non-south facing opaque walls are constructed of metal with insulation and external steel covering. Glass windows of dimension 1m ∗ 5.4m are fitted on each façade and represent the middle surface between the PV/PCM and other surfaces as shown in figure E-1. The facade is constructed with a 10 cm air gap, which allows exterior air to enter at the base of the facade and exit at the top.
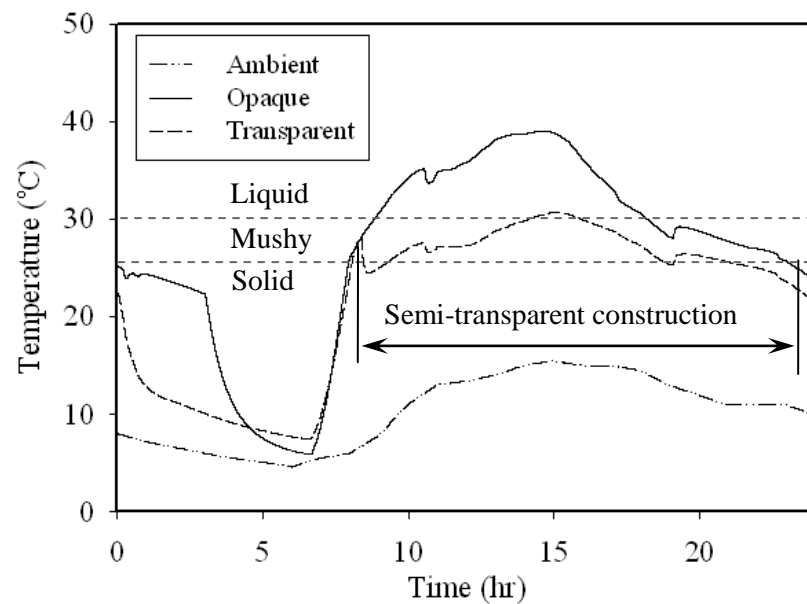
Figure 6-6: External surface temperature for different PV/PCM construction types and optical properties within a semi-transparent component with PCM phase change at 25˚C-30˚C for the façade at the second level.

The façade is separated from the other zones by a double glazed construction representing the back surface of the air channel. From figure 4-9, it can be seen that the external glass surface receives the incident solar radiation, where part of it is absorbed, part reflected and the rest transmitted to the next PV layer. Part of the transmitted component is absorbed at the PV node and converted to electrical power (the remainder being realised as heat). Initially, the PCM in the solid phase absorbs part of the received solar energy, reflecting the rest back into the PV and glass nodes.

The temperature curve of figure 6-6 shows the PCM behaviour. A round sunrise, part of the solar radiation is absorbed and stored in the PCM, the temperature rising until the process of melting begins. The melting process takes a few hours, during which time the PCM remains at the phase change temperature, as shown in figures 6-6 through 6-8. With all material in the liquid state, the PCM behaves like any other sensible heat storage material. When the temperature drops below the solidification temperature around sunset, the PCM starts to crystallise.
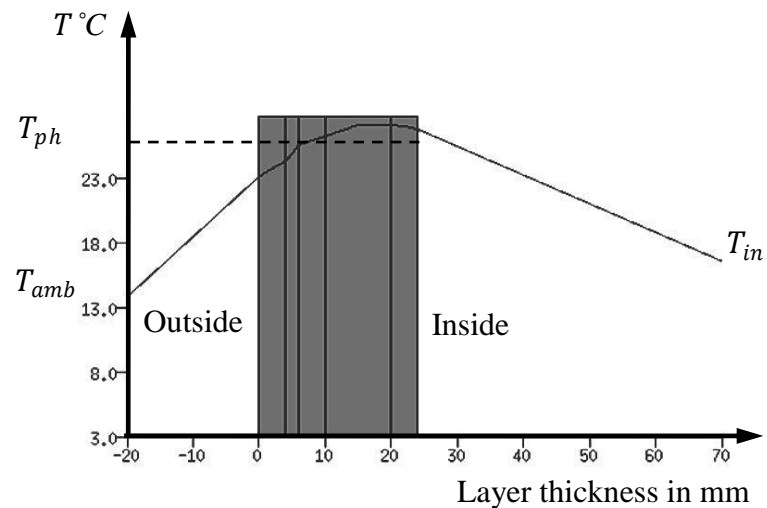
Figure 6-7: External temperature in transparent construction with variation in PCM optical properties and phase change at 25°C-30°C.

137
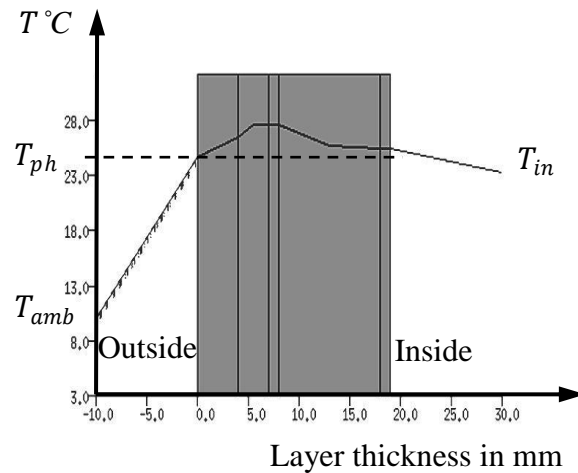
Figure 6-8: PV/PCM temperature in opaque construction with PCM phase change at 25°C.

The energy set free during solidification raises the temperature of the PCM again to the melting point. It then takes several hours to discharge the PCM. In the liquid state, the PCM is a non-scattering, clear and transparent fluid as shown in figure 5-8A; the liquid has high transmittance value in the visible range. With some paraffins, the transmittance decreases at longer wavelengths due to absorption being lower than with salt hydrate type PCMs. In the solid state, the transmittance decreases to about 0.5 in the visual range (Weinlader *et al* 2005). This is mainly due to scattering processes within the material as shown in figure 5-8B. In general, the transmittance in the visible spectral range is nearly independent of wavelength; this prevents any change in the colour of transmitted light, which is an important consideration in daylight designs. The PCM filters out the thermal radiation and, additionally, by the process of phase change, reduces the amount of penetrating heat until the PCM is totally in the liquid phase. The semi-transparent optical property of the PV/PCM façade is shown in figure 6-9.
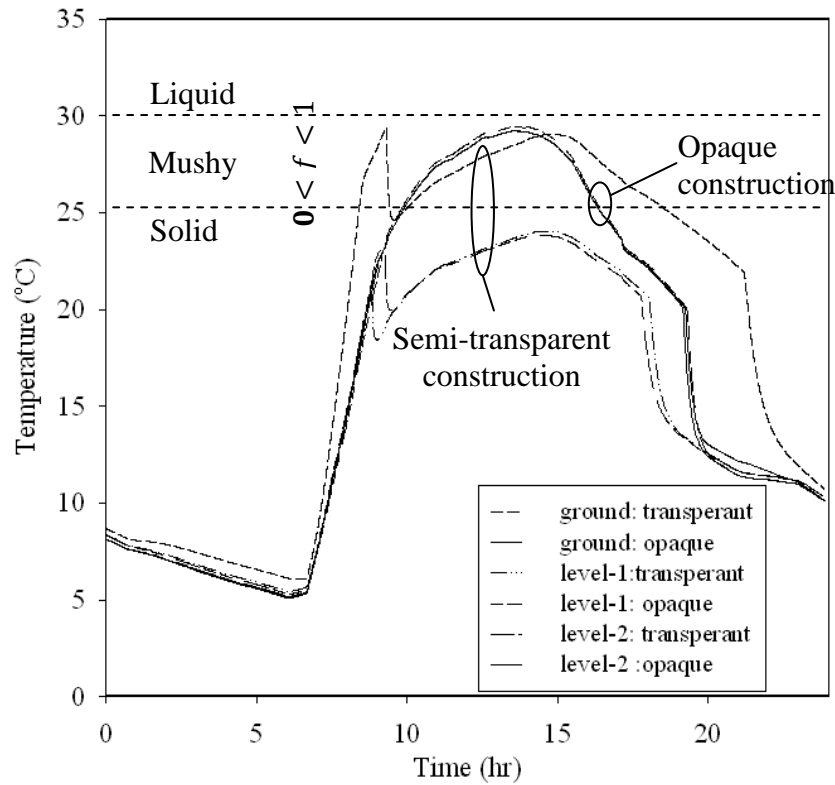
Figure 6-9: External surface temperatures with optical properties varied and heat transfer coefficients set at 7 W/m^2°C for inside surfaces and 25 W/m^2°C at external surfaces; PCM phase change at 25°C-30°C.

A sensitivity study showed that the modelled PV thermal performance is significantly influenced by the choice of convection coefficients in the air gap, particularly by the external convective/radiative heat transfer coefficients (Strachan 1998). The simulations imposed fixed external heat transfer coefficients in place of the buoyancy driven values normally calculated on a time step basis by ESP-r. The values were fixed at 7 W/m^2°C at internal surfaces and 25 W/m^2°C at external surfaces. Figure 6-9 shows the sensitivity of the predicted external surface temperature to the heat transfer at external and internal surfaces. The external surface temperatures reduced for both construction types. For both transparent and opaque constructions, the PCM temperature increases sensibly until it reaches its melting

temperature of 25°C where the phase change effect starts storing latent heat. Through this process, the PCM and PV temperature varies within upper and lower phase change temperature limits of 25°C and 30°C respectively. With the transparent construction, the PCM node temperatures increase until the melting temperature is attained.
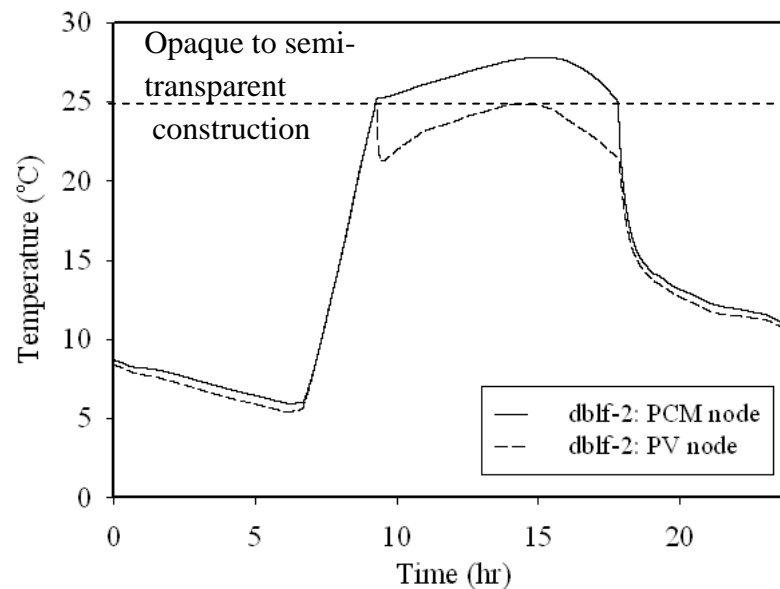
Figure 6-10: The temperature curves for PV and PCM nodes within a transparent construction. The external and internal heat transfer coefficients are 7 W/m^2°C and 25 W/m^2°C respectively.

When the liquid fraction starts growing, a portion of the solar radiation is transmitted; however, if the transmitted value become significant, this will reducing the PV node temperature as shown in (figures 6-8, 6-9 and 6-10) relative to the opaque structure result given in figure 6-11. With the opaque construction, all the non-reflected solar radiation is absorbed in the PV nodes, and a large part of this is converted to heat at the PV node to raise its temperature. Heat is then transferred by conduction to the PCM node, increasing its temperature into the phase change range as the stored latent heat then discharges to the air gap at night as shown in figure 6-11.
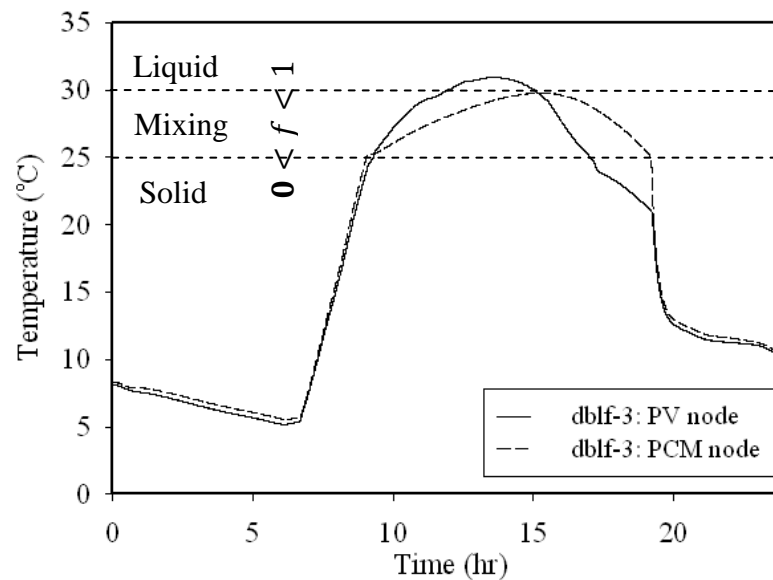
Figure 6-11: The temperature curves for PV and PCM nodes within an opaque construction.

6.3 Coupling the PV/PCM Component to the Building Domain

A strategy that works in conjunction with the building control system and takes into account off-peak and on-peak loadings gives the basis for an appropriate solution for efficient phase change utilisation. The merits of using PCM appear only within the phase change state period. For applications that use PCM, the long phase change process time means efficient control for temperature variation and efficient use of the PCM latent heat. A conventional thermal energy storage and control system based on building management systems can be assessed to achieve optimum savings and power shifting in buildings, as shown in figure 6-13.

In order for the PCM to be effective, three criteria have to be met:

1. The PCM's transition temperature has to be within an acceptable range, depending on the specific climate region.

141

2. The heat energy generated within the PV node must be enough to complete the charging process.

3. Natural/mechanical ventilation inside the air gap is required effectively discharge the PCM to ready it for the next cycle.

The larger the diurnal temperature variation, the better the PCM charging-discharging process will be without the need for auxiliary equipment such as a fan. However, when the diurnal temperature variation is low, the opportunity for the PCM to continue charging is less, and the PCM's temperature is increased sensibly after the phase change had been completed. The liquid PCM layer works as an insulation material; this leads to an elevated PV temperature. This imposes a restriction on the PCM discharging process. In summer, the building's facade acts as an exhaust duct for the building ventilation system (figure 6-12).
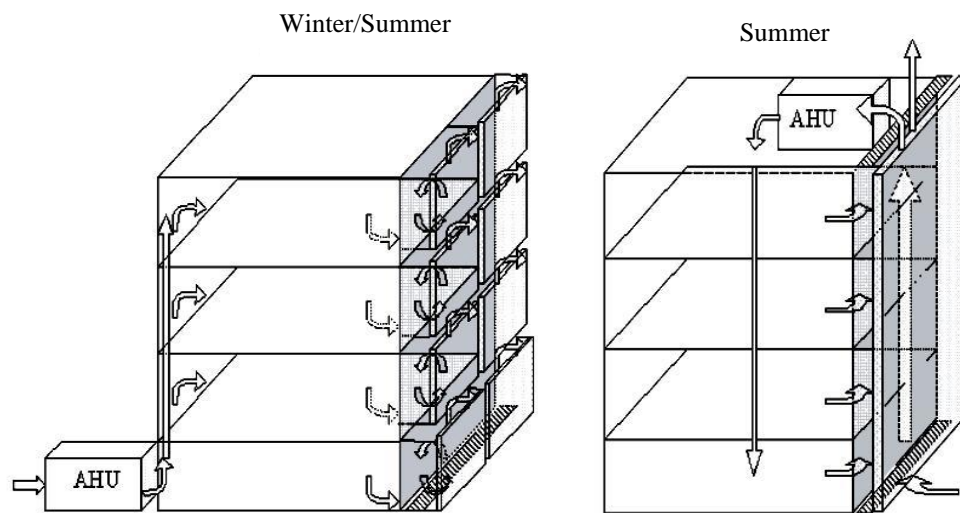
Figure 6-12: Double façade works as a) a pre-heater for the supply air and b) an exhaust duct for the ventilation system.

The exhaust air is ventilated from the building zones into the façade cavity where it is accelerated upward due to the absorption of heat from the PCM internal

surface; this effect reduces the required fan size and therefore the auxiliary power consumption. The ventilation system can switch between natural and forced flow in a manner that achieves efficient heat transfer by convection; this depends on the PCM transition temperature, the ambient temperature, and the ventilation strategy. In winter, the heat stored in PCM can improve the air ventilation system by pre-heating the air before it is supplied to the air handling unit or the building directly; this will result in an energy consumption reduction, as shown in figure 6-13.
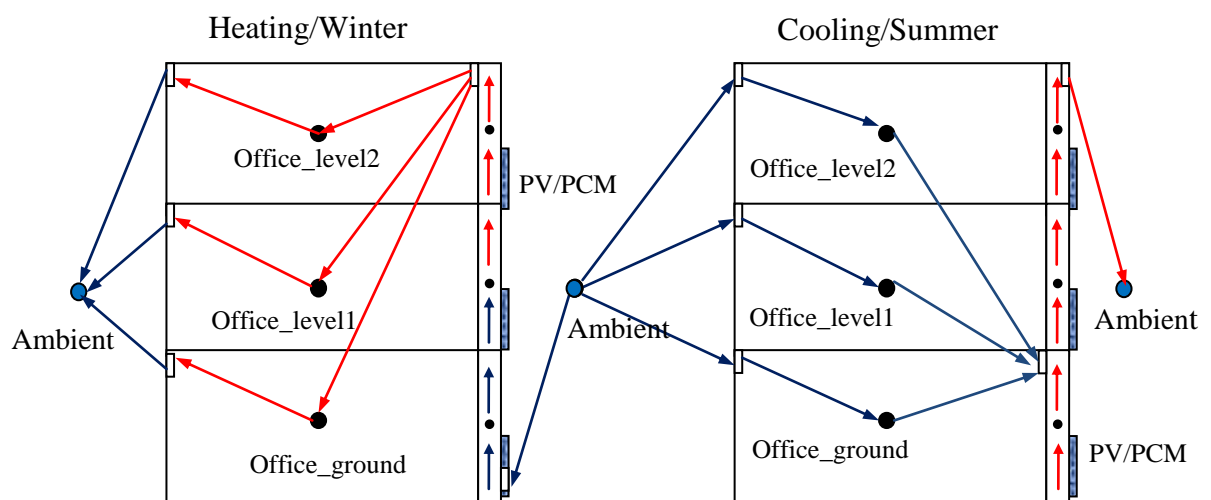
Figure 6-13: Air flow network for heating and cooling strategies using a double façade with PV/PCM.

6.3.1 Control strategy

Consider the three physical models shown in figure 6-13. The PV/PCM structure is integrated into the external south wall in a multi-office model with description as given in table E-1. This opaque surface is exposed to real boundary conditions shown in figure 6-15.

6.3.1.1 during heating periods

The outdoor air is taken in at the lower part of the façade and is preheated in the cavity and is immediately rejected towards the building zones, or connected to the ventilation system to supply air to the central air conditioning system as illustrated in figure 6-14. Exterior openings control the airflow rate as well as temperature. Then, through the central ventilation system, the air enters the building at the required temperature.

6.3.1.2 during cooling periods

The air comes from the inside of the building and is evacuated towards the outside. The ventilation of the façade thus makes it possible to evacuate the air from the building. The air is extracted through the openings at the upper part of the façade: this strategy is usually applied to double-skin facades in multi-storey buildings. The risk of offices being overheated during the summer months is high when the design of the double façade is not coupled properly with the strategy of the HVAC system. An efficient control system needs to be employed so that the indoor temperature is within the comfort range in order to reduce the energy consumption. A successful application can only be achieved when the contributions of all devices are synchronised by an integral control system. Figure 6-14 shows such a control system, which is required to fulfil three tasks via the coordination of passive and active components:

1. keep the level of the temperature inside the building within the comfort zone;

2. supply sufficient ventilation air; and

3. ensure effective latent heat utilisation.

In ESP-r, control loops allow the modelling of hybrid ventilation strategies, where the shift from natural ventilation to mechanical ventilation is achieved based on a control algorithm. The natural ventilation mode is given priority; the mechanical ventilation mode only being triggered when the natural ventilation driving forces become inadequate.
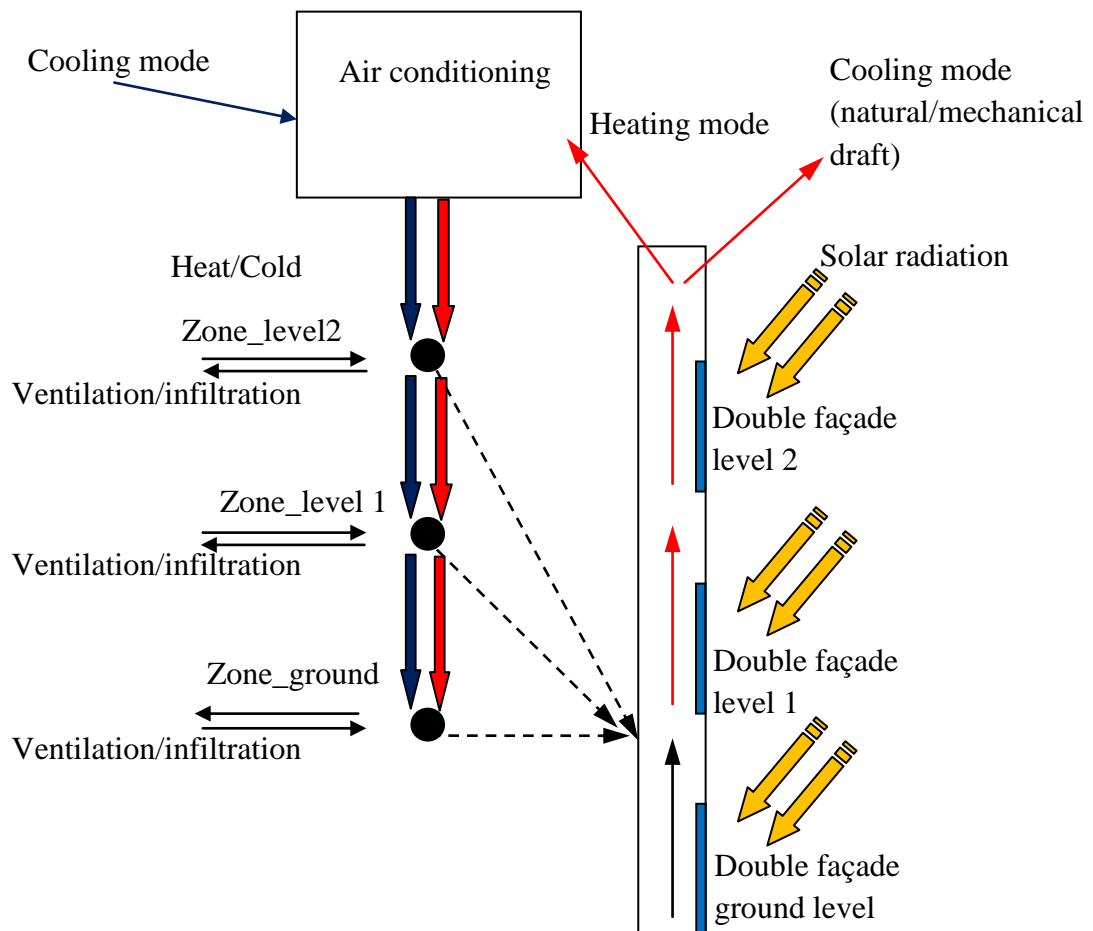
Figure 6-14: Schematic diagram showing the integration of ventilation plant and internal flow paths for heating and cooling requirements.

Table 6-1 represents the control strategy that is applied within this model. The maximum applied load for heating and cooling equals 10 KW during the occupied period (8-17 hr) when the zone temperature is controlled around 23°C. The model simulation takes into consideration zone operation as shown in table 6-2. The

heat gain sources are from occupants, lights, and airflow (both infiltration and ventilation). The PV specifications are given in table 6-3.

Table 6-1: Model control strategy.

Period number	Control-Loop	*Heating*	*Set-point*
1	0 hr-8 hr	0	20 ˚C
2	8 hr-17 hr	10 *kW*	
3	17 hr-24 hr	0	
Period number	Control-Loop	*Cooling*	*Set-point*
1	0 hr-8 hr	0	23 ˚C
2	8 hr-17 hr	10 kW	
3	17 hr-24 hr	0	

Table 6-2: Casual gains inside offices.

Casual gains in each zone:	*Sensible*	*Load type*
0 hr-7 hr	116 W	
7 hr-17 hr	1.056 kW	Occupant + light
17 hr-24 hr	116 W	
Air flow	*Infiltration*	*Ventilation*
0 hr-24 hr	ach/hr	m^3/s
	0.0	0.03-1.9

Table 6-3: PV panel specification.

PV Module type	BP Saturn BP 585	SOLAREX MSX 550	RMS100
Peak power at STC (W)	84.96	49.17	97.18
Open circuit voltage (V)	22.1	20.9	43.8
Short circuit current (A)	5.0	3.08	3.10
Voltage at maximum power point (V)	18.0	16.9	34.1
Current at maximum power point (A)	4.72	2.91	2.85
No. of series connected cells (-)	36	36	72
No. of parallel connected branches (-)	1	1	1
No. of panels in the PV/PCM surface (-)	12	12	12
Short circuit current temperature (A/˚C)	(0.065±0.015)%	0.00032	0.00084
Open circuit voltage temperature (mV/˚C)	-(80±10)	-0.0041	-0.0046

6.3.2 Cooling phase

Cold climate conditions: The simulations performed with climatic representative of the average climate shown in figure 6-15. The weather data recorded and consist of 12 actual months. For this study, a sunny summer day (1-7 July) been chosen. The modelled day preceded by the simulation of 13 previous days to take account of the effect of inertia. The outside temperature evolves between 10˚C and 24˚C. The maximum and minimum direct and diffuse solar irradiance varies between 750-450

W/m^2 and 215-120 W/m^2 respectively. In a building with a South-facing double skin facade, it is sometimes difficult to apply the strategy of daytime natural ventilation. Indeed, ventilation by extraction through the double skin is difficult and is a function of the wind direction. The double skin with top opening has good performance under conditions where the opening is on the leeward side of the wind. The office zones (figure 6-16) start to over heat and are cooled according to the strategy shown in figure 6-14 using the control plan summarised in table 6-1.
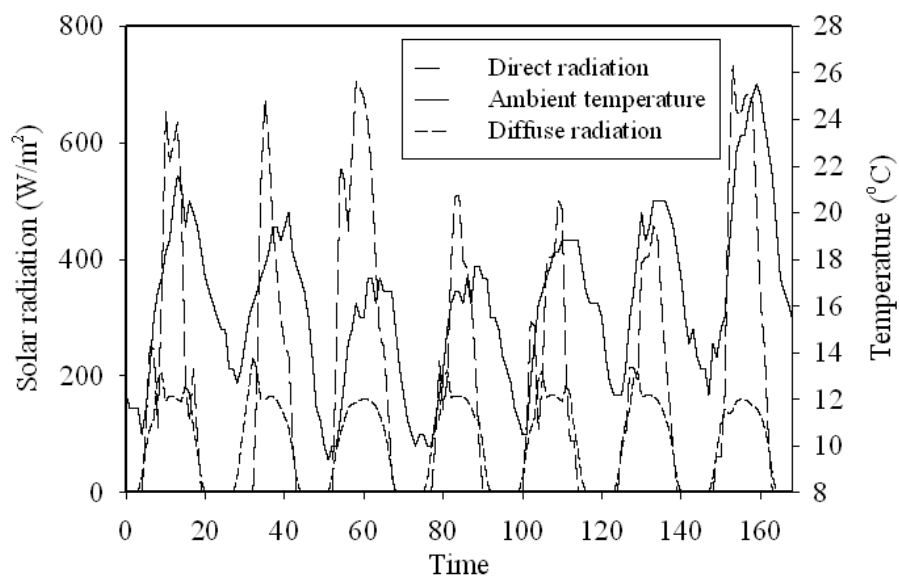
Figure 6-15: Temperature and direct/diffuse solar radiation boundary conditions for the cold climate for period 1-7 July.

From 7 a.m. to 5 p.m., the airflow passes from the outside and is used to cool the building before passing to the outside via the double facade. During the day, the double facade temperature remains lower than ambient because it is cooled by air coming from the building zones. This extends the PCM charging process. During the night, the temperature in the double facade remains higher than ambient because there is only one top-level opening and because the PCM discharging time keeps the PV/PCM inner surfaces at a high temperature. This improves the stack effect.

Through this control strategy, the temperature of a zone is sensed and an appropriate action taken at some relevant actuation point, e.g. a change to the flow rate of air delivered to the zone from an air handling unit or an adjustment to the amount of air flow that enters the building zones directly from outside. Figure 6-17 illustrates the temperature for the internal surfaces of the PV/PCM when controlled in the range 25˚C-30˚C. This may be compared to the case of surfaces without PCM as shown in figure 6-18.
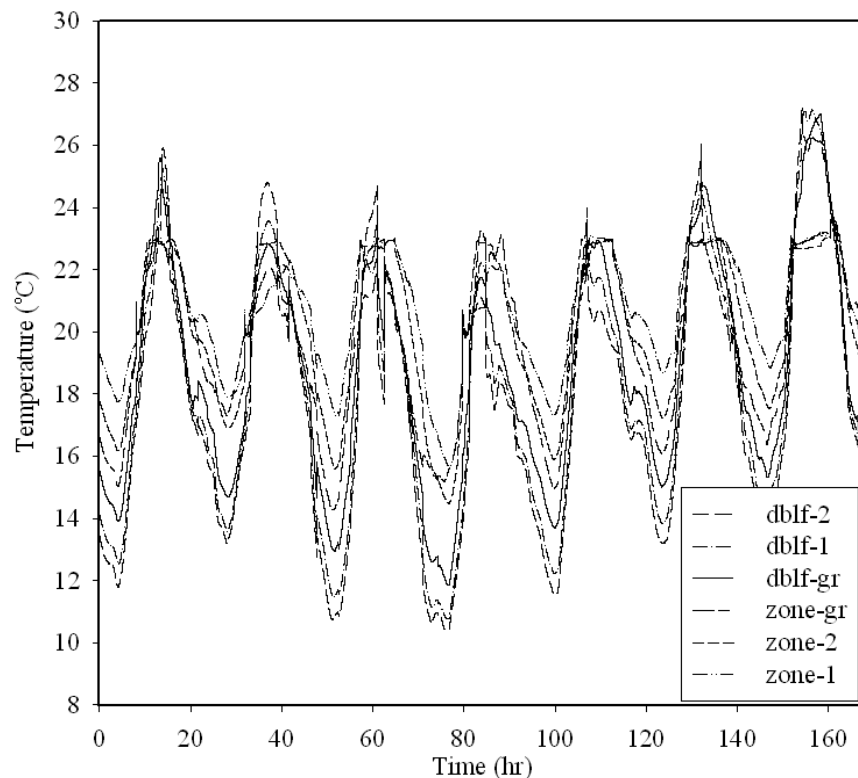
Figure 6-16: Internal zone temperature variation for offices and facades. The surface convection coefficient used is 2 W/m^2˚C; ventilation is induced naturally where no fan required.

From figure 6-16, during mid-day the air flow occurs from an unhelpful direction (almost at the second level) and the hot air of the double facade enters the zone. The second level is partially contaminated by the air from the lower levels resulting in the need for a mechanical air supply with the resulting increase in the

electricity. During the night, the decreasing ambient temperature allows the cooling system to be switched off. On the other hand, this will reduce the discharging time for the PCM layer and affect the double facade draught, thus reducing the amount of air that enters the building from outside. The advantage of this situation is that it controls the amount of ventilation air and prevents the need for building heating.
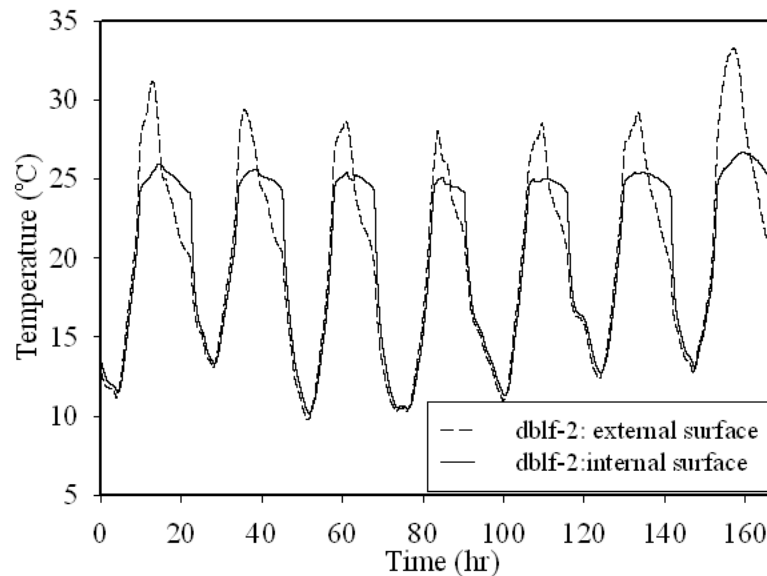
Figure 6-17: Internal and external surfaces temperature variation for the second level façade when naturally ventilated (h_c=2 W/m$^{2\circ}$C).

As explained in chapters 2 and 4, the discharge time is a crucial factor in PCM behaviour because it dictates the release of heat at the PV/PCM surface; when the discharge time is sufficient, the PCM internal surface temperature will be greater than when PCM is not used (figure 6-17). On other hand, the internal surface temperature without PCM can reach higher values than when the PCM is included. This improves the draught within the façade (figure 6-19). This advantage has a limitation beside PV high temperature when compared with the case when PCM is

included (figure 6-17): the temperature will decrease rapidly and the improvement in draught will be limited.
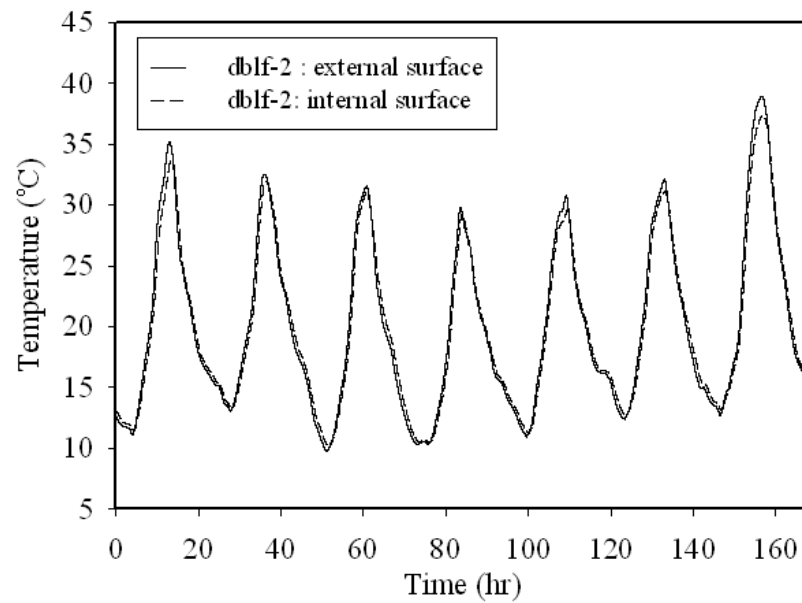
Figure 6-18: Internal and external PV surfaces temperature variation for second level façade without PCM effect when naturally ventilated (h_c=2 W/m^2°C).
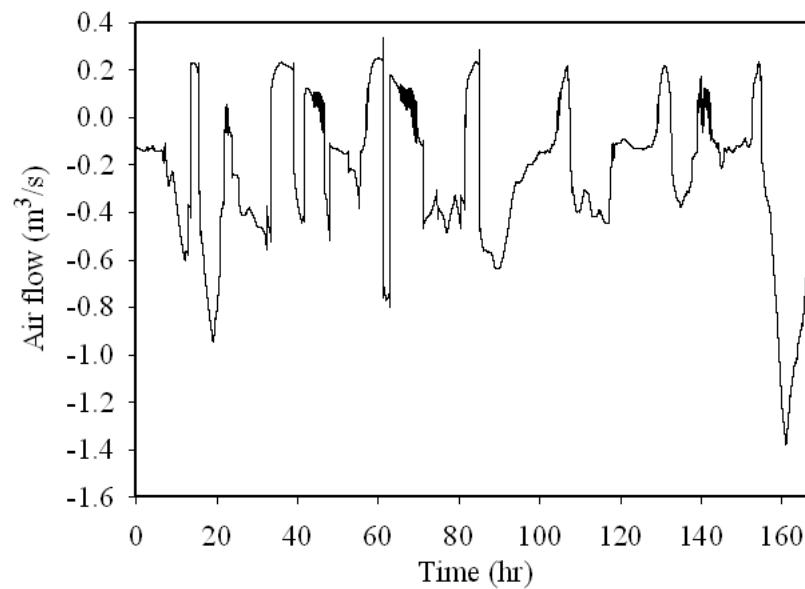
Figure 6-19: Air flow exhausted from the second façade to external with natural drought (h_c=2 W/m^2°C).

Table 6-4: Performance of PCM storage unit under cold climate (1-7 July) and using different phase change temperatures.

Phase change range	PCM node			PV node		Inside surface
	$> T_m$	$> T_s$	Max.˚C	$> T_s$	Max.˚C	>23˚C
23˚C-25˚C	43.7%	14.7%	30.17	17%	31.03	41.3%
25˚C -30˚C	33.6%	0%	29.77	2%	31.07	35.7%
No PCM	-	-	-	-	36.1	27.6%
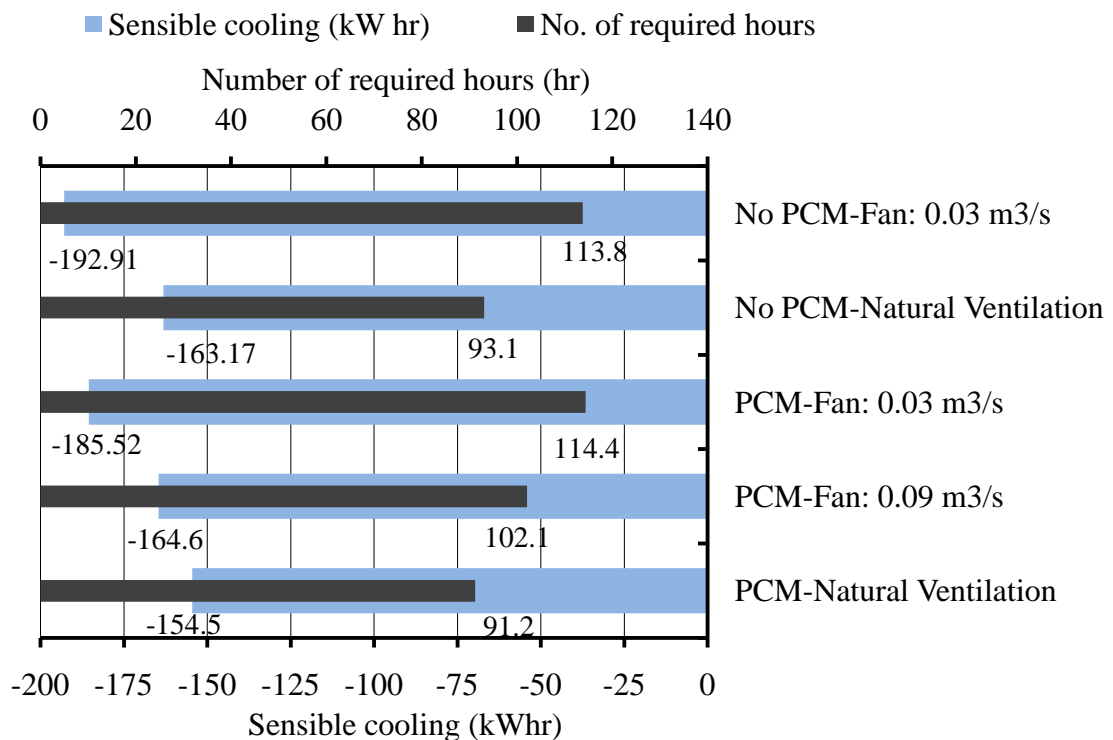
Figure 6-20: Cooling load and number of hours required for different ventilation strategies for double façade with and without PCM.

From figure 6-20 the minimum consumption takes place with PCM under a natural ventilation strategy. Compared with the same model but without PCM (but with natural ventilation), there is a reduction in the cooling requirement of 10.67

kWhr or 6.5%. The total time needed to run the cooling system is 10.98 hours. From table 6-4, the PCM maintains the PV/PCM internal surface in contact with the air gap at around 23°C for 35.7% and 41.3% respectively of the total time comparing with 27.6% for the surface without PCM. The total reduction in energy consumption decreased when the PV/PCM model ventilation strategy was switched to use a fan as shown in figure 6-20. A comparison with the results of natural ventilation for both cases shows a convergence of results with an advantage in the case of a model including PCM due to the maintenance of the PV/PCM internal surfaces temperature at a higher value even after the decrease of solar radiation. From figure 6-21, the use of PCM reduces the PV surface temperature to 35.6°C and increases the power output to 504.6W.
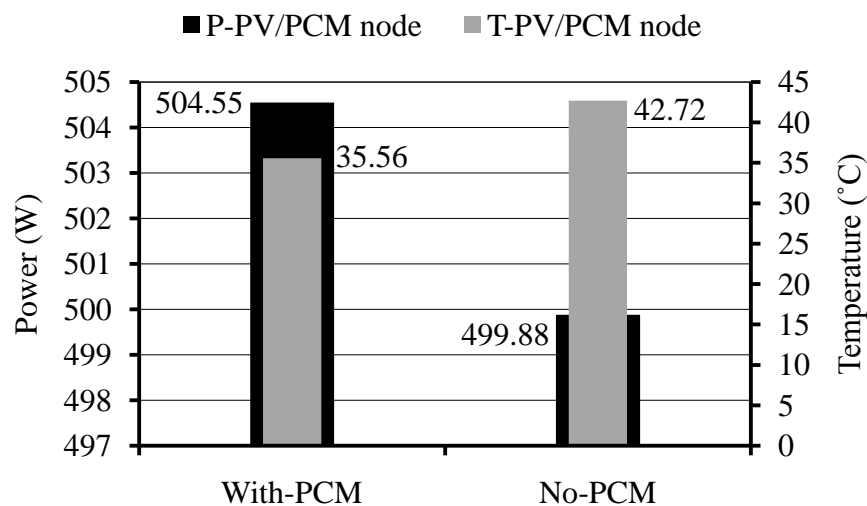
Figure 6-21: Maximum PV power produced for double façade with and without PCM (PV module used is BP Saturn (BP 585)).

Compared with the same model but without the presence of the effect of the PCM, there is an increase in the PV productive capacity of up to 0.924%, which is

nearly equal to 4.67 W with a decrease in PV temperature up to 7.7˚C. This means a
total increase of up to 0.608 W/˚C.
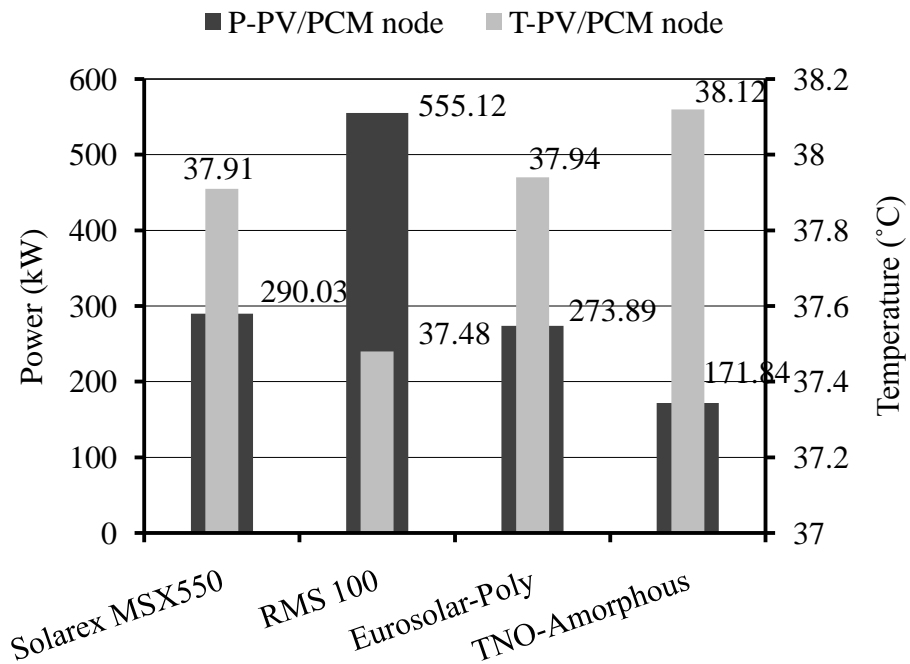
Figure 6-22: Different types of PV panels used and integrated with PCM.
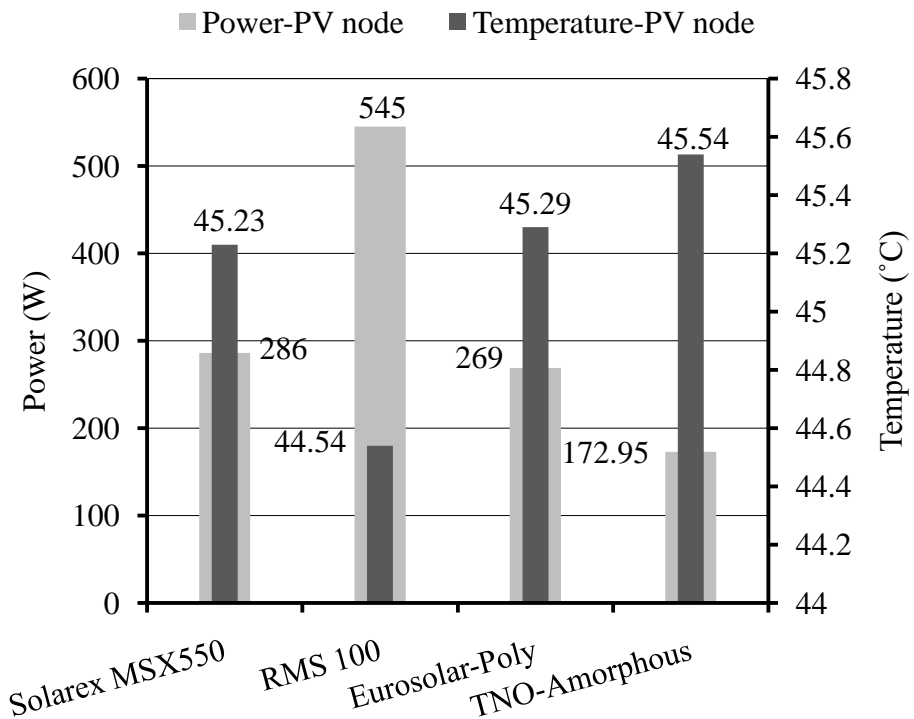
Figure 6-23: Power productions from different PV modules without PCM.

From figure 6-22 and figure 6-23 it can be seen that PCM integration reduces the PV cell temperature and improves power production. Besides the influence of the PCM, the reduction in PV temperature depends also on the electrical conversion efficiency, where high power production leads to lower PV temperature.

Cooling under warm climate condition: Consider the boundary conditions shown in figure 6-24; the maximum and minimum ambient temperature varies between 42°C and 25°C, while the maximum direct and diffuse solar irradiance are 950 W/m^2 and 300 W/m^2 respectively.
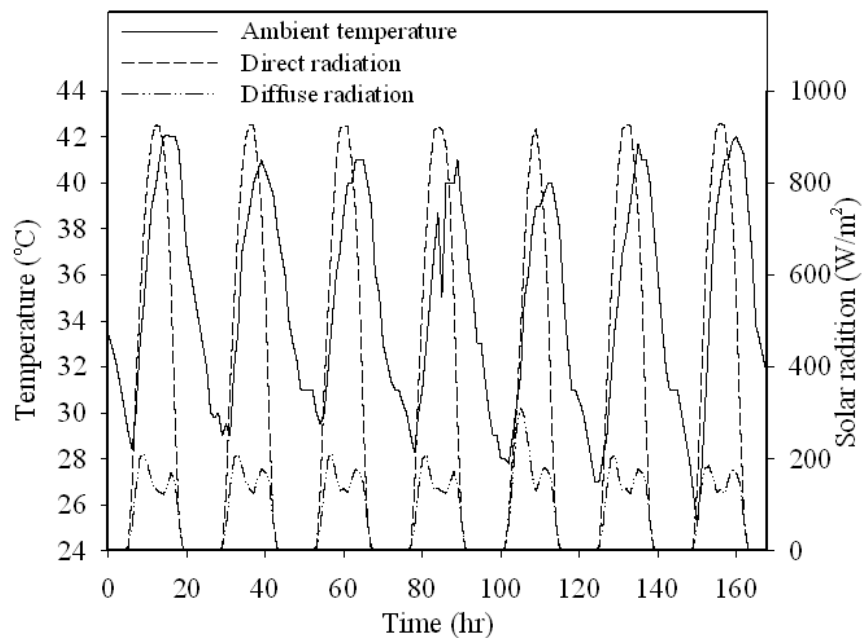
Figure 6-24: Temperature and direct/diffuse solar radiation boundary condition for the period 1-7 July as an example of a warm climate.

The model with the double façade office zones is used with a heavy construction as summarised in table E-2 in appendix (E). The cooling process follows the same strategy used in the cold region case. The zones start to overheat and are cooled according to the strategy shown in figure 6-14 using the control plan

as summarised in table 6-1 but with a maximum cooling equal to 10 kW. Figure 6-25 illustrates the different temperature responses for the PV/PCM internal surfaces using different phase change temperature ranges of 25˚C-30˚C, 30˚C-35˚C and 35˚C-40˚C.
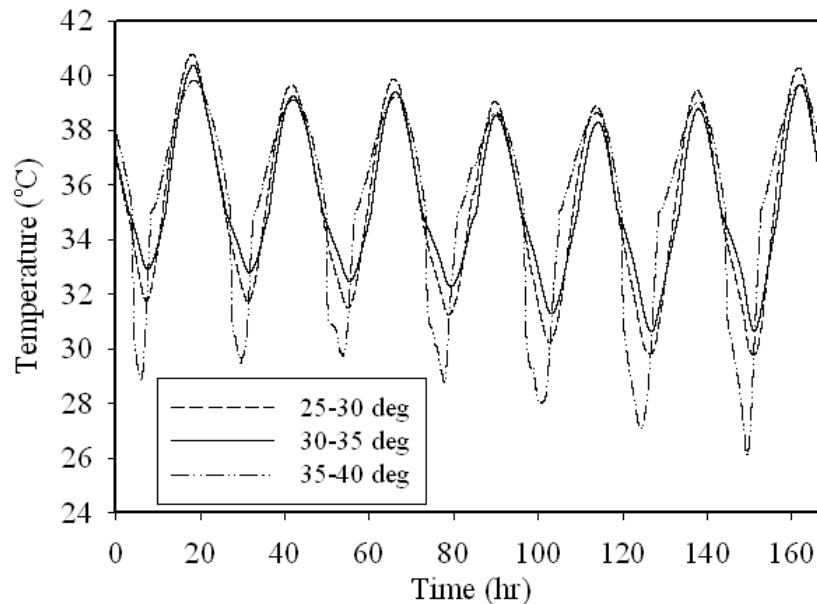
Figure 6-25: Internal surfaces temperature variation for the second level double façade using PCM with different phase change ranges and natural ventilation.

From figure 6.24, high temperature differences during the day can be observed; these can reach more than 40˚C during the day and around 25˚C during the night. Therefore, careful consideration is required to select the appropriate phase change temperature range. There is a wide range of PCM phase change temperatures, and for the purpose of selecting an appropriate one the performance of several candidates was investigated. First, the melting temperature is selected as equal to the minimum ambient temperature of 25˚C-30˚C. Figure 6.25 shows that the PCM layer remains in a liquid phase at all times without discharging; thus, this range is not feasible. In the second case, the range of 30˚C-35˚C was used because of the high

daily temperature differences; a large part of the PCM layer remained in a liquid phase in the discharging period. This reduces the efficiency of the heat storage capacity of the PCM layer. In the third case, the selection of the upper phase change was limited to around the 40°C, i.e. towards the upper end of the ambient temperature range. The PCM layer began melting at a temperature of 35°C and continued to generate phase change up to 40°C. At this time the sun set and discharging took place. This phase change range gives the full duration for complete charging and discharging. During the discharging process, the existence of the relatively high temperature of the PCM heat exchanger inner surface keeps the heat transfer convection coefficient at a high rate. This improves the performance of the natural ventilation between the surface and the air flow, improving the draught within the building's ventilation system as shown in figure 6.26.
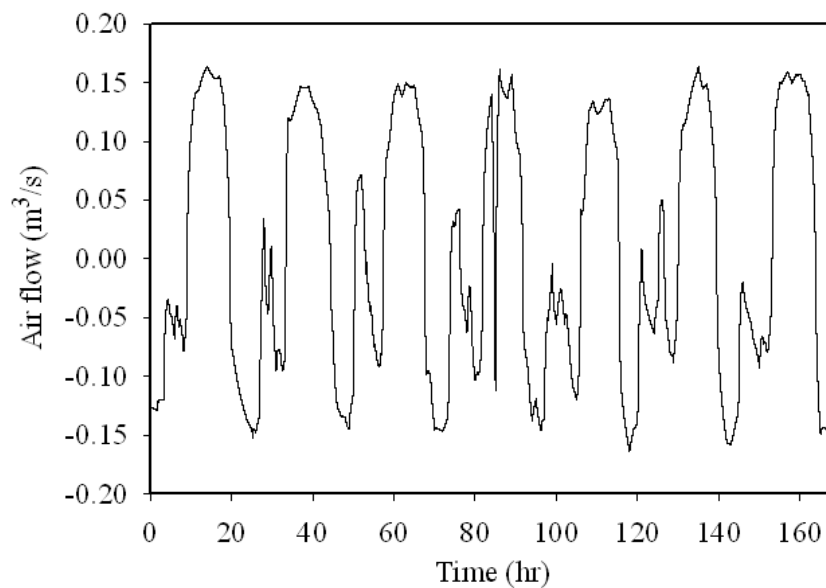
Figure 6-26: Air flow exhausted from the second façade to external with natural draught.

From table 6-5, the PV/PCM internal surfaces temperature in contact with the air gap is around 40°C less than the surface without PCM, the ventilated air from the zones will reduce the façade air gap compared to the case without PCM.

Table 6-5: PV/PCM performance under warm climate during 1-7 July and using different phase change temperature ranges.

Phase change range	PCM node			PV node		Inside surface
	$> T_m$	$> T_s$	Max.°C	$> T_s$	Max.°C	Max.°C
23-25°C	100%	100%	40.22	100%	40.36	40.29
25°C -30°C	100%	100%	40.24	100%	40.4	40.18
30°C-35°C	100%	76.5%	39.77	78%	40.1	39.86
35°C-40°C	82.5%	0%	39.27	0%	39.82	39.37
No. PCM	-	-	-	-	45.24	44.8
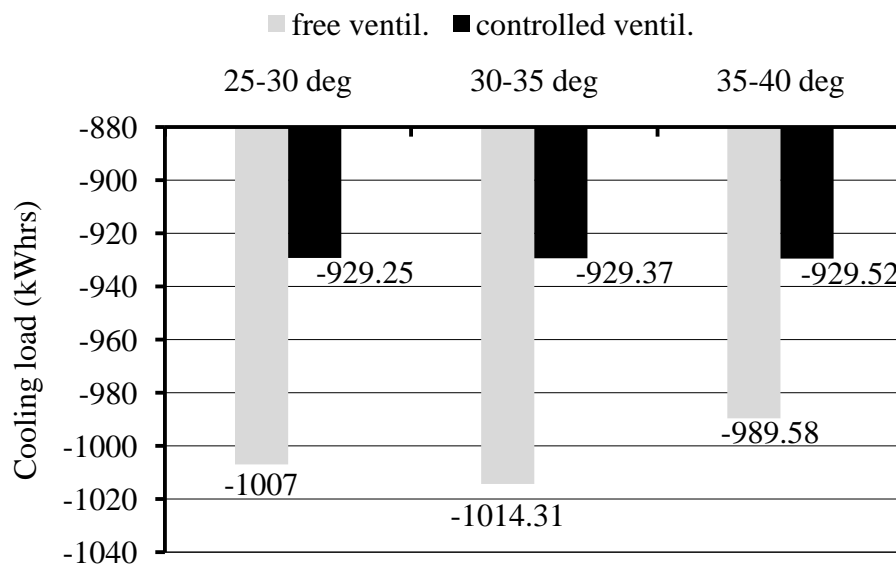
Figure 6-27: Cooling load for different phase change temperature ranges for PCM integrated into a double façade with natural ventilation.

The comparison between the results of natural ventilation for the different PCM phase change temperatures ranges is shown in figure 6.27. In the case of a phase change range of 35˚C-40˚C, the phase change extended most of the day especially when the ambient temperature reaches higher values. It also achieved full discharge during the night, resulting in good preparation for the next day. From figure 6-27, where the natural ventilation is controllable, a reduction in cooling load equal to 8.38% is achieved. The ventilated air drawn from inside the building into the double façade at a temperature less than the outside air will reduce the rise in the PCM temperature, especially during the middle of the day. However, the efficiency of the heat discharge remains low. To maximise the advantage from the heat stored, it is possible to integrate a network of water tubes according to the specification set out in table 6-6. This arrangement can result in an increase in the water outlet temperature from 9.7˚C to 11.47˚C higher than the temperature at the inlet condition.

Table 6-6: PV/PCM/with PCM phase change temperature range of 25˚C-30˚C and fitted with water tubes; simulated 1-7 July.

Water tube specification	PCM Max. Temp.˚C	Water outlet temperature.		PV Max. Temp.˚C
		Max.˚C	Min.˚C	
Water flow rate $(m^3/s)=2*10^{-6}$ Tube diameter =1cm Number of tubes=100 Tube length=5m Water inlet temperature =25˚C	39.66	36.47	34.7	39.96

6.3.3 Heating phase

Condition of cold climate: In heating applications, the ventilation system uses the double façade to pre-heat air. The cold air entering the ventilated cavity can be heated due to contact with the bounding surfaces and due to solar radiation. The temperature of an internal zone is sensed and actions taken through injection of sensible heat directly from an air handling unit, and actuation of the air flow rate supplied from the double façade if at a desirable temperature. The inlet temperature in the cavity influences both the transmission losses and the enthalpy change of the air flowing through the cavity. For the boundary conditions shown in figure 6-28, the average ambient air temperature entering the façade cavity reaches 10˚C.
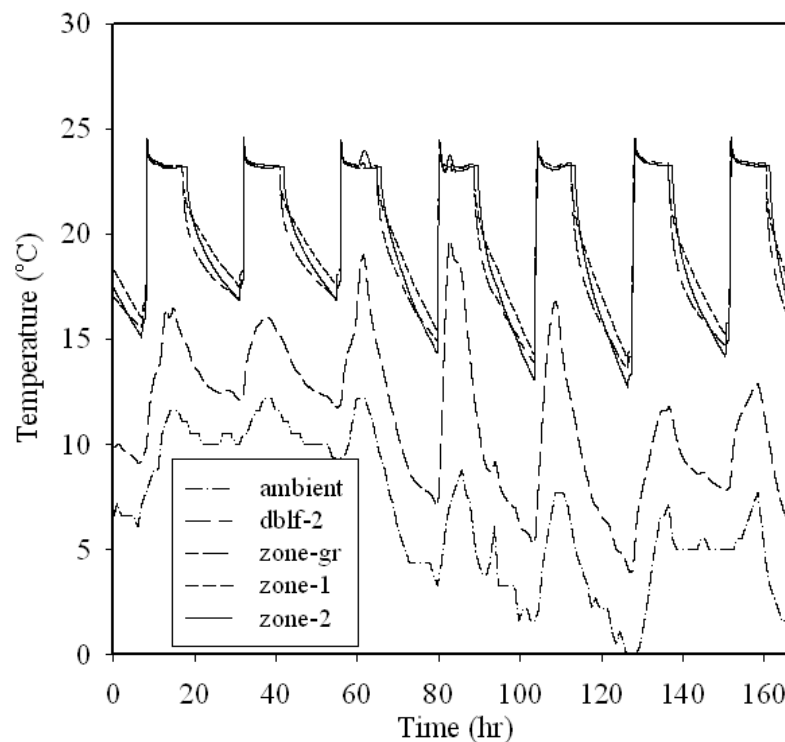
Figure 6-28: Internal zone temperature variation under heating control (h_c=2 W/m^2˚C).
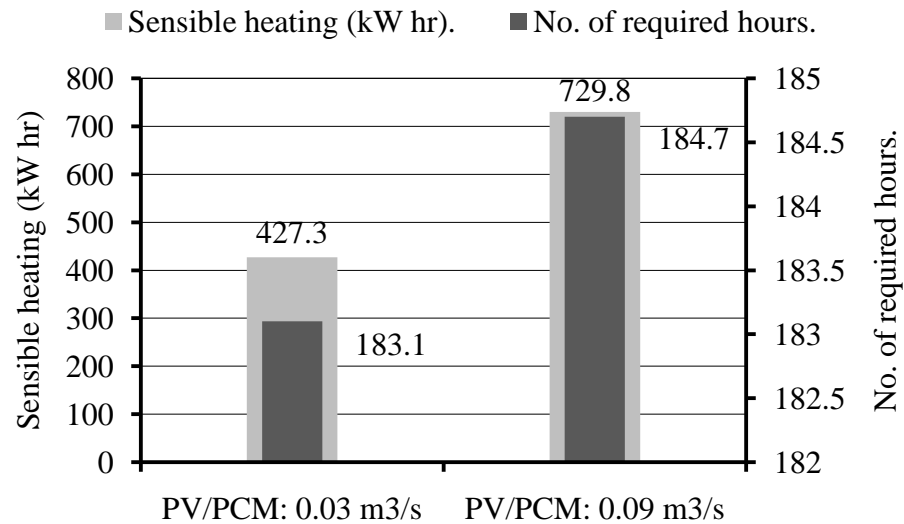
Figure 6-29: Heating load and number of hours required for different fan flow rates for double façade with PCM; (h_c=2 W/m$^{2\circ}$C).

The maximum air temperature in the second level double façade is in general below the heating set point temperature 23°C; the heat is therefore added sensibly. The reason for the heating energy reduction is depicted in figure 6-29; a lowering of the ventilation rate to allow slow air heating and improved pre-heating.

Condition of warm climate: Figure 6-30 corresponds to another boundary condition for the period 1-7 January in a warm climate where the ambient temperature, direct and diffuse solar radiation are illustrated. The ambient temperature varies between 23-4.6°C. From table 6-7, the 25°C-30°C showed the longest phase change period in charging and discharging. With the 35°C-40°C range, the PCM layer charged and discharged sensibly with no phase change and the material remained in the solid phase. For the intermediate case between the two temperature ranges above, the PCM layer was above its melting temperature for 18.6% of the time and the low ambient temperature limited the opportunity to change phase.
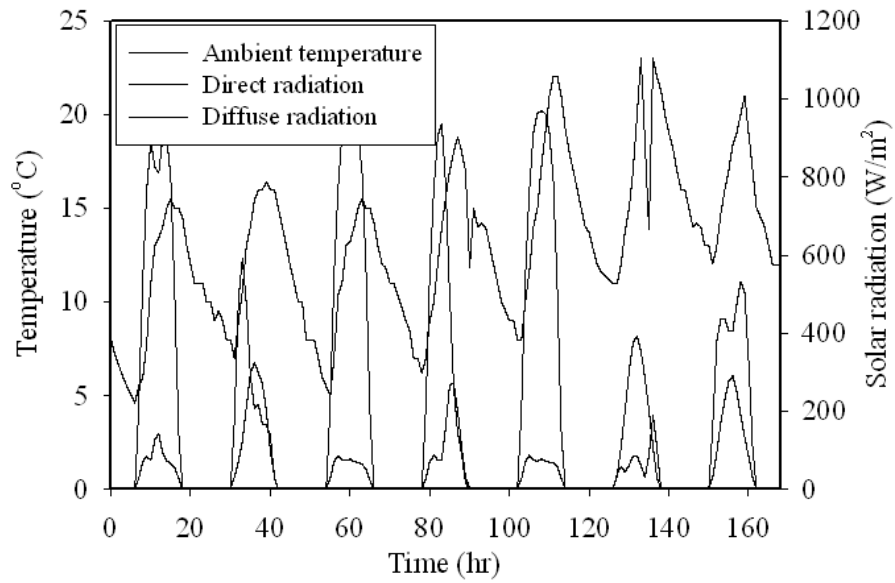
Figure 6-30: Temperature and direct/diffuse solar radiation boundary condition for the period 1-7 January.

Table 6-7: PV/PCM performance under warm climate over the period 1-7 January and using different phase change temperature ranges.

Phase change range	PCM node			PV node		Inside surface	dblf-2 zone
	$> T_m$	$> T_s$	Max. ˚C	$> T_s$	Max. ˚C	>23˚C	>23˚C
23˚C -25˚C	63.5%	44%	36.72	43.5%	38.17	59.7%	9.2%
25˚C -30˚C	60.4%	21.2%	37.17	25.1%	39.57	37.3%	9.6%
30˚C-35˚C	46.8%	9.1%	38.67	17.4%	41.12	50.4%	12.7%
35˚C-40˚C	34.7%	1.4%	40.68	11.6%	43.43	43.8%	18.2%
No PCM	-	-	-	-	57.26	36.5%	20.5%

Chapter 7 : Conclusions and Future Work

7.1 Conclusions

The use of PCM is a means to control PV temperature by exploiting the PCM's capacity to accumulate heat at temperatures close to the phase change range. By also exploiting (in smaller part) their specific heat, these materials act as heat accumulators, absorbing and discharging heat, keeping their temperature unchanged and thus avoiding the overheating of the PV panel. Effective PCMs in this application are suitably robust materials that undergo a phase change at around ambient temperature. As far as climate conditions are concerned, the two main issues that could limit the effective use of this technology are

1- the night outdoor air temperature has to be sufficiently lower than the daytime value; and

2- the heat transfer coefficients between the air and the element encapsulating the PCM needs to be high.

The main problems encountered have to do with the determination of the characteristics of the PCM layer and the evaluation of the PV layer's principal characteristics (power production, optical properties). When attempting to eliminate the effect of a high PV temperature by using a PCM layer, the phase change temperature range represents the most important factor that must be selected to ensure repeated melting and solidification over the daily ambient temperature range. In addition, the phase change temperature range will determine the charging and discharging time. A high phase change temperature keeps the component in continuous sensible heating and keeps the PCM in the solid phase. A low phase change temperature value will keep the PCM in the liquid phase. The purpose of the PCM is to reduce the PV temperature, with a target temperature around the ambient

temperature. Selecting the phase change variation around the daily ambient temperature range gives rise to the following advantages.

i. Small parts of the PCM body start melting before the maximum ambient temperature is reached and this delays the sensible temperature increase of the PV as shown in figure 7-1a.

ii. The other parts of the PCM body pass through the phase change range and complete melting when the PCM temperature reaches its maximum phase change limit ($T_s \geq T_{amb}$). The total time for the charging process is extended through heat transfer with the ambient temperature. The optimum condition is when the charging time duration is extended until the ambient temperature reaches its maximum value and starts to decrease (i.e. around sunset) as shown in figure 7-1b.

iii. The ambient temperature starts decreasing and a full discharge is guaranteed as shown in figure 7-1c.

$(T_{pcm} < T_{PV} > T_{amb})$

$(T_{pcm} < T_{amb})$

(a) Charging process

$(T_{PV} > T_{amb})$

$(T_{PV} > T_{pcm} > T_{amb})$

(b) Charging discharging process

$$(T_{pcm} > T_{PV} \geq T_{amb})$$

$$(T_{PV} < T_{pcm} > T_{amb})$$

(c) Discharging process
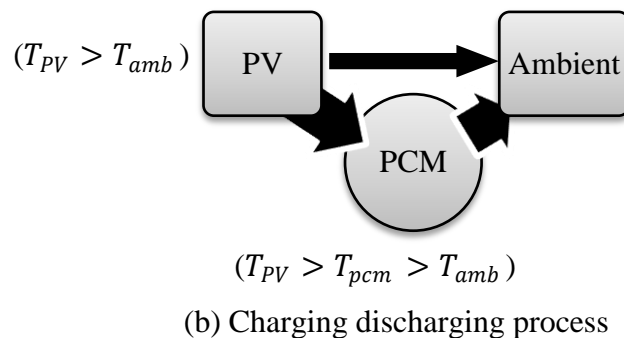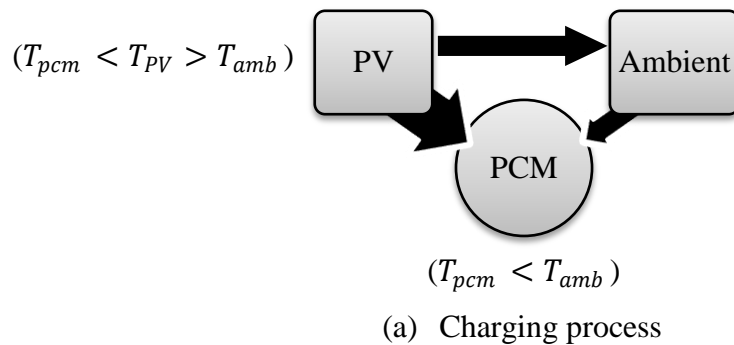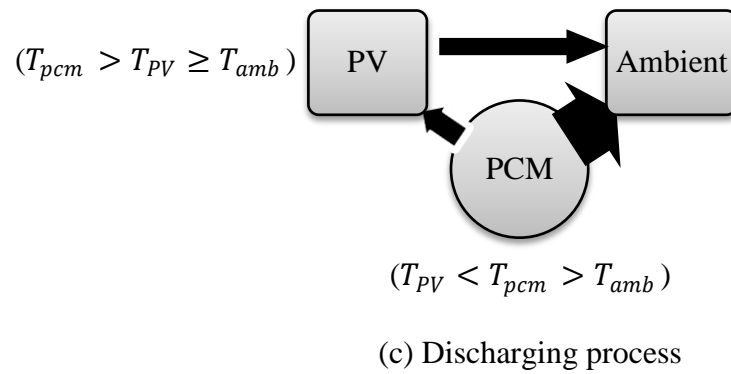
Figure 7-1: Phase change relation with both ambient and PV temperature.

To attain a PV target cooling temperature below the ambient temperature at all times of the day would require the use of a non-air fluid to cool the PCM heat exchanger.

7.1.1 Thermal performance of PCM in PV/PCM component

The experimental results show that the upper PV surface temperature is elevated when the PCM temperature rises within the phase change limits (figure 5-11). As the phase change process ends and all the material become liquid, the additional heat absorbed by the PV/PCM causes its temperature to increase sensibly. Poor cooling of the lower surface will accumulate the heat absorbed in the PCM layer. Because of the stratification behaviour of the phase change process, heat accumulates and the temperature of the lower surface reaches a maximum value of above 50˚C as shown in figure 5-14. The PCM contact interface starts to melt and the liquid volume fraction increases. The convection and density difference at the contact melting surface and PV inner surface increases the effective thermal conductivity of the PCM. From figure 5-13, it can be seen that as the liquid fraction increases, the heat energy accumulates and the temperature rises rapidly.

The enhancement in effective thermal conductivity when convection exists explains the low charging time in the melting process. Increased charging time is needed to delay the liquid fraction building in the PCM layer by a continuous cooling process (i.e. using an air gap as shown in figure 5-15). The low thermal conductivity of the PCM had a negative effect on the rate of heat transfer. In addition to the cost of PCM, the increase in the quantity of the PCM necessitates the need to significantly increase the time of charging or discharging. If it is very thick, part of the PCM will not melt or will become solid within the daily change of temperature; if the PCM is very thin and the PV temperature was any higher, the charging time would decrease. There needs to be a trade-off between charge parameters to ensure that all available heat is stored and subsequently discharged. Improving the discharging process by increasing the thermal conductivity of the PCM showed a small improvement compared with an increased convection heat transfer coefficient as shown in table 4-3. The PCM layer optimisation in section 4-10 showed that if a heat convection coefficient equal to 2 W/m^2°C is used, a PCM layer of 10 mm when cooled will give rise to a solid PCM front depth of about 2.67 mm on a daily cycle of 10 hours. Thus, 7.33 mm will be under charging and therefore not used at the next cycle. If the convection coefficient is increased to 7 W/m^2.K, the solid front moves at 0.93 mm/hr or 9.3 mm on a daily cycle of 10 hours. Here, all the heat stored in the PCM layer is rejected by convection and 93% of the total thickness is ready to use in the next cycle. For a convection coefficient value equal to 25 W/m^2.K, the full 10 mm discharging time is about 3 hr. If the possibility of attaining an appropriate convection heat transfer coefficient to the external environment is not available, PV/PCM integration with parts of the building, such as a double façade or building

ventilation systems, is the preferred method to adjust the charging and discharging process as shown in chapter 6.

In PCM modelling, the influence of the PCM depends on phase change tracking. Both the size of the PCM domain and the surface temperature strongly influence the temperature distribution and the mushy region location. For this reason, a parametric study was under taken to examine the effect of reducing the simulation time step and increasing PCM layer discretisation. The results show good accuracy when the PCM layer is divided into small virtual layers (9 virtual layers is the established best default) and the simulation time step is set to 1 min.

7.1.2 Integration PV/PCM in building ventilation systems

Building envelope elements provide several styles for PV integration. The climate and the PV cell characteristics determine the type and direction of the appropriate elements within the building envelope. For a transparent or semi-transparent building envelope element, a transparent and semi-transparent PV cell can be integrated with semi-transparent PCMs. With a PV/PCM component, it is possible to control the natural light and solar load in the building space. The results obtained from modelling the semi-transparent PV/PCM within a building double facade showed the expected response of this component, where a low PV temperature was achieved as shown in figure 6-6. Where direct integration is used between the building envelope and PV/PCM, in an insulated and non-ventilated PV/PCM façade, the PV surface temperature will be more than the PCM melting temperature for long periods when compared with PV/PCM with air-cooling as shown in figure 6-2. However, in direct integration, because the PCM layer takes

more time to complete the discharging process, the PV upper surface has a higher temperature for a prolonged period of time. However, if a ventilated double façade is used, the effect of air-cooling via a duct behind the PV façade improves the phase change cycling significantly by removing all or part of the heat absorbed by the PCM as shown in figure 6-4. For building cooling, the PCM internal surface in contact with an air gap is maintained at around 23°C for 47.9% of the total time; this represents a 16.9% increase compared with a situation where PCM is not included as shown in figures 6-17 and 6-18. Improving natural ventilation leads to switching off the fan system, and a minimum of energy consumption takes place as shown in figure 6-20. If compared with the same model with a natural ventilation strategy, there is a reduction in the cooling capacity of up to 10.67 kWhr; this reduction represents 6.5%. The total number of hours needed to run the cooling system increases to 10.98 hr. Besides the influence of the PCM on energy consumption, there is an increase in the PV productive capacity of up to 0.924%, which is nearly equal to 4.67 W with a decrease in PV temperature of up to 7.7°C (i.e. a total increase of up to 0.608 W/°C), as shown in figure 6-21. In addition to PCM behaviour during phase change, the reduction in PV temperature depends also on the electrical conversion efficiency, where high power production leads to lower PV temperature as shown in figures 6-22 and 6-23. It is feasible to achieve a reduction in energy consumption by charging the PCM storage at a hotter day temperature and discharging during colder days. A parametric study has been carried out by varying PCM melting temperatures to assess the performance of the PCM storage unit. It has been found that when the phase change range of the storage material is near the highest ambient temperature of the hottest summer month, the reduction in energy

requirement is maximised. Air flow rates should be adjusted according to phase change temperature range and the ambient temperature difference between day and night. This makes large portions of the PCM layer experience phase change and increases the heat storage available for day-time use. The heat storage reduces the energy requirement for cooling/heating the buildings. In general, the latent heat storage improves the natural ventilation, decreases the hours needed to cool the zones, and eliminates or reduces the exhaust fan energy. In building heating applications, the pre-heated air reduces the heating load significantly. In a warm climate, where high ambient temperatures are observed, part of the heat stored can be used to provide hot water for domestic used by embedding water tubes as a second heat sink as shown in table 6-6. Depending on the temperature at the water inlet, a marked increase in the outlet water temperature can be achieved. The hot water system is then supplied with water, which requires less energy to raise its temperature to the required value.

7.2 Recommendations

Results have shown that the PV/PCM:

   i. Enhances performance by combining multiple functions in the same building element. However, the climate conditions appreciably limit the applicability of such a hybrid component.

  ii. By chosen an appropriate phase change range and the method of integration of the PV/PCM component several advantages may be realized as follows.

             1. It will enable and enhance the possibilities of PCM completing the charging and discharging process.

2. Integration with building ventilation system will lead to improvement in operating performance.

iii. It will allow the integration of new architectural components into energy efficient building concepts. A number of PCM have the ability to change their optical properties within the phase change temperature range. Besides controlling PV temperature, this allows both thermal energy and natural light to be manipulated.

iv. In a warm climate, part of the heat stored can be used to provide hot water in both warm and cold seasons.

v. In building-integrated PV, the usefulness and timing of the thermal energy produced is crucial. The thermal energy can be stored in the PCM and used to preheat incoming air in cold seasons or support natural ventilation for buildings with high ventilation requirements.

7.3 Future Work

Careful attention to the climate context, type of building and mounting surface orientation is important to obtain acceptable PCM performance. Within the phase change process, the physical properties are usually varied within a simulation period. For better understanding of these processes within a PV/PCM, future work on the potential to develop and enhance phase change simulation through incorporating PV/PCM hand-shaking within building multi-dimensional variable thermo-physical properties is required. A computational fluid dynamic technique is suggested for solving the microscopic heat transfer phenomena within a PCM layer with convection dominating the liquid phase. The possibility of improving the performance of the phase change process through integration with both control

systems and air conditioning also needs to be further researched. Improving the performance of building façades by integrating semi-transparent PV/PCM components to additionally enable daylight capture should also be investigated.

References

Aasem E. O., 1993, 'Practical simulation of buildings and air-conditioning systems in the transient domain', *PhD Thesis*, University of Strathclyde, Glasgow, UK.

Abhat A., 1983, 'Low temperature latent heat thermal energy storage: heat storage materials', *J. Solar Energy*, Vol. 30, No. 4, pp. 313-332.

Adine H. A. and ElQarnia H., 2009, 'Numerical analysis of the thermal behaviour of a shell-and-tube heat storage unit using phase change materials', *J. Applied Mathematical Modelling*, Vol. 33, No. 4, pp. 2132-2144.

Agyenim F., Hewitt N., Eames P. and Smyth M. 2010, 'A review of materials, heat transfer and phase change problem formulation for latent heat thermal energy storage systems', *J. Renewable and Sustainable Energy Reviews*, Vol. 14, No. 2, pp. 615-628.

Akhilesh R., Narasimhan A. and Balaji C., 2005, 'Method to improve geometry for heat transfer enhancement in PCM composite heat sinks', *J. Heat and Mass Transfer*, Vol. 48, No. 13, pp. 2759 - 2770.

Al-Ajmi F., Loveday D. L. and Han by V. I., 2006, 'The cooling potential of earth-air heat exchangers for domestic buildings in a desert climate', *J. Building and Environment*, Vol. 41, No. 3, pp. 235 - 244.

Al-Awadhi E. M., 2008, 'Thermal analysis of a building brick containing phase change material', *J. Energy and Buildings*, Vol. 40, No. 3, pp. 351-357.

Alexiades V. and Solomon A. D., 1993, *Mathematical modelling of melting and freezing processes*, Hemisphere Publishing Corporation Taylor & Francis, Washington DC, USA.

Beausoleil-Morrison I., 2000, 'The adaptive coupling of heat and air flow modelling within dynamic whole-building simulation', *PhD Thesis*, University of Strathclyde, Glasgow, UK.

Benemann J., Chehab O. and Schaar-Gabril E., 2001, 'Building-integrated PV modules', *J. Solar Energy Materials and Solar Cells*, Vol. 67, No. 1, pp. 345 – 354.

Benlia H. and Durmus A., 2009, 'Performance analysis of a latent heat storage system with phase change material for new designed solar collectors in greenhouse heating', *J. Solar Energy*, Vol. 83, No. 12, pp. 2109-2119.

Bony J. and Citherlet S., 2007, 'Numerical model and experimental validation of heat storage with phase change materials', *J. Energy and Buildings*, Vol. 39, No. 10, pp. 1065–1072.

Breteque E. A. D. L., 2009, 'Thermal aspects of c-Si photovoltaic module energy rating', *J. Solar Energy*, Vol. 83, No. 9, pp. 1425-1433.

Brinkworth B. J., Crossa B. M. C., Marshalla R. H. and Yang H., 1997, 'Thermal regulation of photovoltaic cladding', *J. Solar Energy*, Vol. 61, No. 3, pp. 169-178.

Chua S. C., OH T. H. and Goh W. W., 2011, 'Feed-in tariff outlook in Malaysia', *J. Renewable and Sustainable Energy Reviews*, Vol. 15, No. 1, pp. 705 – 712.

CIBSE 2006, *Renewable energy sources for buildings,* ISBN: 1 903287 73 1.

Clarke J. A., 2001, *Energy simulation in building design (2nd edition)*, Butterworth-Heinemann, Oxford, UK.

Danchev S., Maniatis G. and Tsakanikas A., 2010, 'Returns on investment in electricity producing photovoltaic systems under de-escalating feed-in tariffs: the case of Greece', *J. Renewable and Sustainable Energy Reviews*, Vol. 14, No. 1, pp. 500 – 505.

Delgado A. E. and Da-Wen S., 2001, 'Heat and mass transfer models for predicting freezing processes – a review', *J. Food Engineering*, Vol. 47, No. 3, pp. 157 – 174.

Dincer I. and Rosen M., 2002, *Thermal energy storage systems and applications*, John Wiley & Sons Ltd, England, UK.

Eicker U., 2003, *Solar technologies for buildings*, John Wiley & Sons Ltd, England, UK.

ESRU, 1997, *The ESP-r system for building energy simulation: user guide version 9 series*, ESRU, University of Strathclyde, Glasgow, UK.

ESRU, 2002, *The ESP-r system for building energy simulation: user guide version 10 series*, ESRU, University of Strathclyde, Glasgow, UK.

Fan L. and Khodadadi J. M., 2011, 'Thermal conductivity enhancement of phase change materials for thermal energy storage: A review', *J. Renewable and Sustainable Energy Reviews*, Vol. 15, No. 1, pp. 24 – 46.

Farajia M., El-Qarniaa H. and Ramos J. C., 2009, 'Thermal control of protruding electronic components with PCM: A parametric study', *J. Numerical Heat Transfer*, Vol. 56, No. 7, pp. 579 – 603.

Farid M. M. and Chen X. D., 1999, 'Domestic electrical space heating with heat storage', *J. Power and Energy*, Vol. 213, No. 2, pp. 83-92.

Farid M. M., Khudhair A. M., Razack S. A. K. and Al-Hallaj S., 2004, 'A review on phase change energy storage: materials and applications', *J. Energy Conversion and Management*, Vol. 45, No. 9-10, pp. 1597 – 1615.

Fath H. E. S., 1995, 'Thermal performance of a simple design solar air heater with built-in thermal energy storage system', *J. Energy Conversion and Management*, Vol. 36, No. 10, pp. 989 – 997.

Farrell A. J., Norton B., Kennedy D. M., 2006, 'Corrosive effects of salt hydrate phase change materials used with aluminium and copper', *J. Materials Processing Technology*, Vol. 175, No. 1-3, pp. 198–205.

Garg H. P., Mullick S. C. and Bhargava A. K., 1985, *Solar thermal energy storage,* Springer, Holland.

Gunther E., Harald M. and Stefan H., 2007, 'Modelling of subcooling and solidification of phase change materials', *J. Modelling and Simulation in Materials Science and Engineering*, Vol. 15, No. 8, pp. 879 -892.

Habbib I. S., 1971, 'Solidification of semi-transparent materials by conduction and radiation', *J. Heat and Mass Transfer*, Vol. 14, No. 12, pp. 2161 – 2164.

Halford C. K. and Boehm R. F., 2007, 'Modelling of phase change material peak load shifting', *J. Energy and Buildings*, Vol. 39, No. 3, pp. 298 – 305.

Hand J. and Strachan P., 1998, 'ESP-r data model decomposition', *Occasional paper*, ESRU, University of Strathclyde, Glasgow, UK.

Hansen J. L. M., 1991, 'On the thermal interaction of building structure and heating and ventilation system', *PhD Thesis*, University of Eindhoven, Glasgow, UK.

Hasan A., McCormack S. J., Huang M. J., Norton B., 2010, 'Evaluation of phase change materials for thermal regulation enhancement of building integrated photovoltaics', *J. Solar Energy*, Vol. 84, No. 9, pp. 1601-1612.

Hawes D. W., Banu D. and Feldman D., 1990, 'Latent heat storage in concrete II', *J. Solar Energy Materials*, Vol. 21, No. 1, pp. 61 – 80.

Hawes D. W., Feldman D. and Banu D., 1993, 'Latent heat storage in building materials', *J. Energy and Buildings*, Vol. 20, No. 1, pp. 77 – 86.

He B., Martin V. and Setterwall F., 2003, 'Liquid-solid phase equilibrium study of tetradecane and hexadecane binary mixtures as phase change materials PCMs for comfort cooling storage', *J. Fluid Phase Equilibrium*, Vol. 212, No. 1-2, pp. 97 – 109.

Heim D., 2005, 'Two solution methods of heat transfer with phase change within whole building dynamic simulation', *Building Simulation*, *Proc. 10th Int. IBPSA Conference*, Montréal, Canada.

Heim D. and Clarke J. A., 2004, 'Numerical modelling and thermal simulation of PCM-gypsum composites with ESP-r', *J. Energy and Buildings*, Vol. 36, No. 8, pp. 795 – 805.

Ho C. J. and Chu C. H., 1996, 'Thermal protection characteristics of a vertical rectangular cell filled with PCM/air layer', *J. Heat and Mass Transfer*, Vol. 31, No. 3, pp. 191 – 198.

Ho C. J. and Chang J. Y., 1994, 'A study of natural convection heat transfer in a vertical rectangular enclosure with two-dimensional discrete heating: Effect of aspect ratio', *J. Heat and Mass Transfer*, Vol. 37, No. 6, pp. 917 – 925.

Hoseon Y. and Ro S. Tack, 1991, 'Melting process with solid-liquid density change and natural convection in a rectangular cavity', *J. Heat and Fluid flow*, Vol. 12, No. 4, pp. 365 – 374.

Huang M. J., Eames P. C. and Hewitt N. J., 2006a, 'The application of a validated numerical model to predict the energy conservation potential of using phase change materials in the fabric of a building', *J. Solar Energy Materials and Solar Cells*, Vol. 90, No. 13, pp. 1951 – 1960.

Huang M. J., Eames P. C. and Norton B., 2004, 'Thermal regulation of building-integrated photovoltaics using phase change materials', *J. Heat and Mass Transfer*, Vol. 47, No. 12-13, pp. 2715 – 2733.

Huang M. J., Eames P. C. and Norton B., 2006b, 'Comparison of a small-scale 3D PCM thermal control model with a validated 2D PCM thermal control model', *J. Solar Energy Materials and Solar Cells*, Vol. 90, No. 13, pp. 1961 – 1972.

Huang M. J., Eames P. C. and Norton B., 2006c, 'Phase change materials for limiting temperature rise in building integrated photovoltaics', *J. Solar Energy*, Vol. 80, No. 9, pp. 1121 – 1130.

Huang M. J., McCormack S., Eames P.C. and Norton B., 2008, 'The effect of phase change material crystalline segregation on the building integrated photovoltaic system thermal performance', *World Renewable Energy Congress WREC X*, Glasgow, Scotland, UK.

Huang M., Eames P., Norton B. and Hewitt N., 2011, 'Natural convection in an internally finned phase change material heat sink for the thermal management of photovoltaics', *J. Solar Energy Materials and Solar Cells*, Vol. 95, No. 7, pp. 1598 – 1603

Hu H. and Argyropoulos S. A., 1996, 'Mathematical modelling of solidification and melting: a review', *J. Modelling Simulation Material Science. Engineering*, Vol. 4, No. 4, pp. 371–396.

Ibanez M., Ana L., Belen Z. and Luisa F. Cabeza, 2005, 'An approach to the simulation of PCMs in building applications using TRNSYS', *J. Applied Thermal Engineering*, Vol. 25, No. 11-12, pp. 1796 – 1807.

IEA, 2009, *CO₂ Emissions from fuel combustion highlights*, International Energy Agency.

Ismail K. A. R. and Hentoquez J. R., 2002, 'Parametric study on composite and PCM glass systems', *J. Energy Conversion and Management*, Vol. 43, No. 7, pp. 973 – 993.

Jager-Waldau A., 2010, 'PV status report 2010: research solar cell production and market implementation of photovoltaics', Report for European Commission Joint Research Centre, Institute for Energy, Luxembourg.

Jamnia A., 2000, *Practical guide to the packaging of electrics: thermal and mechanical design and analysis*, CRC Press.

Ji J., LU J. P., Chow T. T., He W. and Pei G., 2007, 'A sensitivity study of a hybrid photovoltaic/thermal water-heating system with natural circulation', *J. Applied Energy*, Vol. 84, No. 2, pp. 222 – 237.

Kandasamy R., Wang X. Q. and Mujumdar A. S., 2007, 'Application of phase change materials in thermal management of electronics', *J. Applied Thermal Engineering*, Vol. 27, No. 17-18, pp. 2822 – 2832.

Kelly N. J., 1998, 'To wards a design environment for building-integrated energy systems: the integration of electrical power flow modelling with building simulation', *PhD Thesis*, University of Strathclyde, Glasgow, UK.

Kenisarin M. M., 2010, 'High-temperature phase change materials for thermal energy storage', *J. Renewable and Sustainable Reviews*, Vol. 14, No. 3, pp. 955 – 970.

Kenisarin M. and Mahkamov K., 2007, 'Solar energy storage using phase change materials', *J. Renewable and Sustainable Energy Reviews*, Vol. 11, No. 9, pp. 1913 – 1965.

King D. L., Kratochvil J. A., Boyson W. E. and Bower W. I., 1998, 'Field experience with a new performance characterization procedure for photovoltaic arrays', *2nd world conference and exhibition on photovoltaic solar energy conversion 6-10 July*, Vienna, Austria.

King D. L., Kratochvil J. A. and Boyson W. E., 1997, 'Temperature coefficients for PV modules and arrays: measurement methods, difficulties and results', *Photovoltaic specialist's conference record of the twenty-sixth, IEEE.*

Krajacic G., Duic N., Tskalakis A., Zoulias M., Caralis G., Panteri E., Rigter J. and Vidican G., 2010, 'Cost and optimal feed-in tariff for small scale photovoltaic systems in China', *J. Energy Policy*, Vol. 38, No. 11, pp. 6989 – 7000.

Krauter S., Salhi M. J., Schroer S. and Hanitsch R., 2001, 'New facade system consisting of compound photovoltaic and solar thermal generators with building insulation', *Seventh International IBPSA Conference,* Brazil.

Kreith F., 2000, *Handbook of thermal engineering*, Springer-Verlage, Heidelberg, Germany.

Krishnan S., Garimella S. V. and King S. S., 2005, 'A novel hybrid heat sink using phase change materials transient thermal management of electronics', *IEEE transactions on components and packaging technologies*, Vol. 28, No. 2, pp. 281 – 289.

Kuznik F. and Virgone J., 2009, 'Experimental investigation of wallboard containing phase change material: Data for validation of numerical modelling', *J. Energy and Buildings*, Vol. 41, No. 5, pp. 561 – 570.

L'azaro A., Gunther E., Mehiling H., Stefan H., Jose M., Marian and Belen Z., 2006, 'Verification of a T-history installation to measure enthalpy versus temperature curves of phase change materials', *J. Measurement Science and Technology*, Vol. 17, No. 8, pp. 2168 – 2174.

Lamberg P., Lehtiniemi R. and Henell A. M., 2004, 'Numerical and experimental investigation of melting and freezing processes in phase change material storage', *J. Thermal Sciences*, Vol. 43, No. 3, pp. 277 – 287.

Laouadi A. and Lacroix M., 1999, 'Thermal performance of a latent heat energy storage ventilated panel for electric load managnent', *J. Heat and Mass Transfer*, Vol. 42, No. 2, pp. 275 – 286.

Liu H. and Awbi H. B., 2009, 'Performance of phase change material boards under natural convection', *J. Building and Environment*, Vol. 44, No. 9, pp. 1788 – 1793.

Macqueen J., 1997, 'The modelling and simulation of energy management control systems', *PhD Thesis*, University of Strathclyde, Glasgow, UK.

Maycock P. D., 2005, 'PV review: World Solar PV market continues explosive growth', *J. Refocus*, Vol. 6, No. 5, pp. 18 – 22.

Mehling H. and Cabeza L. F., 2008, *Heat and cold storage with PCM*, Springer Verlage, Heidelberg, Berline, Germany.

Nakhi A. E., 1995, 'Adaptive construction modelling within whole building dynamic simulation', *PhD Thesis*, University of Strathclyde, Glasgow, UK.

Neeper D. A., 2000, 'Thermal dynamics of wallboard with latent heat storage', *J. Solar Energy*, Vol. 68, No. 5, pp. 393 – 403.

Negrao C. O. R., 1995, 'Conflation of computational fluid dynamics and building thermal simulation', *PhD Thesis,* University of Strathclyde, Glasgow, UK.

Nishioka K., Hatayama T., Uraoka Y., Fuyuki T., Hagihara R. and Watanabe M., 2003, 'Field-test analysis of PV system output characteristics focusing on module temperature', *J. Solar Energy Materials and Solar Cells*, Vol. 75, No. 3-4, pp. 665 – 671.

Nitz P. and Hartwig H., 2005, 'Solar control with thermotropic layers', *J. Solar Energy*, Vol. 79, No. 6, pp. 573 – 582.

Nunzi J. M., 2002, 'Organic photovoltaic materials and devices', *J. of Physics*, Vol. 3, No. 4, pp. 523 – 542.

Ozisik M., 1993, *Heat conduction,* John Wiley & Sons Inc, New York, USA.

Ozisik M., 1994, *Finite difference methods in heat transfer,* CRC press. Inc, Florida, USA.

Pal D. and Joshi. Y. K., 2001, 'Melting in a side heated tall enclosure by a uniformly dissipating heat source', *J. Heat and Mass Transfer*, Vol. 44, No. 2, pp. 375 – 387.

Pasupathy A., Velraj R. and Seeniraj R. V., 2008, 'Phase change material-based building architecture for thermal management in residential and commercial establishments', *J. Renewable and Sustainable Energy Reviews*, Vol. 12, No. 1, pp. 39 – 64.

Patankar S. V., 1980, *Numerical heat transfer and fluid flow*, Taylor and Francis.

Peippo K., Kauranen P. and Lund P. D., 1991, 'A multicomponent PCM wall optimized for passive solar heating', *J. Energy and Buildings*, Vol. 17, No. 4, pp. 259 – 270.

Pitts A., 2008, 'Future proof construction-future building and systems design for energy and fuel flexibility', *J. Energy Policy*, Vol. 36, No. 12, pp. 4539 – 4543.

Porez-Lombard L., Ortiz J. and Pout C., 2008, 'A review on buildings energy consumption information', *J. Energy and Buildings*, Vol. 40, No. 3, pp. 394 – 398.

Roberts S. and Guariento N., 2009, *Building integrated photovoltaics: a hand book, Birkhäuser* Verlag AG.

Roth K., Westphalen D. and Brodrick J., 2007, 'PCM technology for building materials', *J. ASHRAE*, Vol. 49, No. 7, pp. 129–31.

Sanyal D., Rao P. R., Gupta O. P., 2004, 'Modelling of free boundary problems for phase change with diffuse interface', *J. Mathematical Problems in Engineering*, Vol. 2005, No. 3, pp. 309 – 324.

Sharma A., Tyagi V. V., Chen C. R. and Buddhi D., 2009, 'Review on thermal energy storage with phase change materials and applications', *J. Renewable and Sustainable Energy Reviews*, Vol. 13, No. 2, pp. 318 – 345.

Sharma A., Won L. D., Buddhi D. and Park J. U., 2005, 'Numerical heat transfer studies of the fatty acids for different heat exchanger materials on the performance of a latent heat storage system', *J. Renewable Energy*, Vol. 30, No. 14, pp. 2179 – 2187.

Simone R. and Matthias W., 2009, *Phase change materials: science and applications*, Springer.

Skoplaki E., Boudouvis A. G. and Palyvos J. A., 2008, 'A simple correlation for the operating temperature of photovoltaic modules of arbitrary mounting', *J. Solar Energy Materials and Solar Cells*, Vol. 92, No. 11, pp. 1393 – 1402.

Skoplaki E. and Palyvos J. A., 2009, 'On the temperature dependence of photovoltaic module electrical performance: A review of efficiency/power correlations', *J. Solar Energy*, Vol. 83, No. 5, pp. 614 – 624.

Solomon A. D., 1979a, 'Melt time and heat flux for a simple PCM body', *J. Solar Energy*, Vol. 22, No. 3, pp. 251 – 257.

Solomon A. D., 1979b, 'A relation between surface temperature and time for a phase change process with a convective boundary condition', *J. Heat and Mass Transfer*, Vol. 6, No. 3, pp. 189 – 197.

Strachan P. A., 1998, 'Calibration with PST semi-transparent PV modules', *Occasional Paper*, ESRU, University of Strathclyde, Glasgow, UK.

Takashi I., 2003, 'Solar shading and daylighting by means of autonomous responsive dimming glass: practical application', *J. Energy and Buildings*, Vol. 35, No. 5, pp. 463 – 471.

Takashi I., Masayuki I. and Naoyoshi I., 2008, 'Thermotropic glass with active dimming control for solar shading and daylighting', *J. Energy and Buildings*, Vol. 40, No. 3, pp. 385 – 393.

Tan F. L. and Tso C. P., 2004, 'Cooling of mobile electronic devices using phase change materials', *J. Applied Thermal Engineering*, Vol. 24, No. 2-3, pp. 159 – 169.

Tan F. L. and Leong K. C., 1994, 'Effect of wall temperature and aspect ratio on the solid-liquid interface during freezing inside a rectangular enclosure', *J. Heat and Mass Transfer*, Vol. 21, No. 5, pp. 641–650.

Thomas R., Max F. and Partners, 2001, *Photovoltaics and architecture*, Spoon Press, London, UK.

UNEP, 2007, *Building and climate change, status, challenges and opportunities*, United Nation Environment Programme.

Watanabe H., 1998, 'Intelligent window using a hydrogel layer for energy efficiency', *J. Solar Energy Materials and Solar Cell*, Vol. 54, No. 1-4, pp. 203 – 211.

Weinlader H., Beck A. and Fricke J.,2005, 'PCM-facade-panel for daylighting and room heating', *J. Solar Energy*, Vol. 78, No. 2, pp. 177 – 186.

Yang H., Burnett J. and Zhu Z., 2001, 'Building-integrated photovoltaics: effect on the cooling load component of building façades', *J. Building Servicing RES Technology*, Vol. 22, No. 3, pp. 157 – 165.

Zahedi A., 2010, 'A review on feed-in tariff in Australia, what it is now and what it should be', *J. Renewable and Sustainable Energy Reviews*, Vol. 14, No. 9, pp. 3252 – 3255.

Zalba B., Jose M. M. and Cabeza L. F., 2003, 'Review on thermal energy storage with phase change materials heat transfer analysis and applications', *J. Applied Thermal Engineering*, Vol. 23, No. 3, pp. 251 – 283.

Zhang Y., Lin K., Jiang Y. and Zhou G., 2008, 'Thermal storage and nonlinear heat-transfer characteristics of PCM wallboard', *J. Energy and Buildings*, Vol. 40, No. 9, pp. 1771– 1779.

Zhu N., Ma Z. and Wang S., 2009, 'Dynamic characteristics and energy performance of buildings using phase change materials: A review', *J. Energy Conversion and Management*, Vol. 50, No. 12, pp. 3169 – 3181.

Appendix A

Figure A-1: Iterative solution of nested domain equations in ESP-r (Clarke 2001).
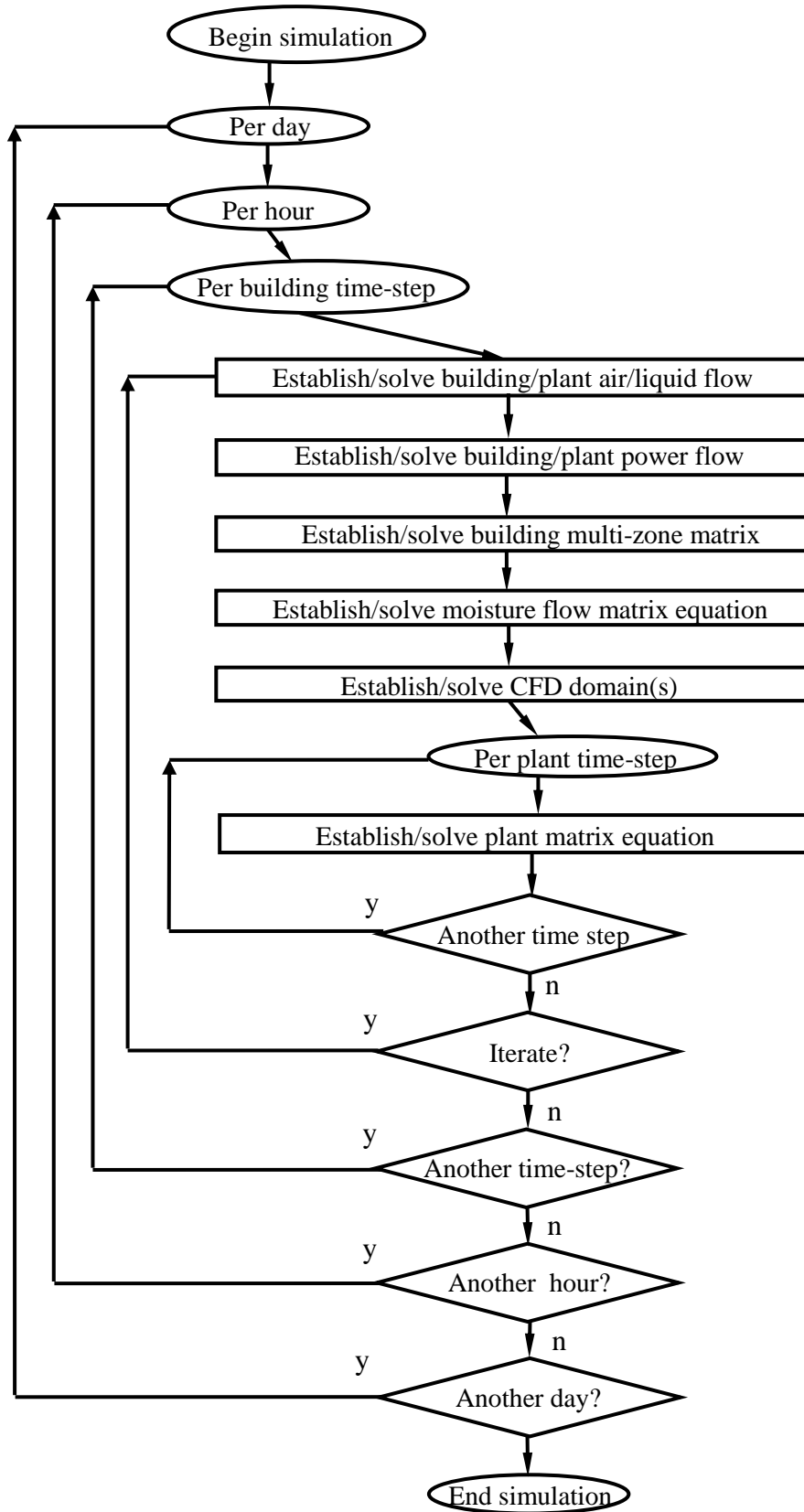
Appendix B

Table B-1: PlusICE organic solutions http://www.pcmproducts.net/.

PCM Type	Phase Change Temperature (˚C)	Density (kg/m³)	Heat Capacity (kJ/kg)
A164	164	1500	306
A144	144	880	230
A133	133	880	222
A95	95	900	202
A82	82	850	170
A70	70	890	220
A62	62	910	202
A60	60	910	197
A58	58	910	210
A55	55	905	195
A53	53	910	210
A42	42	905	195
A39	39	900	190
A32	32	845	215
A28	28	789	230
A26	26	790	225
A25	25	785	172
A24	24	790	225
A23	23	785	170
A22	22	785	172
A17	17	785	172
A15	15	790	173
A9	9	775	220
A8	8	773	220
A6	6	770	222
A4	4	766	227
A3	3	765	225
A2	2	76	225
E0	0	1000	332

Appendix C

Table C-1: Thermophysical properties for building materials used in figure 2-2 (Clarke 2001).

Material	Conductivity (Wm^{-1}°C^{-1})	Density (kg m^{-3})	Specific heat (J kg^{-1}°C^{-1})
Brick			
Aerated	0.30	1000.	840.
Breeze block	0.44	1500.	650.
Burned	0.75	1300.	840.
Inner leaf	0.62	1800.	840.
Outer leaf	0.96	2000.	650.
Paviour	0.96	2000.	840.
Reinforced	1.10	1920.	840.
Concrete			
Heavyweight	1.30	2000.	840.
Lightweight	0.20	620.	840.
Medium lightweight	0.32	1050.	840.
Very lightweight	0.14	370.	840.
No fines	0.96	1800.	840.
Aerated, Cellular	0.70	1000.	840.
aerated roofing slab	0.16	500.	840.
block, lightweight	0.64	1660.	840.
block, medium weight	0.86	1970.	840.
block, heavy weight	1.31	2240.	840.
block, aerated	0.24	750.	1000.
block, hollow, light weight	0.58	720.	840.
Mineral Wool			
Regular	0.038	140.	840.
Fibrous	0.043	96.	840.
resin bonded	0.036	99.	1000.
rock wool	0.033	100.	710.
Polystyrene			
Extruded	0.035	25.	1470.
Expanded	0.035	23.	1470.
expanded PVC	0.04	100.	750.

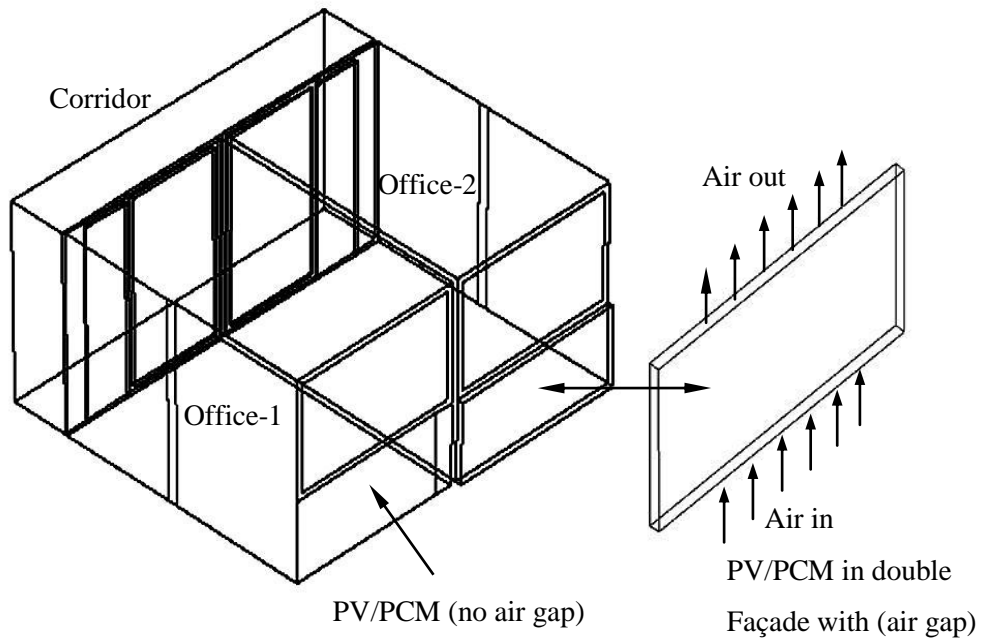| Material	Conductivity (Wm^{-1}°C^{-1})	Density (kg m^{-3})	Specific heat (J kg^{-1}°C^{-1})
Wood			
Fir, pine	0.12	510.	1380.
Maple, oak	0.16	720.	1260.
Cork			
Board	0.04	160.	1890.
Expanded	0.044	150.	1760.
expanded and impregnated	0.043	150.	1760.
Tiles	0.08	530.	1800.
Stone			
Basalt	3.5	3000.	840.
Sandstone	1.3	2150.	840.

Appendix D

Figure D-1: Model of PV/PCM with and without back surface cooling.

Table D-1: Construction of PV/PCM as used in the model shown in figure D-1.

| Office_1: Direct integration (No air gap).				
Material	Thickness (mm)	Conductivity (W/m˚C)	Density (kg/m^3)	Specific heat (J/kg.K)
Low-e glass	4	1.05	2500	750
PV-EVA	2	0.38	920	2100
PCM	10	0.5	750	1000
Steel	2	50	7800	502
Cork-insulation	300	0.04	105	1800
Office_2: Integration within double façade (Natural cooling via a 100 mm air gap). The PV/PCM structure included the same components above but without cork layer.				

Appendix E
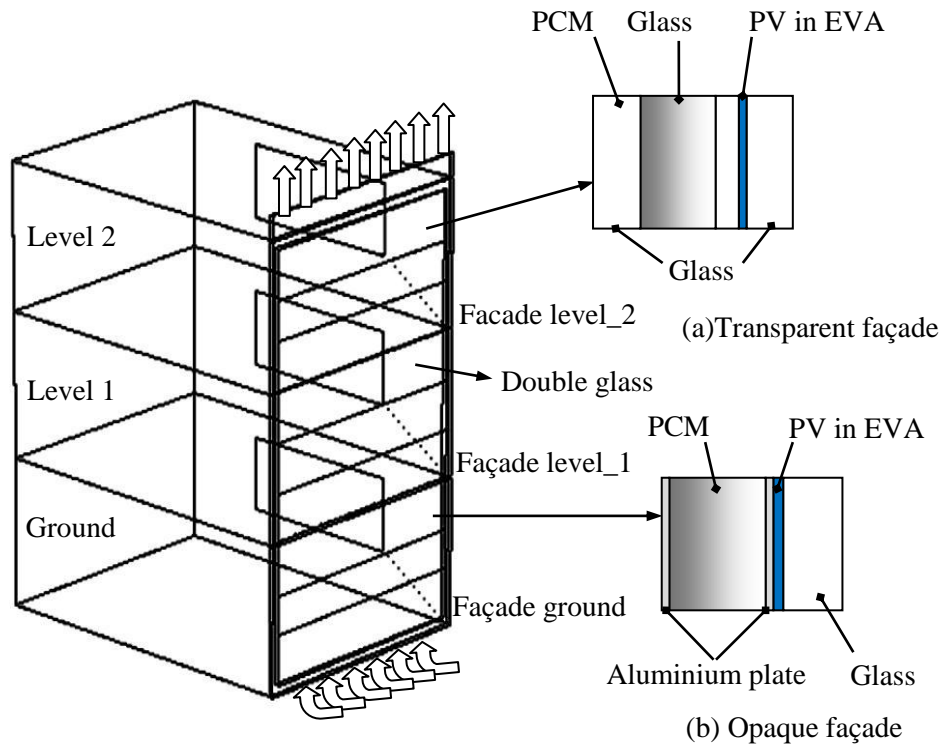
Figure E-1: A schematic diagram for model with 10 cm double façade integrated PV/PCM: a) semi-transparent; b) opaque.

Table E-1: Model construction thermal properties for light structure.

Walls		Roof		Façade
Rendering	20 mm	Grey coated alum. 1 mm		Single glass 4 mm
Concert block	100 mm	Air-gap	50 mm	Air-gap 10 cm
Air-gap	50 mm	EPS	106 mm	Double glass 4 mm
Plywood	10 mm	Gypsum-board	15 mm	
Glass wall	140 mm			
Gypsum-p-board	13 mm			
Ceiling Floor		PV/PCM construction		
Floor-el	5 mm	Low –e- glass	4 mm	
H-mix concrete	13 mm	PV-EVA	2 mm	
Air-gap	100 mm	Aluminium plate	1 mm	
Ceiling	13 mm	PCM	10 mm	
		Aluminium plate	2 mm	
PCM		*Conductivity*		*Density*
Phase Change: 25°C-30°C		0.2 W/m.K Solid		950 kg/m^3 Solid
		0.15 W/m.K Liquid		850 kg/m^3 Liquid

Table E-2: Model construction thermal properties for heavy structure.

Walls		Roof		Façade
Cement screed	30 mm	Floor tiles	12 mm	Single glass 4 mm
Breez block	250 mm	Cement screed	30 mm	Air-gap 10 cm
Cement screed	30 mm	Heavy mix concert 150 mm		Double glass 4 mm
		Cement screed	30 mm	Steel plate 2 mm
Partitions Floor		PV/PCM construction		
Glass	6 mm	Low-e-glass	4 mm	
Air gap	12 mm	PV-EVA	3 mm	
Glass	6 mm	Aluminium plate	1 mm	
		PCM	10 mm	
		Steel plate	1 mm	
PCM		*Conductivity*		*Density*
Phase Change: using different range of phase change.		0.2 W/m.K Solid		950 kg/m^3 Solid
		0.15 W/m.K Liquid		850 kg/m^3 Liquid